SYSTEMATICS OF CROSS SECTIONS FOR TARGET K-VACANCY PRODUCTION IN HEAVY ION COLLISIONS

A Dissertation

by

YONG PENG

Submitted to the Office of Graduate Studies of
Texas A&M University
in partial fulfillment of the requirements for the degree of

DOCTOR OF PHILOSOPHY

December 2006

Major Subject: Chemistry

SYSTEMATICS OF CROSS SECTIONS FOR TARGET K-VACANCY PRODUCTION IN HEAVY ION COLLISIONS

A Dissertation

by

YONG PENG

Submitted to the Office of Graduate Studies of
Texas A&M University
in partial fulfillment of the requirements for the degree of

DOCTOR OF PHILOSOPHY

Approved by:

Chair of Committee,	Rand L. Watson
Committee Member,	Sherry J. Yennello
	Joseph B. Natowitz
	John C. Hardy
Head of Department,	David Russell

December 2006

Major Subject: Chemistry

ABSTRACT

Systematics of Cross Sections for Target

K-vacancy Production in Heavy Ion Collisions. (December 2006)

Yong Peng, B.S., Sichuan University; M.S., Texas A&M University

Chair of Advisory Committee: Dr. Rand L. Watson

Cross sections for K-shell ionization by heavy ions have been determined from the measurements of target K x-ray yields. The measurements were performed with Ar, Kr, and Xe ions at energies from 2.5 to 25 MeV/amu and self-supported metallic foil targets of Al, Ti, Cu, Zr, Ag, Sm, and Ta. The x-ray yields were measured with a Si(Li) detector, while the projectile ions were counted in coincidence with the x-rays using a plastic scintillation detector. In addition, the amount of secondary K-shell ionization and the degree of simultaneous L-shell ionization in primary K-shell ionizing collisions were assessed by performing high-resolution x-ray measurements on targets of Al, Ti, V, Co, and Cu with a curved crystal spectrometer.

The results of the high resolution measurements revealed that the apparent average L-shell spectator vacancy fraction at the time of Kα x-ray emission, p_L , may be represented by a universal function of the Geometrical Model's parameter X for Z_2 = 17 - 32.

Multiple-vacancy Kα fluorescence yields and corrections for K-shell ionization by secondary processes were determined with the aid of the high resolution spectra for the

targets Al, Ti, and Cu. Fluorescence yields for the other targets were determined using an extrapolation procedure.

The resulting K-vacancy production cross sections for 2.5 to 6 MeV/amu projectiles were compared with a limited amount of available experimental data and shown to be in relatively good agreement.

The ECPSSR predictions for all the targets except Al agreed reasonably well with experimental cross sections for Ar projectiles. The experimental cross sections for K-vacancy production in Al, Ti, Cu, Zr, and Ag were greatly deviated from the ECPSSR predictions. The cross sections for Kr on Sm and Ta were in good agreement with theory.

The scaling properties of the Kα x-ray production cross sections were examined and a semiempirical "universal" curve was deduced that reproduces the measured cross sections to within ±30% on average.

The relationship between the Kα x-ray production cross sections and the geometrical model's universal variable also was examined.

ACKNOWLEDGMENTS

It is a pleasure to thank the following coworkers and friends whose patience and encouragement made my stay at the Cyclotron Institute very enjoyable.

It is difficult to overstate my gratitude to Dr. Rand L. Watson, my advisor, for his constant support, encouragement and guidance throughout this research project. His own enthusiastic and conscientious attitude towards work, methodical approach to a problem, cautious experimentation and attention to details, and critical technical writing have made me realize the significance of these traits in any type of endeavor. His patience and understanding during my research of this project were also deeply appreciated. His enthusiasm, his inspiration, and his great efforts to explain things clearly and simply helped to make this project fun for me. I would have been lost without him.

I would also like to thank my research colleague, Dr. Vladimir Horvat, for his invaluable assistance with the experiment, discussions, data analysis, and dissertation corrections. Whenever I faced problems, his help was always there.

Special thanks must be given to Dr. Wei Liu and Mr. Lijun Qing for the discussions and their help during my thesis writing. Mr. Qing is not only an expert in software but also in hardware. His help greatly improved my research progress.

I also acknowledge Mr. John Goodwin and Miss Sera Wuenschel for their help in my thesis writing. Officemates deserve my thanks for the discussions.

My greatest gratitude goes to the entire Cyclotron staff and personnel for their

assistance all the time. The support from the Welch Foundation is gratefully acknowledged.

My special thanks to my wife, Hongyu Liu, and my daughters, Jenny, Emily, and Zoey, whose love and support have been an inspiration in all the aspects of my life.

Finally, and most importantly, my very special thanks to my wonderful parents to whom I owe everything. Without their constant encouragement and love, this would have never become reality. I am honored to dedicate this dissertation to them.

TABLE OF CONTENTS

Page

Page

Page

LIST OF FIGURES

FIGURE Page

FIGURE Page

FIGURE Page

FIGURE Page

LIST OF TABLES

TABLE Page

CHAPTER I

INTRODUCTION

1.1. Overview

The study of ion-atom collisions plays an essential role in developing new models for ion-atom interactions and in providing important atomic data and cross sections for other areas of science, such as atomic physics, astrophysics, plasma physics, elemental analysis, medical research, environmental protection, and industrial processing (see references [1-6]).

The work described in this dissertation focuses on K-vacancy production cross sections and the probability of simultaneous L-shell ionization in heavy ion-atom collisions. The theoretical description of inner-shell vacancy production in fast heavy ion-atom collisions is an extremely challenging problem due to its many-body nature and because multiple mechanisms contribute to the process. Development of a detailed understanding of K-vacancy production in ion-atom collisions requires knowledge of the systematic behavior of cross sections for electron excitation, ionization, and capture, along with the rate constants for radiative, nonradiative and collisional decay of the various excited states produced in both collision partners. So far, rigorous treatments

---

The citations in this dissertation follow the format of the Physical Review A.

that account only for the interactions between a single active target electron and a bare projectile nucleus have been attempted. While methods based upon the Born approximation, such as the semiclassical approximation (SCA) [7-12] and the perturbation stationary state approximation (PSS), which incorporates the increased binding and polarization effects of the projectile, along with corrections for projectile energy loss (E), Coulomb deflection (C) effects in the projectile trajectory, and relativistic (R) effects (ECPSSR theory) [13-18], have been reasonably successful at predicting ionization cross sections for projectiles of low atomic number (e.g., $Z_1 < 10$), they have been found to greatly overestimate the ionization cross sections for heavy ions [19, 20]. Therefore, a detailed experimental examination of the dependence of inner-shell vacancy production cross sections on projectile energy and atomic number, and on target atomic number, is warranted to stimulate further theoretical progress and to develop semiempirical methods of prediction.

Inner-shell ionization produced by heavy ion-atom collisions has been an intensely active area since the early 1960's due to the availability of modern particle accelerators and developments in x-ray and electron detection technology, data acquisition techniques, and computational facilities. Target atom inner-shell vacancies are created in ion-atom collisions mainly via two processes: i) Coulomb direct ionization, in which bound electrons of the target atom are ejected into the continuum, and ii) the capture of target electrons into the projectile. Subsequent de-excitation of the inner shell vacancy states produced in ion-atom collisions occurs either by radiative or nonradiative transitions. Additional vacancies can be created as a result of Auger and Coster-Kronig

transitions, or as a consequence of shake-up and shake-off processes. The energies of x-rays emitted from such multiply ionized atoms are shifted with respect to the corresponding x-ray energies of singly ionized atoms and reflect the configuration of electrons at the time of x-ray emission. The resulting x-ray spectra typically consist of a large number of closely spaced satellite lines corresponding to configurations having multiple vacancies. Satellite lines usually occur at higher energies than the normal (single vacancy) lines due to the increased binding of the remaining electrons.

1.2. Survey of previous work

The accurate prediction of inner-shell vacancy production cross sections has been a long-standing goal of ion-atom collision physics. Many experimental investigations concerning target atom inner-shell ionization in light ion ($Z_1 \leq 2$) collisions have been carried out over the past three decades and a large database of cross sections for light ion collisions, spanning a large range of relative velocities and target atomic numbers, has accumulated [21]. These data are well described by the ECPSSR theory [14-18, 22-24]. However, very little data is currently available for collision systems in which the projectile atomic number is greater than 10.

Myerhoff et al. [25-32] performed a comprehensive survey of target and projectile K vacancy production cross sections in the 1970's. They used projectiles of Br, Kr, I, Xe, and Pb spanning the energy range 0.1 to 4 MeV/amu incident on a large number of targets throughout the periodic table and identified various mechanisms of inner shell ionization. In symmetric collisions ($Z_1/Z_2 \approx 1$) at low velocities ($v_1/v_{2K} < 1$, where v_1 is

the projectile velocity and v_{2K} is the average target atom K electron velocity), the vacancy production cross sections were described by a molecular orbital model [33-36]. In this model, the target and projectile atomic K orbitals combine in near-symmetric collisions forming 2pσ and 1sσ diatomic molecular orbitals as they approach each other. During the incoming part of the collision, vacancies may be produced in the 2pσ orbital by direct excitation or by rotational coupling with the 2pπ orbital. On the outgoing part of the collision, these vacancies are shared between the two K shells according to the relative asymmetry of the two collision partners. The K-vacancy cross sections for the higher(H)- and lower(L)-Z collision partners are given by

$$\sigma(H) = \sigma(1s\sigma) + \omega\sigma(2p\sigma) \tag{1}$$

$$\sigma(L) = (1-\omega)\sigma(2p\sigma) + \sigma_{K-L} \tag{2}$$

where $\sigma(1s\sigma)$ is the cross section for $1s\sigma$ vacancy production by direct (Coulomb) ionization, $\sigma(2p\sigma)$ is the $2p\sigma$ vacancy production cross section, ω is the probability that a $2p\sigma$ vacancy will end up in the 1s level of the heavy partner on the outgoing part of the collision [37-39], and σ_{K-L} is the contribution from K-L level matching effects when the 1s(L) level approaches the 2p(H) levels [27]. They found that the cross sections were dominated by the sharing of the $2p\sigma$ vacancies near symmetry while for more asymmetric collisions, the lower-Z partner profited from K-L level matching. In highly asymmetric collision, the higher Z partner obtained vacancies solely by direct $1s\sigma$ excitation. The MO model is successful in describing low energy and nearly symmetrical collisions, but it is not valid for collisions in which $v_1/v_{2k} \geq 1$.

Anholt et. al. [40-47] studied inner-shell ionization in collisions with relativistic Xe and U projectiles with energies ranging from 82 to 300 MeV/amu and 105 to 955 MeV/amu, respectively. The ionization, excitation, radiative decay, radiative electron capture (REC) and nonradiative electron capture (NRC) processes were studied in detail. They also investigated the effects of relativistic wave-functions, target-atom screening, and transverse-excitation [40, 41, 48] on the K-shell ionization cross sections as well as the influence of excited states of the projectile on the charge states of relativistic heavy ions in solids. The measured electron capture cross sections in comparison with calculations of radiative and nonradiative capture showed that nonradiative capture into excited states of the projectile was dominant in high-Z targets. The results of charge-state, x-ray, and radiative capture photon measurements were found to be in good agreement with predictions based on the plane wave Born approximation (PWBA).

Liatard et al. [49] carried out measurements on solid targets ranging in Z_2 from 27 to 90 using 30 MeV/amu Ne and Ar projectiles. Their results showed good overall agreement with the predictions of the CPSSR theory (an earlier version of the ECPSSR theory, which did not take into account energy loss) but displayed small systematic deviations from the theoretical projectile and target-Z dependences. It was also shown that K-electron capture to the projectile contributed significantly to the total K-shell ionization cross sections for Ar.

Cross sections for K x-ray production in solid targets (Z = 13, 22, 26, 29, 32, 40, 42, 46, and 50) by 30 MeV/amu beams of H, N, Ne, and Ar were reported by Horvat et al [50]. The deduced K-shell-ionization cross sections for H, N, and Ne projectiles agreed

quite well with the predictions of the ECPSSR but large deviations were observed for Ar projectiles on high Z targets from $Z_2 = 26$ to 40.

Zou et al. [51] performed studies of K x-ray yields from argon projectiles, with energies between 1 MeV/amu and 7.5 MeV/amu, passing through solid targets having atomic numbers varying from 6 to 74. The dependence on Z_2 of the Ar Kα hypersatellite to Kα satellite x-ray intensity ratio was described by the molecular orbital model in near symmetric and low energy collisions while it was described by the direct Coulomb processes in high energy collisions. The average L-shell vacancy probability showed a similar dependence on Z_2 but no dependence on the projectile energy was observed.

Kravchuk et al. [52] investigated zero impact parameter collisions of carbon and neon projectiles at energies of 8.3 MeV/amu and 30 MeV/amu, respectively, with solid targets from Ag to Th. The results showed good agreement with SCA calculations in both the separated atom approximation and the united atom approximation. In another experiment [53], it was shown that K x-ray production cross sections, induced by 20 MeV/u He, C, O, and Ne beams on Ta, Pb, and Th targets as well as 80 MeV/u He, C, O beams on a Pb target, were within 10% of the theoretical PWBA-BCPR model predictions (PWBA including corrections for the increased binding and polarization effects, Coulomb deflection, and relativistic effects). They also observed that the deduced probabilities of simultaneous L-shell ionization increased significantly as a function of the projectile atomic number in the case of 20 MeV/amu projectiles whereas in the case of 80 MeV/amu projectiles there was only a slight increase. The degree of simultaneous L-shell ionization was relatively small in the reactions studied with less

than one L-shell hole created on average.

In two recent studies [19, 20], the projectile Z_1 dependence of K vacancy production in Cu and Al targets was investigated using 10 MeV/amu projectiles over a range of Z_1/Z_2 extending from 0.34 to 6.38. The velocity ratio v_1/v_{2K} for these collision systems was 0.79 and 1.87 for Cu and Al, respectively. It was found that beyond $Z_1 = 18$, substantial contributions to the measured K x-ray yields were attributable to secondary processes (e.g., photoionization and ionization by secondary electrons). In addition, the measured K-vacancy production cross sections fell far below the values predicted by the ECPSSR [23]. In the case of the Al measurements, large deviations between the ECPSSR predictions and the experimental results were observed beyond $Z_1 = 10$, with the theoretical cross sections rising much faster as a function of Z_1 than the experimental cross sections. At $Z_1 = 83$ (Bi), the Al theoretical cross sections were a factor of fifteen larger than the experimental cross sections. In the case of the Cu measurements, the K vacancy production cross sections were found to saturate beyond $Z_1 = 54$, while the ECPSSR cross sections rose above the experimental cross sections beyond $Z_1 = 18$ and deviated from them by a factor of 18 at $Z_1 = 83$. These results were significant in two respects: i) they demonstrated that K vacancy production by secondary processes must be taken into account if accurate experimental values of cross sections for K-vacancy production by high Z_1 projectiles are to be obtained, and ii) they underlined the fact that a theoretical method capable of providing even rough estimates of cross sections for K vacancy production in high Z_1 heavy ion collisions is not yet available.

1.3. Scope of the present work

The primary objectives of the present work were to generate a body of K-vacancy production cross section data of sufficient accuracy and extent to encourage further development of more reliable theoretical methods, and to use this database as a means of establishing an empirical scaling law capable of systematizing cross sections for a wide variety of collision systems. In order to accomplish these objectives, measurements of target K x-ray yields excited in collisions of Ar, Kr, and Xe ions having energies of 2.5, 4, 6, 10, 15, 20, and 25 MeV/amu with self-supported foil targets of Al, Ti, Cu, Zr, Ag, Sm, and Ta have been performed. In addition to the K x-ray production cross section measurements, it was necessary to perform high resolution spectral measurements with a curved crystal spectrometer in order to correct the x-ray yields for contributions from secondary process.

A survey of collision systems involving projectiles with $Z_1 \geq 6$ that have been examined in previous work is shown in Fig. 1. The collision systems investigated in the current work are indicated by the colored data points. As this figure shows, the present measurements considerably expand the explored range of Z_1/Z_2 and v_1/v_{2K}.

In order to accomplish the objectives of the current investigation, several challenging problems had to be overcome. The determination of an accurate efficiency curve for the Si(Li) detector at x-ray energies below 6 keV is difficult because there are no suitable radioactive calibration sources available in this energy range. However, it has been well established that the ECPSSR calculations agree with the experimental proton ionization cross sections within 10% and hence the Si(Li) detector efficiency could be determined

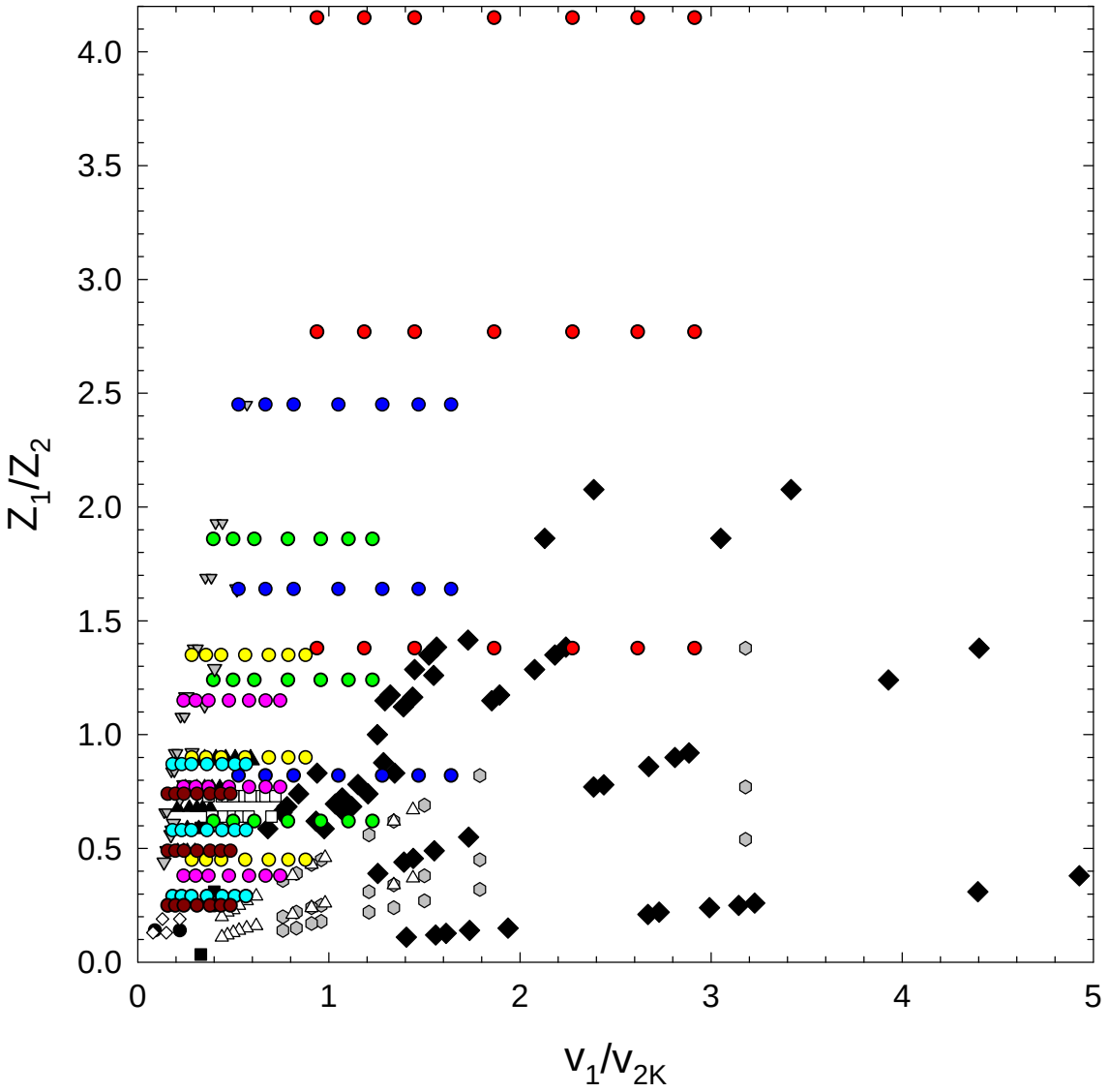

FIG. 1. Collision parameters of measured cross section for K-shell vacancy production by heavy ions; shaded triangle [29], filled diamonds [40], open triangles [49], shaded hexagons [50], filled circles [54], filled squares [55], filled triangles [56],open squares [57]. The present collision systems are shown by the colored points; solid red circles = Al, solid blue circles = Ti, solid green circles = Cu, solid yellow circles = Zr, solid magenta circles = Ag, solid cyan circles = Sm, and solid brown circles = Ta.

by measuring x-ray yields produced by 10 MeV/amu protons and comparing them with ECPSSR cross sections.

Another difficulty was encountered in determining accurate K x-ray yields for aluminum and titanium targets when krypton and xenon projectile beams, respectively, were employed due do the overlap of krypton and xenon L x-rays with the aluminum and titanium K x-rays. Accurate methods had to be developed for subtracting the contributions of the interfering x-rays. Finally, conversion of the measured x-ray production cross sections to K vacancy production cross sections required knowledge of the fluorescence yields. Because the K x-rays produced in heavy-ion collisions are emitted from atoms that have additional vacancies in the L- and higher shells, tabulated fluorescence yields for single vacancy atoms are not appropriate. A solution to this challenging problem is discussed in Chapter IV.

This dissertation is organized as follows. In the second chapter, a brief introduction of theoretical methods, including PWBA, ECPSSR, SCA, BEA, the geometrical model (GM), and molecular orbital theory (MO), for computing K-shell vacancy production cross sections is presented. Chapter III describes the experimental methods used to measure the K-x-ray yields with a Si(Li) detector and the high resolution measurements with a curved crystal spectrometer. Descriptions of the detector calibration methods are also presented in this chapter. In the fourth chapter, details of inner-shell vacancy decay including nomenclature and energy level diagrams are presented along with a discussion of x-ray spectra and fluorescence yields for multiply ionized atoms. The data analysis procedure, including corrections applied to the measured x-ray yield to account for

contributions from secondary processes, are presented in the fifth chapter. Chapter VI contains a discussion of the results and the conclusions are presented in Chapter VII.

CHAPTER II

THEORIES OF INNER SHELL IONIZATION

Several theoretical methods have been developed to describe the process of inner-shell ionization in heavy ion-atom collisions by utilizing different approximation methods. In this chapter, a brief review of some of these methods is presented with emphasis on details of relevance to calculation of K-shell vacancy production cross sections.

The Plane Wave Born Approximation (PWBA) [54-56] has played a key role in the development of the various theoretical methods and is introduced in Section 2.1. This is followed (Section 2.2) by a discussion of the ECPSSR theory [14-18, 22-24], one of the improved approaches of PWBA. Then, the semiclassical approximation (SCA) [7-10, 57] and the classical Binary Encounter Approximation (BEA) [58-61] methods are presented in Section 2.3 and Section 2.4, respectively. The Geometrical Model (GM) [62-64] is discussed in Section 2.5 while the molecular orbital theory (MO) is presented in Section 2.6.

The approximate regions of the validity for the PWBA, SCA and Molecular Orbital (MO) model are shown in Fig. 2 (taken from ref. [65] p.59). The current study is focused on the region of $0.25 \le Z_1 / Z_2 \le 4.15$, and $0.16 \le v_1 / v_{2K} \le 2.89$, marked as a red rectangle in Fig. 2.

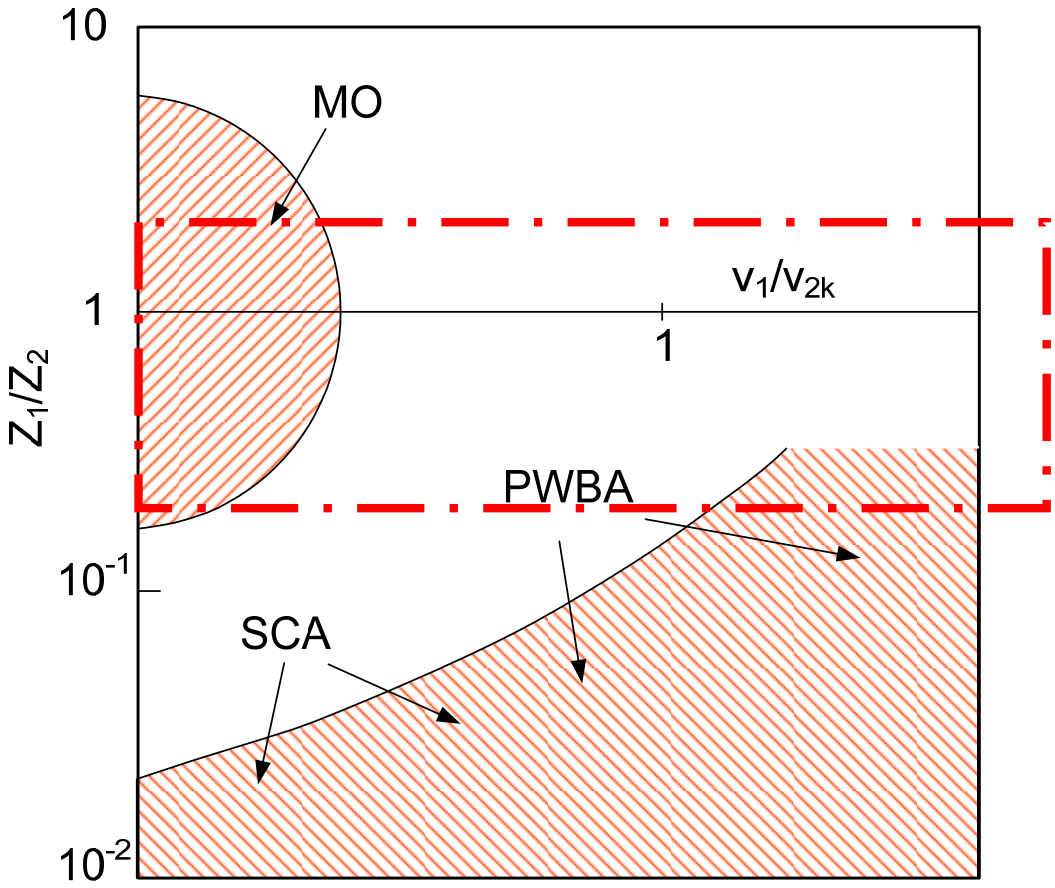

FIG. 2. Regions of validity for various approximation schemes as a function of the projectile-to-target nuclear charge ratio, Z_1/Z_2, and the projectile to the target K electron velocity ratio, v_1/v_{2K}. Shaded regions are shown for the Plane-Wave-Born-Approximation (PWBA), the semiclassical approximation (SCA), and the molecular orbital model (MO) (Reprinted from reference [65] p.59). The red rectangle outlines the region covered by the present investigation.

2.1. The plane wave Born approximation

PWBA is a quantum perturbation method in which the first Born approximation is used to describe the interaction between the projectile and the target. This method is generally valid when [56, 66]

$$\frac{Z_1 e^2}{h v_1} = 1, \tag{3}$$

where Z_1 is the projectile atomic number, v_1 is the projectile velocity, and $e^2/\hbar$ is the speed of the electron in a hydrogen atom. In addition to the condition of Eq. (3), it is assumed that i) the interaction between the projectile and the target electron is very weak, ii) the target electron appears "frozen" during the collisions because the response time of the electrons is long compared to the interaction time, and iii) the projectile acts as a point charge and its electronic structure has a negligible effect on the interaction [14].

Details of the evaluation of the cross section for ionization employing the PWBA can be found in reference [65]. The result for K-shell ionization is given by the formula [14, 56, 66]

$$\sigma_K^{PWBA} = \left(\sigma_{0K} / \theta_K\right) F_K\left(\frac{\eta_K}{\theta_K^2}, \theta_K\right), \tag{4}$$

where σ_{0K} is

$$\sigma_{0K} = 8\pi a_0^2 \left(Z_1 / Z_{2K}\right)^2, \tag{5}$$

in which $a_0 = 0.5291771$ Å is the Bohr radius, and $Z_{2K} = Z_2 - 0.3$ is the screened target

nuclear charge. In Eq. (4), θ_K measures how much the K-shell ionization energy exceeds that of a hydrogenic atom and is given by

$$\theta_K = U_K / Z_{2K}^2 \Re_\infty , \tag{6}$$

where U_K is the K-shell binding energy and $\Re_\infty = 13.6\ \text{eV}$ is the Rydberg constant. The reduced particle-velocity parameter, η_K, in Eq. (4) is given by

$$\eta_K = \left(\frac{v_1}{v_{2K}} \right)^2 . \tag{7}$$

Extensive tables of values of the function F_K in Eq. (4) have been tabulated for the K- and L-shells by Khandelwal and Choi [67, 68].

Scaled K-shell ionization cross sections as a function of the reduced velocity parameter η_K are shown in Fig. 3(taken from reference [56]). The different curves represent different values of the screening parameter θ_K.

PWBA is in good agreement with experiment for light projectiles at high velocities. However, various improvements have been suggested to overcome the limitations of this theory. Examples are the Distorted Wave Born Approximation (DWBA) (see a review by Rudd et al. [69]) that includes the interaction between the projectile and the target nucleus, the Continuum-Distorted-Wave method (CDW) [70, 71] in which Coulomb interactions are explicitly contained in the initial- and final-state wave functions, etc.. Corrections for Coulomb repulsion [15], projectile energy loss [11, 72, 73], relativistic effects [9, 74-77], and binding polarization effects [14, 15, 17] led to the well-known ECPSSR theory.

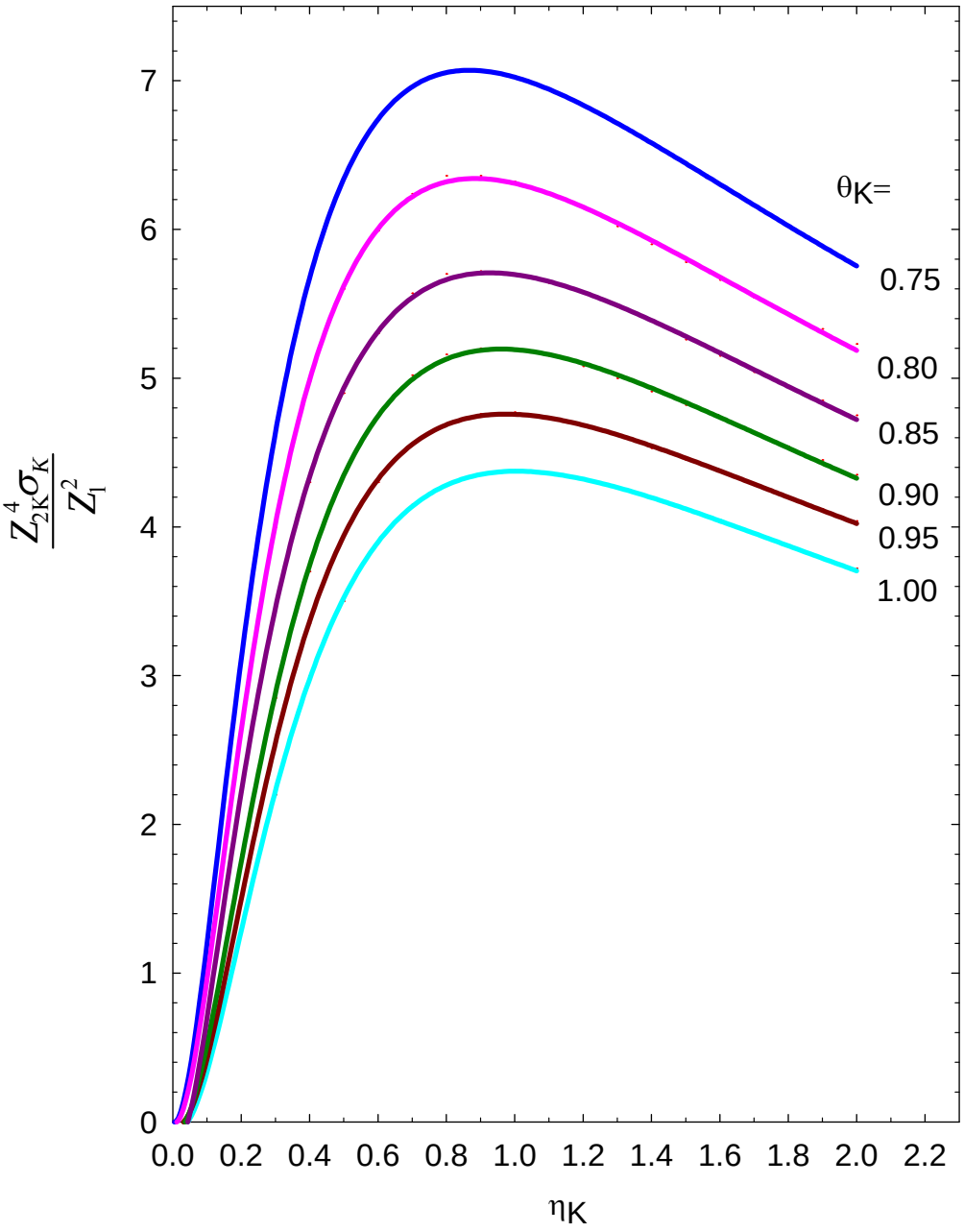

FIG. 3. PWBA predictions of K-shell ionization as a function of the reduced velocity parameter η_K (reproduced from reference [56]).

2.2. The perturbed stationary state approximation

The ECPSSR theory goes beyond the first-order perturbative treatment and is the most advanced approach based on the PWBA. It includes corrections for projectile energy loss (E), Coulomb deflection of the projectile trajectory (C), binding and polarization effects within the perturbed stationary state (PSS) of the target electron, and relativistic (R) effects. The Coulomb deflection correction is very important for low-energy projectiles. The binding effect refers to the increased binding experienced by the electron at small impact parameters when it is in the combined field of the projectile and target nuclei. The polarization effect refers to the distortion of the electron wave function by the projectile at impact parameters greater than the electron shell radius.

In addition to the above mentioned corrections, ECPSSR also takes into account vacancy production via electron capture to the projectile based on the Oppenheimer-Brinkman-Krames (OBK) formula [78-81].

Details of the ECPSSR theory and examples of calculation procedures can be found in references [23, 82]. The ECPSSR cross section for K-shell ionization is formulated in terms of σ_K^{PWBA} from Eq. (4) [82] as

$$\sigma_K^{ECPSSR} = C_{BK}^{E}(dq_{0K}\zeta_K)\sigma_K^{PWBA}\left(\frac{m_K^R\left(\frac{\xi_K}{\zeta_K}\right)\eta_K}{(\zeta_K\theta_K)^2}, \zeta_K\theta_K\right), \tag{8}$$

where C_{BK}^{E} represents the Coulomb deflection correction, the quantity $d = Z_1Z_2/(\mathrm{Mv}_1^2)$ is the half distance of the closest approach in a head-on collision, q_{0K} represents

approximate minimum momentum transfer (U_{2K}/v_1), ζ_K is the correction factor for binding and polarization effects, m_K^R is the relativistic correction factor, and ξ_K is the redefined reduced projectile velocity, given by $2v_1/\theta_K v_{2K}$.

It has been shown that ECPSSR calculations agree with experimental results within 10% to 20% for proton and alpha particle bombardment of targets in the range $10 \leq Z_2 \leq 92$ [83].

2.3. The binary encounter approximation

The binary encounter approximation (BEA) assumes that ionization is completely due to a classical binary encounter between the charged projectile and the target electron. The target nucleus and the rest of its electrons are assumed to play no role in the process, except for providing the initial momentum distribution and binding energy of the ejected electron.

A detailed analysis of the classical Coulomb interaction between two moving charged particles was given by Gryzinski [84-86]. Rudd et al. [87] extended the theory by using a quantum-mechanically derived velocity distribution for the target electron.

The expression for the K-shell ionization cross section [84-86, 88] is given by

$$\sigma_K(E_i) = \frac{N_K Z_1^2 \sigma_0}{U_{2K}^2} G(V), \tag{9}$$

where U_{2K} is the electron binding energy, $\mathrm{N_K}$ is the number of electrons in the K-shell and σ_0 is (see Ref. [86] Eq. 20)

$$\sigma_0 = \pi e^4 Z_1^2 = Z_1^2 6.56 \times 10^{-14} \text{cm}^2\text{eV}^2. \quad (10)$$

The term G(V) is a function of the reduced velocity $V = v_1 / v_{2K}$, and it is given in references [84-86, 88]. The BEA predicts that the product of the binding energy squared and the ionization cross section divided by the projectile atomic number squared is a universal function of the reduced velocity V.

Fig. 4 (taken from reference [65] p. 87) shows a comparison of the BEA predictions, the PWBA predictions, and experimental measurements of K-shell ionization cross sections for proton impact as a function of $E/\lambda U_K$, where λ is the ratio of the electron to proton masses. The PWBA assumes that the interaction between the incident particle and the atom is weak thus the interaction is quantum mechanically treated (as a perturbation), while the BEA treats the collision classically as an incident particle and a free electron with an artificial velocity distribution.

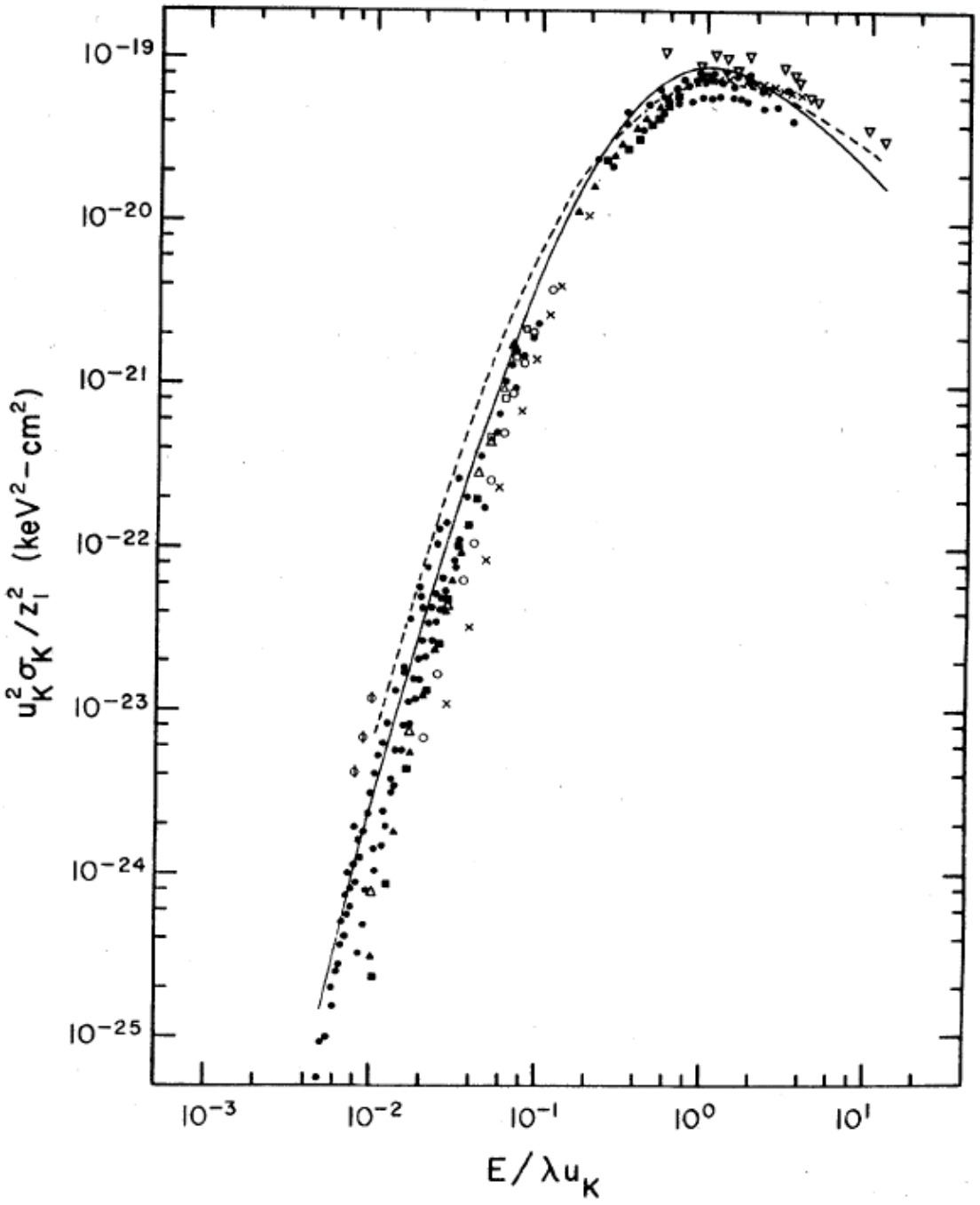

FIG. 4. Comparison of the PWBA, the BEA, and experimental K-shell ionization cross sections for proton impact: dashed curve, PWBA; solid curve, BEA. (Taken from reference [65] p. 87).

2.4. The semiclassical approximation

The semiclassical approximation (SCA) [7-10, 57] was introduced by Bang and Hansteen [7], who calculated the K-shell ionization cross sections for heavy ion-atom collisions for low projectile energy. The SCA enables one to investigate the details of the collision process as a function of impact parameter. It can be derived from the basic principles of quantum mechanics (first-order time-dependent perturbation theory) in a relatively straight-forward way. so that the number of parameters introduced in a more or less artificial manner is minimized. The SCA takes into account the Coulomb repulsion between the projectile and the target by assuming a hyperbolic trajectory for the incident projectile. For high projectile energies, SCA is equivalent to PWBA [7, 89-91].

The differential cross section for the ionization of an atomic electron with a final energy E_f, as given by first-order time-dependent perturbation theory, is [7, 89]

$$\frac{d\sigma}{dE_f} = \frac{2\pi}{\hbar^2}\int_0^\infty bdb \left| \int_{-\infty}^{\infty} e^{i\omega t} < \psi_f \left| V(r,t) \right| \psi_i > dt \right|^2 , \qquad (11)$$

where b is the impact parameter and $\omega = (E_f + u_i)/\hbar$, u_i being the binding energy of the electron in the initial bound state, and E_f denoting the final state energy of the electron. The quantity V(r,t) is the time-dependent Coulomb potential between the projectile and the target electron, and Ψ_i and Ψ_f are the one-electron states in the self-consistent field, as only one-electron excitation is possible in the first order theory. The ionization probability, I_b, as a function of impact parameter b is thus given by

$$I_b = \int_0^{E_{\max}} \left(\frac{dI(b)}{dE_f} \right) dE_f \ , \tag{12}$$

where

$$\frac{dI(b)}{dE_f} = \left| a_{E_f,i}(t \to \infty) \right|^2 , \tag{13}$$

where $a_{E_f,i}(t \to \infty)$ is an excitation amplitude given by [8]

$$a_{E_f,i}(t \to \infty) = -i/\hbar \int_{-\infty}^{\infty} dt e^{i\omega t} \left\langle E_f \left| \frac{-Z_1 e^2}{|r - R_b(t)|} \right| i \right\rangle . \tag{14}$$

Tabulation of the matrix elements in Eq. (11) can be found in Ref. [7].

Instead of using hydrogen-like wave functions for the bound electron, Trautmann et al. [9-12, 70, 71, 92] employed relativistic Hartree-Fock electron wave function. They also made corrections for binding and polarization effects, nuclear distortions, screening on projectile trajectory, and recoil effects. Reviews and corrections of the SCA can be found in reference [9, 12, 70, 71, 89, 92, 93] and the references therein. Those corrections were shown to significantly improve agreement between the theory and experiment.

2.5. The geometrical model

For heavy projectiles, the BEA and the SCA theories fail since their predictions of ionization probabilities exceed unity. The geometrical model (GM) [62-64] was developed to describe multiple ionization in heavy ion-atom collisions, involving strong perturbations. Within the framework of the single particle model (SPM) [94], the simultaneous inner and outer shell ionization processes are characterized by the inner shell ionization cross section and the ionization probability per electron for the outer shells at zero impact parameter. Details of the geometrical model (GM) can be found in references [62-64]. The coordinates and characteristic distances used in the geometrical model are shown in Fig. 5. The projectile-target nucleus impact parameter is denoted by B (taken to be zero for inner-shell ionization) while the distance between the projectile trajectory and the electron is denoted by b. The fraction of the electrons swept out by the projectile may be considered as the ionization probability per electron. Generally, the target electron ionization probability is given by

$$P_{nlm}(b) = \iiint \left|\Psi_{nlm}(\vec{r})\right|^2 \eta(b)\rho \mathrm{d}\rho \mathrm{d}z \mathrm{d}\varphi \,, \tag{15}$$

where $\vec{r}$ is the position vector, $\rho d\rho dz d\phi$ is the differential volume in cylindrical coordinates, and $\eta(b)$ is the efficiency function, which may be chosen to be given by

$$\eta(b) = \begin{cases} 0 & if \;\; b > b_0 \\ 1 & if \;\; b \le b_0 \end{cases}, \tag{16}$$

with b_0 given by the ionization cross section

$$b_0 = \left(\sigma / \pi\right)^{1/2}, \tag{17}$$

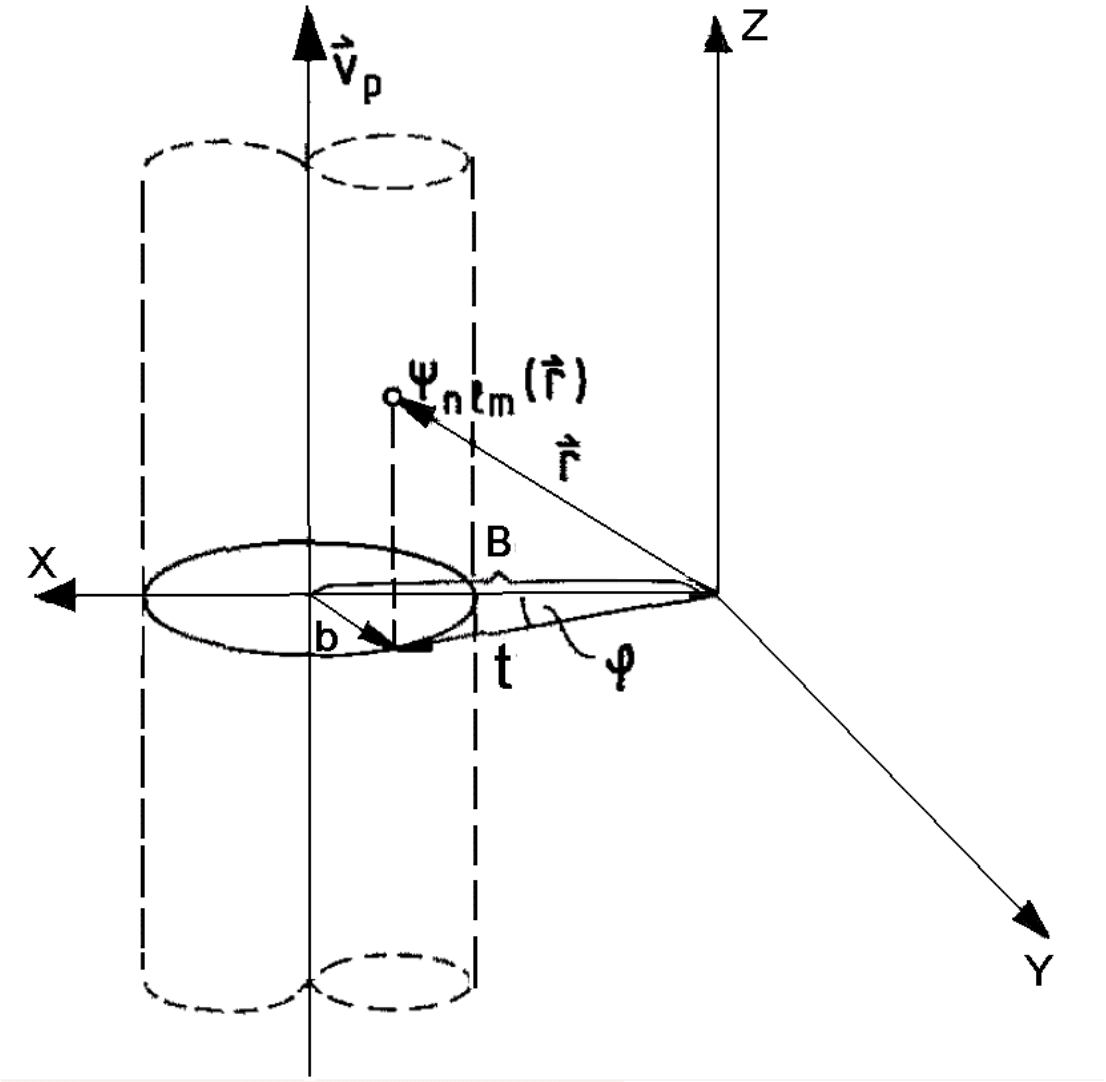

FIG. 5. Coordinates and characteristic distances used in the geometrical model.

If σ is derived from BEA [see Eq. (9)], then [63]

$$b_0 = \frac{Z_1 e^2}{v_1} V \left[\frac{2G(V)}{I} \right]^{1/2}, \tag{18}$$

where $V = v_1 / v_2$ is the reduced projectile velocity, G(V) is the BEA universal velocity function [88], and I is the experimental binding energy given by $v_2^2 / 2$.

The universal variable X is defined as

$$X = a_{nl} b_0, \tag{19}$$

where

$$a_{nl} = \frac{2}{Z_2 n} = 2\mathrm{v}_2 \tag{20}$$

is an atomic parameter. From Eqs. (18) , (19), and (20), the universal variable X can be written as

$$X = 4 \frac{Z_1}{v_1} \mathrm{V} \left[G(\mathrm{V}) \right]^{1/2} \tag{21}$$

In summary, the Geometrical Model predicts that the mean ionization probability per electron at a zero impact parameter depends only on the universal scaling parameter X. Experimental test of this model have been published in Refs. [95, 96].

2.6. The molecular orbital model

The molecular orbital (MO) model is used to describe ionizing collisions in which the projectile and target atomic numbers are comparable to each other while the velocity of the projectile is much smaller than the orbital velocity of the target electron. Madison and Merzbacher [97] outlined schematically regions of the validity of the separated-atom (SA) and molecular-orbital (MO) theories for atomic collisions as shown in Fig. 2. In the first Born approximation, the perturbation becomes increasingly large as the projectile velocity decreases (for $v_1/v_{2k} \approx 1$ and below), unless the Z_1/Z_2 ratio drops significantly below 0.1, so that the validity of the first Born approximation becomes restricted to asymmetric collisions in the fast-collision regime. On the other hand, slow and symmetric, or nearly symmetric, collisions are in the domain of applicability of the MO model, which takes into account the mutual distortion in the atomic orbitals of the collision partners. If two atoms collide slowly, inner shell electrons tend to adjust their orbital states adiabatically to the motion of the two nuclei, and Coulomb excitation or ionization becomes unlikely. During the collision, a quasimolecule is formed. Experiments on slow ion-atom collisions have shown that, under favorable conditions, inner-shell vacancies may nevertheless be produced with high probability. From a theoretical point of view, a partial understanding of this collision regime has been achieved through the application of ideas borrowed from the quantum theory of diatomic molecules [98, 99].

The model proposed by Fano and Lichten [100-103] for slow symmetric or near symmetric collisions assumes that (i) inner-shell electrons occupy independent-electron

MO's, (ii) these independent-electron MO's correlate with the same SA and united atom (UA) levels as the one electron hydrogenic MO, (iii) the effect of the other electrons is ignored except insofar as they screen the nuclear potential (i.e., correlation diagrams are constructed by drawing one-electron correlations but between the independent-electron levels of the many-electron atoms), (iv) excitation occurs most readily when promoted MO's become degenerate, or nearly degenerate, with MO's that contain vacancies, and (v) the Pauli principle enters only in a statistical way in deciding the initial occupation of MO's between which transitions take place. The conceptual simplicity of the Fano-Lichten model is exemplified in Fig. 6 for the symmetric collision system of Ar + Ar. This type of diagram is often referred to as a correlation diagram. During a collision, the bound independent electron states retain their validity in the two-center field of the projectile-target system. When the atoms are far apart, occupied inner-shell and unoccupied outer-shell levels interact weakly or not at all. As the inter-nuclear distance R changes during the collision, dramatic variations in the ordering of energy levels may take place and cause an occupied quasi-molecular state to interact strongly with one or more unoccupied electron states. Thus, an electron may be promoted from its occupied state to an unoccupied state, leaving a vacancy in the inner-shell. In Fig. 6, the levels at $R = \infty$ are those of the separated Ar atoms, while those at $R = 0$ are of the united Kr atom. Electron-electron interactions within the independent particle model cause transitions between diabatic molecular orbitals of like parity ($s \leftrightarrow s$, $s \leftrightarrow d$, $p \leftrightarrow p$, $p \leftrightarrow f$, etc.) and equal angular momentum λ ($\theta \leftrightarrow \theta$, $\pi \leftrightarrow \pi$, etc.). Rotational uncoupling causes

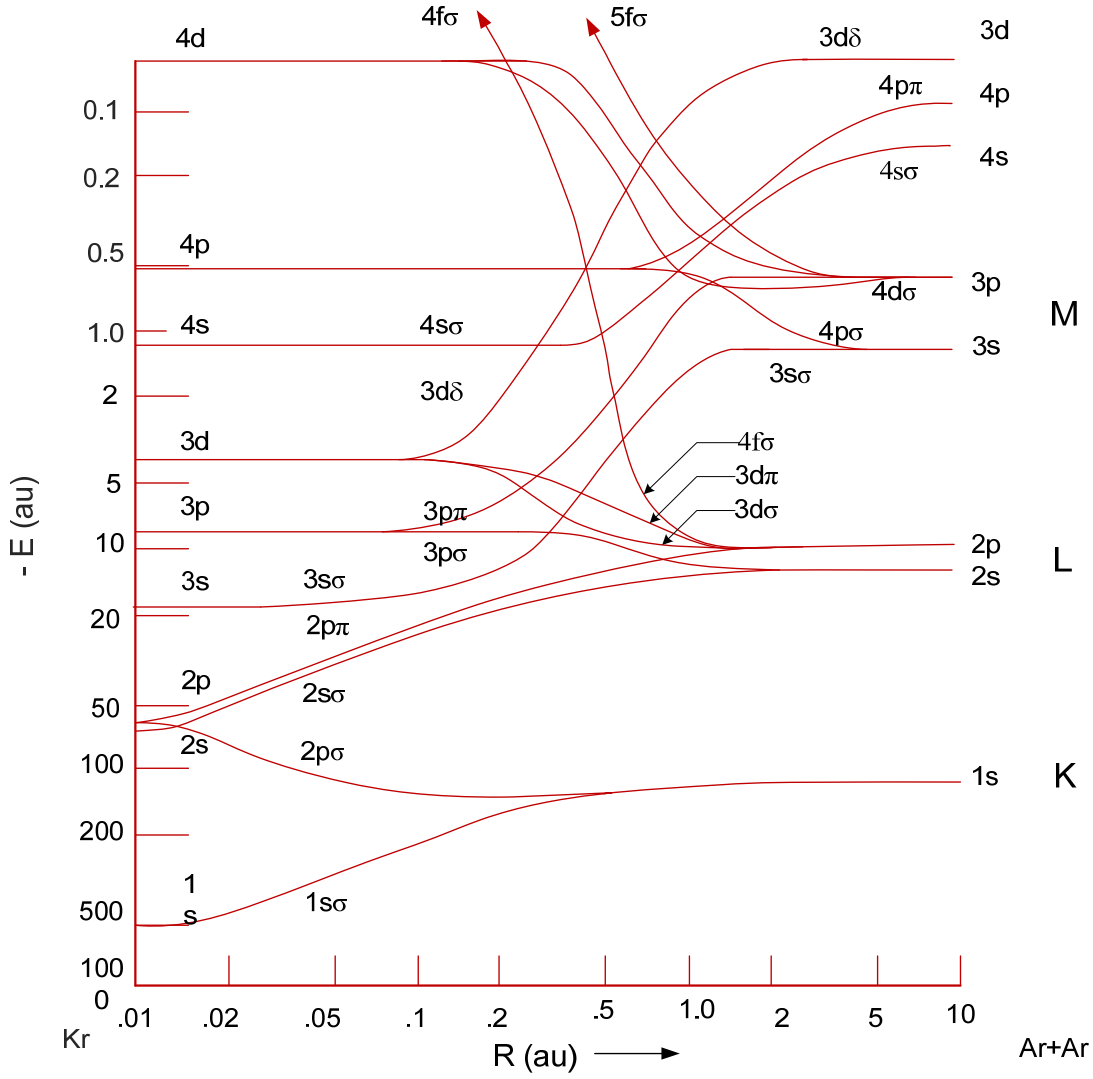

FIG. 6. Energy diagram for symmetric collision system (reproduced from Ref. [100]). This figure is for Ar on Ar.

transitions between molecular orbitals of like parity and $\Delta\lambda = \pm 1$, ($\theta \leftrightarrow \pi$, $\pi \leftrightarrow \delta$, etc.). Electron correlation (configuration interaction) allows two-electron, or (in the case of $\lambda \neq 0$) four-electron, transitions between pairs of molecular orbitals. As the atoms approach, all these effects cause transitions of M electrons into higher shells in the vicinity of R ~1-2 a.u. In the vicinity of R ~ 0.5 a.u., one 4fσ electron can be transferred to 4pσ or 3pπ (if the molecular orbital is not filled) or 4pπ. At crossings at smaller R, other L electrons can be transferred to higher shells. K-shell excitation can only occur at very small internuclear distances.

The Fano-Lichten model gives a reasonable interpretation of energy losses, inner-shell excitation, and characteristic internuclear distances for excitation and perturbation of elastic cross sections. In particular, the prediction of fast Auger-electron emission in hard collisions has been confirmed in detail by several experimental groups. Further confirmation of the predictions of the promotion model have come from observations of x rays in symmetric collisions by Saris et al. [104].

Following the successful use of these ideas in the analysis of Ar on Ar [100] and Ne on Ne [105] collisions, Barat and Lichten [101] applied them in detail to the more complicated cases of heteronuclear collisions. Such analysis now forms the framework of the understanding of inner-shell excitation in slow ion-atom collisions. It has been used successfully to interpret a wealth of experimental data where the formation of inner-shell vacancies has been monitored either by the observation of energy loss or by Auger electron or x-ray emission. Details of these experimental results and their interpretation in terms of the Fano-Lichten model may be found in Barat and Lichten

[101], Lichten [105], Garcia et a1. [58], Briggs [106], Lapicki and Lichten [107], Anholt [108, 109], and the papers of Meyorhof [25-27, 29, 31, 38, 39, 108, 110].

In Chapter VI, it will be demonstrated that the K x-ray production cross sections dramatically increase as the projectile atomic number approaches the target atomic number due to the formation of molecular orbitals. In this process, K vacancy production in the target atom and in the projectile ion is due to interactive level crossings that occur as the two collision partners dynamically combine to form a quasi molecule.

CHAPTER III

EXPERIMENTAL METHODS

Two different experimental setups were employed in the current work. One was for the cross section measurements with an energy-dispersive Si(Li) detector and the other was for the high resolution spectral measurements with a wavelength-dispersive curved crystal spectrometer. Accordingly, two major sections are presented in this chapter.

The first section describes the beam transport system. Then the energy-dispersive measurements, including the detectors and Si(Li) detector efficiency calibration, the targets, the determination of x-ray yields, and the data acquisition electronics and procedure, are presented.

A description of the wavelength dispersive measurements is presented in the second section, including Bragg reflection, the proportional counter, the targets, the curved crystal spectrometer, and the data acquisition procedures.

3.1. Beam transport system

A diagram of the Texas A&M University K500 superconducting cyclotron beam transport system is shown in Fig. 7 with details from the bending magnet (also called analyzing magnet or Maryland Magnet) positioned 2 m upstream to the target chambers. Heavy ion beams extracted from the cyclotron were directed through the analyzing magnet and on to the target chamber by means of a beam transport system, which

included a set of focusing quadrupole magnets and a set of horizontal and vertical steering magnets.

Beam focusing was attained by adjusting the quadrupole magnet currents while viewing the beam spot on a CdS-ZnS phosphorescent target ("phosphor") through a closed circuit TV monitor system.

3.2. Energy-dispersive measurements

The target absolute x-ray yields were measured in coincidence with the projectiles by using a Si(Li) detector to detect the K x-rays and a plastic scintillator combined with a photomultiplier tube to directly count the number of projectiles passing through the targets. Additional relative measurements were performed for the high Z (Ag, Sm and Ta) targets because their K x-ray production cross sections were too low to provide sufficient x-ray counting statistics at useable particle rates. A photograph and a schematic diagram of the experimental setup are shown respectively, in Fig. 8 and Fig. 9 for the coincidence measurements. Ion beams from the cyclotron passed through two 1-mm diameter collimators positioned respectively, 1.5 and 5.5 cm from the target. The target faced the beam and the Si(Li) detector both at 45 degrees. As shown in Fig. 9 beam particles passing through the target were detected by a plastic scintillator detector positioned 4 cm behind the target. The distance from the target to the Si(Li) detector Be window was 2 cm.

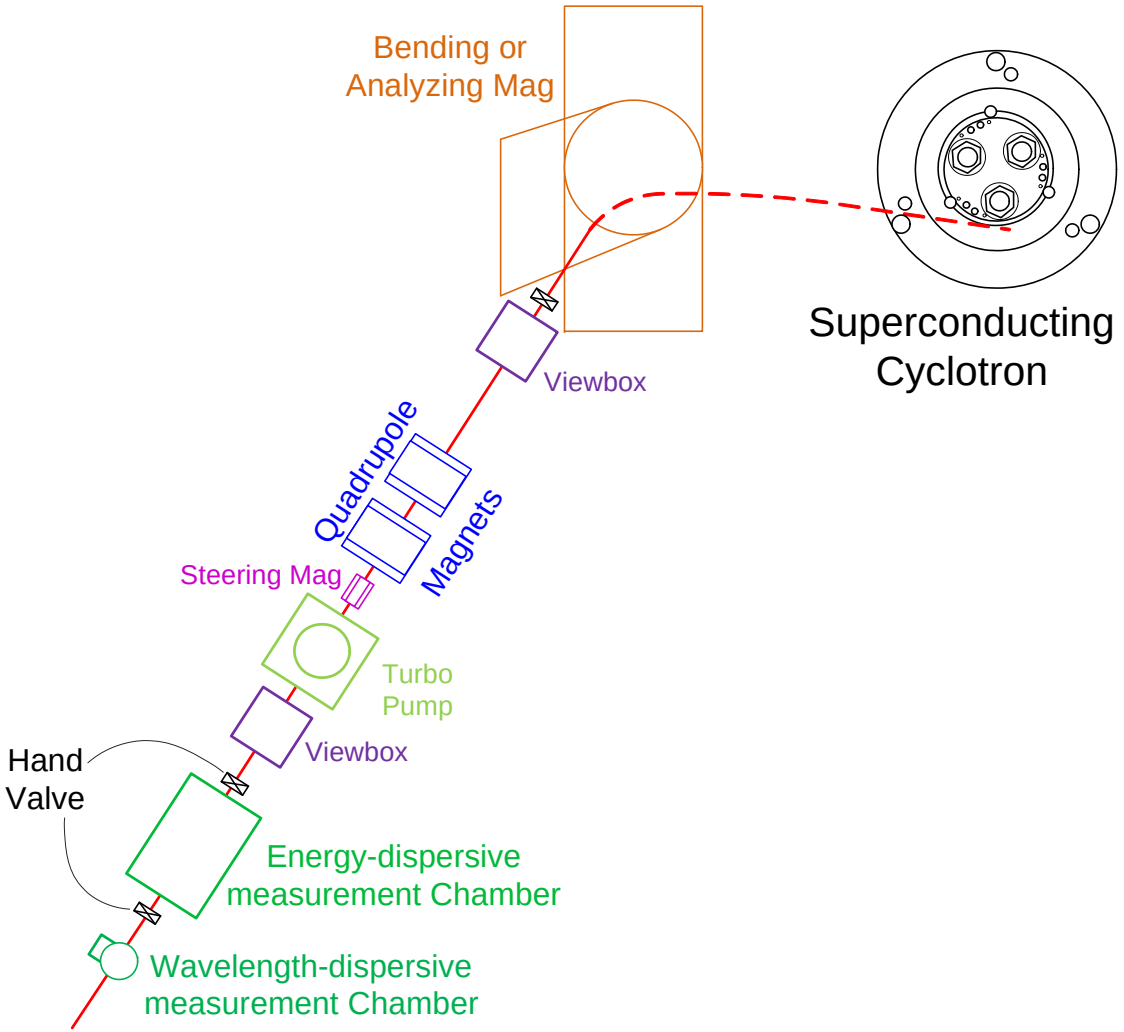

FIG. 7. Schematic beam transport system. Only details from the bending magnet to the target chamber are shown.

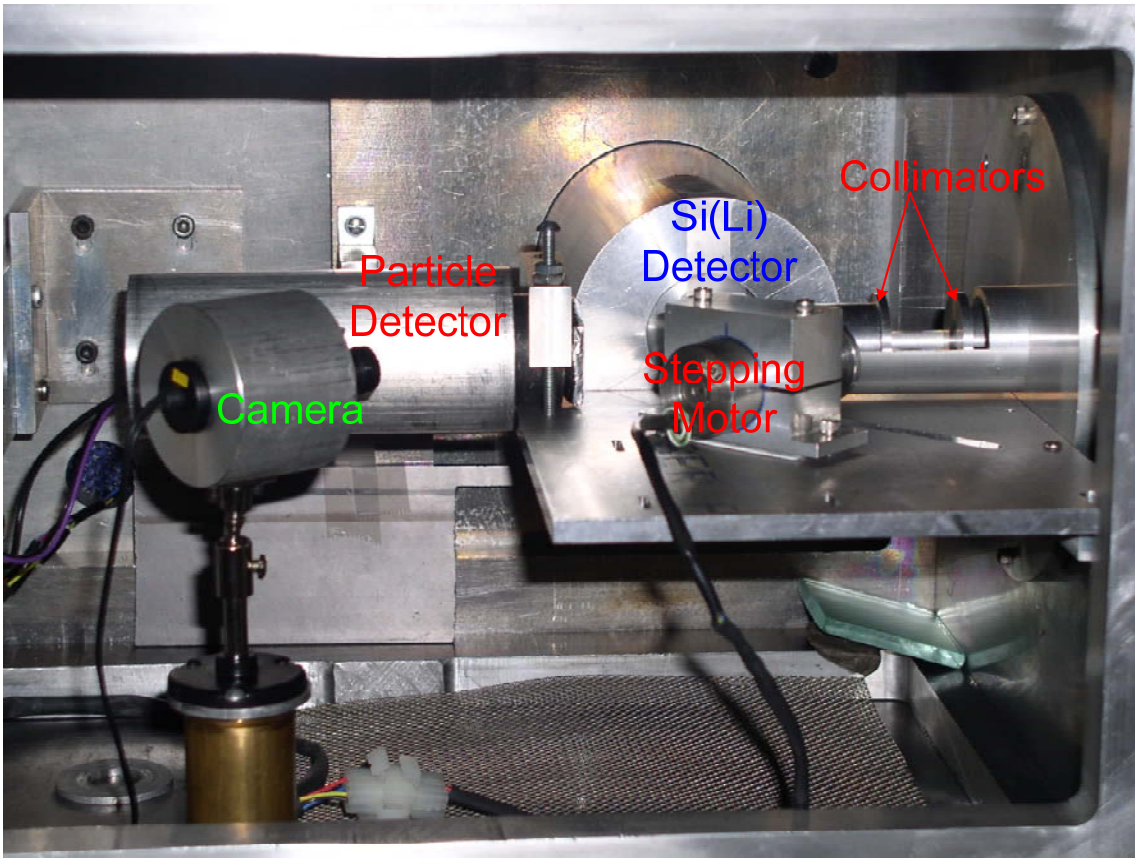

FIG. 8. Photograph of the experimental setup for the measurement of x-ray production cross sections.

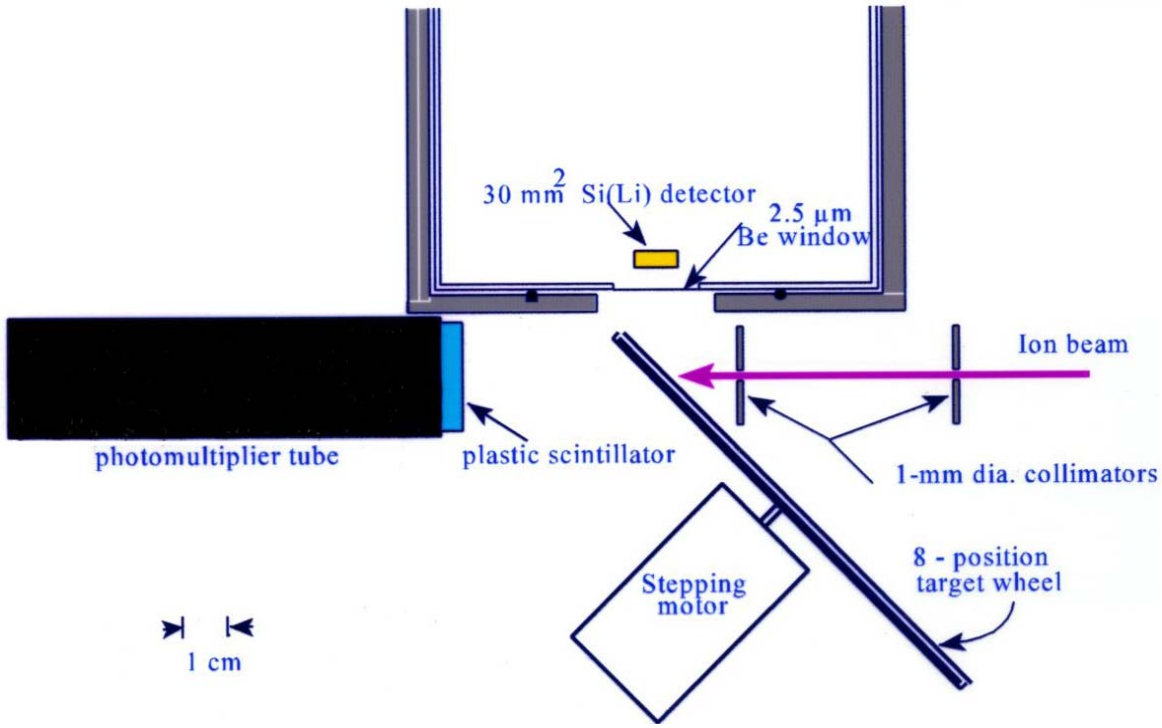

FIG. 9. Schematic view of the experimental setup for the measurement of x-ray production cross sections.

3.2.1. Targets

The targets used in the energy-dispersive measurements were mounted on an eight-position target wheel connected to a stepping motor that could be remotely controlled. This enabled changing from one target to another easily and reproducibly, without opening the vacuum chamber. The target wheel was oriented at a 45 degree angle with

respect to both the beam axis and the detector normal. Consequently, all stated thicknesses for these targets have been corrected for the 45 degree inclination angle. The targets were obtained from the Goodfellow Corporation, Berwyn, Pennsylvania, and their 45^0 thicknesses are listed in Table I. Two Sm and Ta targets were used. The thicknesses of all the targets were determined by weighing the foils and divided by their measured surface areas.

TABLE I. List of the target thicknesses used in the energy dispersive measurements

Targets thickness($\mu g/cm^2$)						
Al	Ti	Cu	Mo	Ag	Sm	Ta
849	1235	1639	1571	1493	4483/1344	2588/1226

3.2.2. Detectors

A scintillator is a material that emits light when it is excited by radiation or high energy atomic collisions. Common scintillators are thallium-doped NaI, some plastics, anthracene, and other organic solids. The light pulse emitted from the scintillator is converted to an electrical pulse by a photomultiplier tube, which consists of a

photocathode, the dynodes, and an anode. The structure of a photomultiplier is shown in Fig. 10. Incident photons strike the photocathode material and produce electrons. The electrons leave the photocathode, and are accelerated by an applied electric field. On striking the first dynode, more low energy electrons are emitted and these, in turn, are accelerated toward to the second dynode. Each dynode is held at a more positive voltage than the previous one. The geometry of the dynode chain is such that a cascade occurs with an ever-increasing number of electrons being produced at each stage. Finally the anode is reached where the accumulation of charge results in a sharp current pulse marking the arrival of a photon at the photocathode. Amplification can be as much as 10^8 meaning that measurable pulses can be obtained from single photons.

The particle detector used in the present energy-dispersive (absolute) measurements was made by attaching a thick block of BC-308 plastic scintillator to a 1 inch diameter Hamamatsu R1923 photomultiplier tube attached to a Hamamatsu E2923-01 tube base. The scintillator and photomultiplier tube were optically coupled and covered with aluminized Mylar to prevent background light from entering the system. A mu metal shield was placed around the photomultiplier tube and tube base to prevent interference in the light collection efficiency by stray magnetic fields.

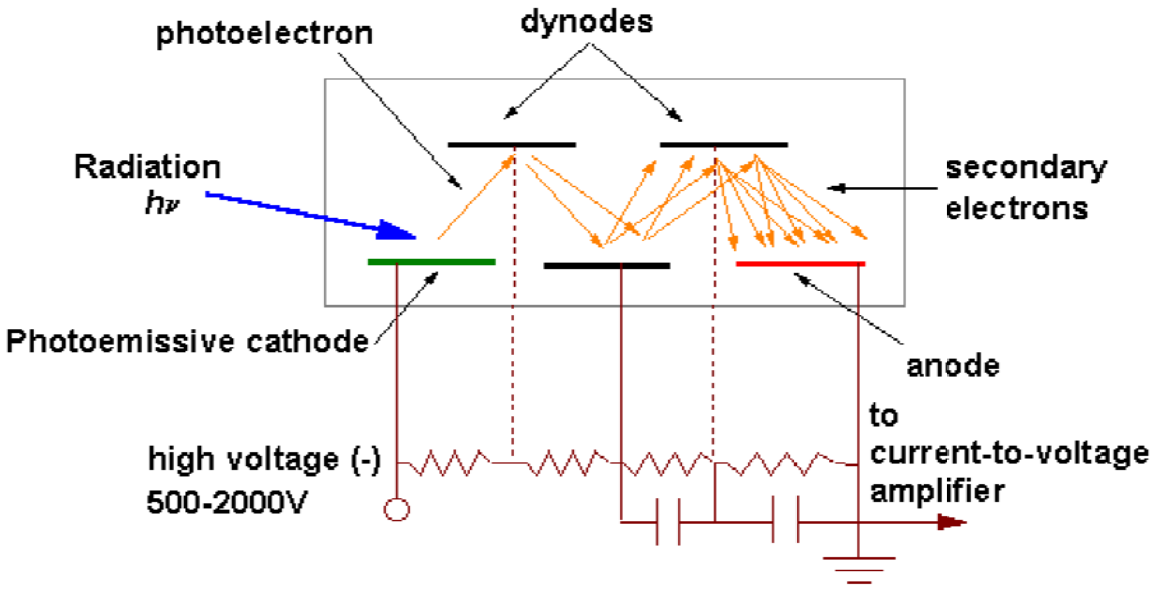

FIG. 10. Structure of the photomultiplier tube (taken from reference [111]).

The x-rays produced in ion-atom collisions were detected by a Si(Li) semiconductor detector. Li is incorporated into the semiconductor lattice by annealing the semiconductor at a high temperature (~500^{o}C) to increase the detector active volume. A cutaway view of a typical lithium-drifted silicon x-ray detector is shown in Fig. 11. A thin layer of gold (usually around 200 Å thick) is evaporated onto the surface of the p-type region (which faces the x-ray source), to act as an electrode. The lithium-drifted region (called the depletion region) is in the middle. A thin metal layer (usually around 2000 Å of Au) is evaporated onto the surface of the n-type region to act as another electrode. The depletion region of a silicon detector functions in a way that is analogous to argon in a gas-filled detector by producing ionization in the form of free holes and electrons. These free charges are swept away by the applied bias and collected by the electrodes. A voltage of approximately 1000 V is placed across the semiconductor material between the two electrodes, and the electron cascade produced by a photoelectron is detected as an electrical pulse at the anode. In addition to being more robust than scintillator detectors, semiconductor detectors also provide much higher resolution. The only disadvantage of the semiconductor detector is the need for cooling, usually with liquid nitrogen, to decrease the dark noise of the detector and first stage of the preamplifier. The Si(Li) detector used in the present work had a 6 mm active diameter and an depletion region that was approximately 5.5 mm thick.

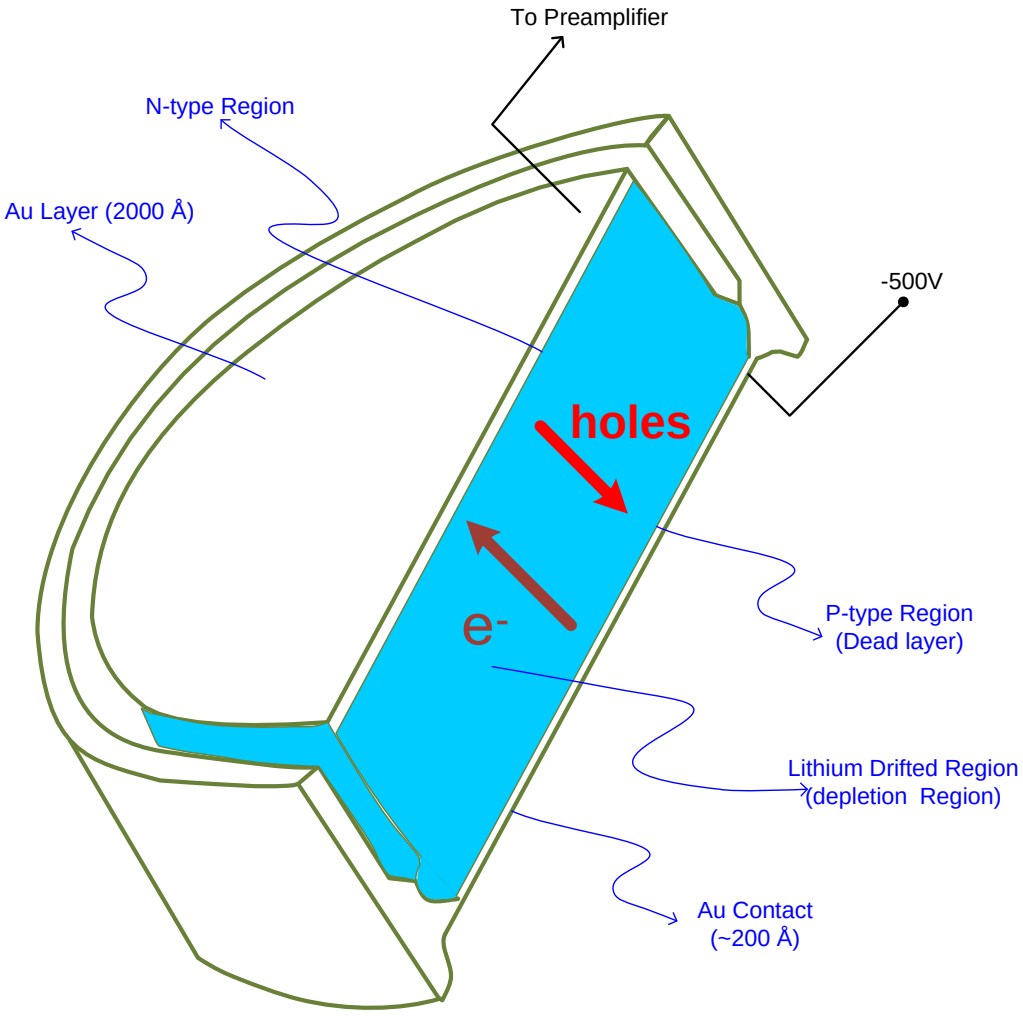

FIG. 11. Cross section of a typical lithium-drifted silicon detector. X-rays create electron-hole pairs in the depletion region of the semiconductor; these charge carriers then migrate to the electrodes under the influence of an applied bias voltage.

3.2.3. The measurements

The energy-dispersive measurements employed two different methods; one for low Z_2 targets and one for high Z_2 targets. The method applied to low Z_2 targets (Al, Ta, Cu, and Zr) involved absolute measurements utilizing a coincidence method, in which the absolute number of beam particles passing through the target was counted directly. The other method, applied to some of the Ag measurements and all of the Sm and Ta measurements, included determination of the x-ray yield from the target relative to the x-ray yield from a lower Z_2 reference foil positioned directly behind the target .

3.2.3.1. Absolute measurements

Although it would be possible to determine the absolute x-ray yields by simply counting the number of projectiles and x-rays independently, these measurements were conducted in coincidence to prevent the counting of events associated with particles which had undergone slit edge scattering, to reduce significantly the background in the resulting x-ray spectra, and to eliminate the need to determine the efficiency of the particle detector. The coincidence rate, $R_c^{'}$, is given by

$$R_c^{'} = R_c\, p_p\, p_x, \tag{22}$$

where R_C is the rate of coincident events, p_p is the particle detection probability and p_x is the x-ray detection probability. The detected particle rate, $R_p^{'}$, is given by

$$R_p^{'} = R_p\, p_p, \tag{23}$$

where R_p is the incident particle rate.

When less than one x-ray is emitted per particle, the rate of coincident events is equal to the rate of x-ray emission, R_x. The x-ray detection probability is equal to the product of the solid angle fraction intercepted by the detector and the efficiency for x-ray detection, $(\Omega\varepsilon)_x$. Therefore,

$$R_c^{'} = R_x p_p (\Omega\varepsilon)_x , \tag{24}$$

and

$$\frac{R_c^{'}}{R_p^{'}} = \frac{R_x p_p (\Omega\varepsilon)_x}{p_p R_p} = N_x (\Omega\varepsilon)_x , \tag{25}$$

where N_x is the number of x rays per particle. When more than one x-ray is emitted per particle, the rate of coincident events is equal to the particle rate. The x-ray detection probability is equal to the product of the number of x-rays emitted per particle, the solid angle fraction, and the x-ray detection efficiency. Therefore,

$$R_c^{'} = R_p (\Omega\varepsilon)_p N_x (\Omega\varepsilon)_x \tag{26}$$

and

$$\frac{R_c^{'}}{R_p^{'}} = N_x (\Omega\varepsilon)_x \tag{27}$$

The x-ray coincidence rate was usually within 3% of the x-ray singles rate, indicating that the particle detection efficiency was close to 100%.

Signals from the particle detector were well defined (3 mV) with -750 volts applied to the photomultiplier tube. However, it was observed that the signals deteriorated, becoming less well defined with decreased amplitudes, over time and when the particle rate became too high. This problem was especially prevalent at high particle rates (e.g., greater than 20,000 particles per second for Ar ions and greater than 2,000 particles per

second for Xe ions). In order to prevent these effects, the particle rates were kept below the thresholds for saturation and the scintillator was rotated occasionally to expose a fresh region to the beam, thereby restoring the signals to their original amplitudes.

A diagram of the data acquisition electronics is shown in Fig. 12. Signals from the photomultiplier were preamplified then sent through a LeCroy 428F Linear FAN IN/OUT unit into a Tennelec TC 455 Quad CFD (Constant fraction discriminator), where the arrival times of the different events were marked precisely in order to achieve maximum time resolution, and into an Oscilloscope along with one of the output signals of the CFD for monitoring purposes. A second output of the CFD was used to count the prompt particle signals while a third output was directed to LeCroy 222 Dual Gate & Delay Generator. The gate & delay generator was used to delay the particle timing signal so that it would arrive at the Ortec 357 TAC (time to amplitude converter) after the x-ray timing signal, thereby acting as the TAC stop signal.

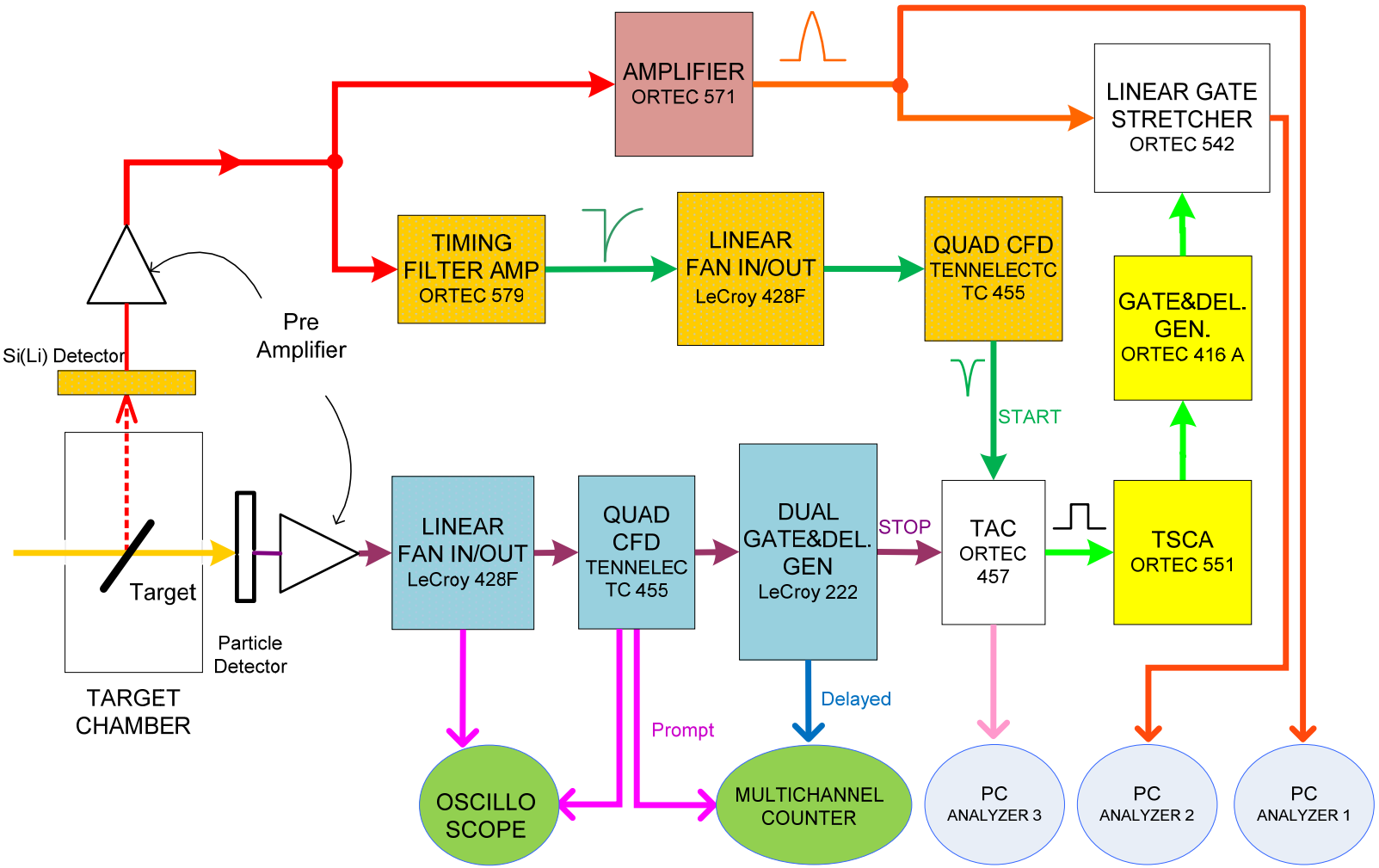

FIG. 12. A schematic diagram of the electronic system for the coincidence measurements.

The x-rays emitted from the target were measured with an Ortec SLP-06165-P Si(Li) detector. The preamplified signals from the Si(Li) detector were amplified by an Ortec 579 Timing Filter Amplifier and then distributed through a LeCroy 428F Fan In/Out to an oscilloscope for monitoring purposes, and to a Tennelec TC 455 Quad CFD unit where the threshold was adjusted to eliminate noise signals. The CFD (x-ray) output provided the start signal for the TAC, which generated an output signal corresponding to the time difference between the two input signals (x-ray and particle) up to a limit of 300 nanoseconds. The TAC output signal was directed to an Ortec 551 TSCA (Timing single channel analyzer). The TSCA output signal was directed to an Ortec 416 Gate & Delay Generator, whose output signal was directed to an Ortec 542 Linear Gate Stretcher to open the gate for the coincident events. The output signal of the TAC was also sent to a pulse height analyzer (PCA-3) for monitoring purposes during the run.

The preamplified signals from the Si(Li) detector were also directed to an Ortec 571 amplifier. The amplified signals were gated by the Ortec 542 Linear Gate & Stretcher for the coincident events. Then the coincidence signals were processed by a multichannel pulse height analyzer operating within a personal computer (PCA-2).

Another output of the Ortec 571 amplifier (for the x-ray signals) was directed to a multichannel pulse height analyzer operating within another personal computer (PCA-3).

3.2.3.2. Relative measurements

Absolute K x-ray yields could not be measured for the Sm and Ta targets by direct particle counting because their K x-ray production cross sections were too low to

provide sufficient x-ray counting statistics at useable particle rates. This same problem was also encountered for the Ag targets at 2.5 and 4.0 MeV/amu. In the case of Ag, a reference foil of Cu was mounted behind the target in the same holder and the absolute yield of Cu K x-rays was determined by direct particle counting as described above. Then the particle detector was removed so that the particle rate could be increased and a thin (12. 6 mg/cm^2) Al absorber placed in front of the Si(Li) detector to absorb low energy (L) x-rays. Finally, an x-ray spectrum containing both the target and the reference K x-rays was recorded at an increased particle rate sufficient to provide adequate target K x-ray counting statistics. In the case of Sm and Ta, reference foils of Ag and a three step procedure were employed. In the first step, the absolute yield of target Lα x rays was determined by direct particle counting. In the next step, the particle detector was removed, the thin Al absorber placed in front of the Si(Li) detector to absorb target M x rays, and the spectrum of target L x rays plus reference K x rays was record at a particle rate sufficient to provide adequate Ag K x ray counting statistics. Finally, in the last step, the thin Al absorber was replaced with a thick (355 mg/cm^2) Al absorber to reduce the target L x ray intensity, and the spectrum of target K x rays plus reference foil K x rays was recorded at a particle rate sufficient to provide adequate target K x ray counting statistics.

3.2.4. Si(Li) detector calibration

As may be seen by referring to Fig. 11, x-rays entering a typical Si(Li) detector must pass through a thin Au layer, which provides an electrical contact and a thin “dead” layer

caused by incomplete Li compensation. In addition, the vacuum cryostat containing the Si(Li) detector has Be window, which in the present case is nominally 0.0254 mm thick.

The efficiency of a Si(Li) detector depends principally on the thickness of these layers and the silicon depletion region. Except for the thickness of the Be window, the exact thickness of the layers and the depletion region were not known. Therefore, the efficiency could not be calculated directly, and had to be determined experimentally.

Each particular semiconductor detector is unique in its detailed efficiency response for photon energies due to variations in fabrication. Numerous methods have been developed for the calibration of Si(Li) detectors. For example, the use of calibrated radioactive sources [112-114], synchrotron radiation from an electron storage ring [114-117], bremsstrahlung by electron impact [118-121], and particle induced x-ray emission [118, 119, 121-123]. Among these methods, the most common one for photon energies above 6 keV is the use of calibrated radioactive sources. This method determines the detector efficiency by measuring the number of photons detected at specific energies and comparing them with the calibrated total emission rates.

The efficiency calibration becomes difficult at photon energy below 6 keV because of the scarcity of suitable radioactive sources that emit single, resolvable x-rays and the existence of discontinuities in the efficiency curve due to the K- and M-absorption edges of Si and Au, respectively. Detail discussions of these problems have been given by Campbell et al. [112].

Lennard and Phillips [118] described a method that was based on the detection of particle-induced x-rays from thin calibration targets, whose thicknesses are measured

simultaneously by the Rutherford backscattering (RBS) method. The accuracy of this method is primarily limited by the accuracy of the adopted x-ray production cross sections. This approach was further investigated by Maenhaut et al. [124], Cohen [125], Cipolla et al. [126], and de Castro Faria et al. [127].

A combination of two different methods was employed for the calibration of $\Omega\varepsilon$ in the current work, where Ω and ε represent the detector solid angle fraction and efficiency, respectively. In the first method, $\Omega\varepsilon$ values at 1.49, 1.74, 2.62, 3.31, 4.51, and 8.04 keV were determined by measuring K x-ray yields of Al, Si, Cl, K, Ti, and Cu excited by 10 MeV protons and comparing them with the yields predicted by theoretical ECPSSR K-shell ionization cross sections. In the second method, the $\Omega\varepsilon$ values were measured using the 11.9, 13.9 ,17.8, 20.8, 26.4, 30.6, 35.2, 53.2, 59.5, 79.6, 81.0, 122.1, and 136.5 keV x-rays and γ-rays from calibrated ^{241}Am, ^{133}Ba, , and ^{57}Co sources, placed at the target position. The acquisition time was measured using a standard 60 Hz pulser. The numbers of each of the different x-rays and γ-rays emitted by these sources per nuclear disintegration are well established [113, 128, 129]. They are listed in Table II for the sources used in the present calibration.

Typical calibration spectra of ^{57}Co, ^{133}Ba, and ^{241}Am taken with the Si(Li) detector are shown in Fig. 13, Fig. 14, and Fig. 15. The full widths at half maximum (FWHM) for the peaks at 13.93, 26.35, and 59.53 keV were 287, 313, and 325 eV, respectively.

TABLE II. Energies and intensities of the standard radioactive sources [130].

Sources	Energy (keV)	Line	photons per disintegration
^{241}Am	11.89	Np Ll	0.00848 +/- 0.00010
	13.90	Np Lα	0.1303 +/- 0.0010
	17.81	Np Lβ+η	0.1886 +/- 0.0015
	20.82	Np Lγ	0.0481 +/- 0.0004
	26.34	γ1	0.0240 +/- 0.0003
	59.54	γ2	0.3578 +/- 0.0009
^{133}Ba	30.62	^{133}Cs Kα	0.340 +/- 0.004
	30.97	^{133}Cs Kβ	0.628 +/- 0.007
	53.16	γ1	0.0214 +/- 0.0003
	79.61	γ2	0.0265 +/- 0.0005
	81.00	γ3	0.329 +/- 0.003
^{57}Co	6.40	Fe Kα+Kβ	0.500 +/- 0.008
	122.06	γ	0.8551 +/- 0.0006
	136.47	γ	0.1071 +/- 0.0015

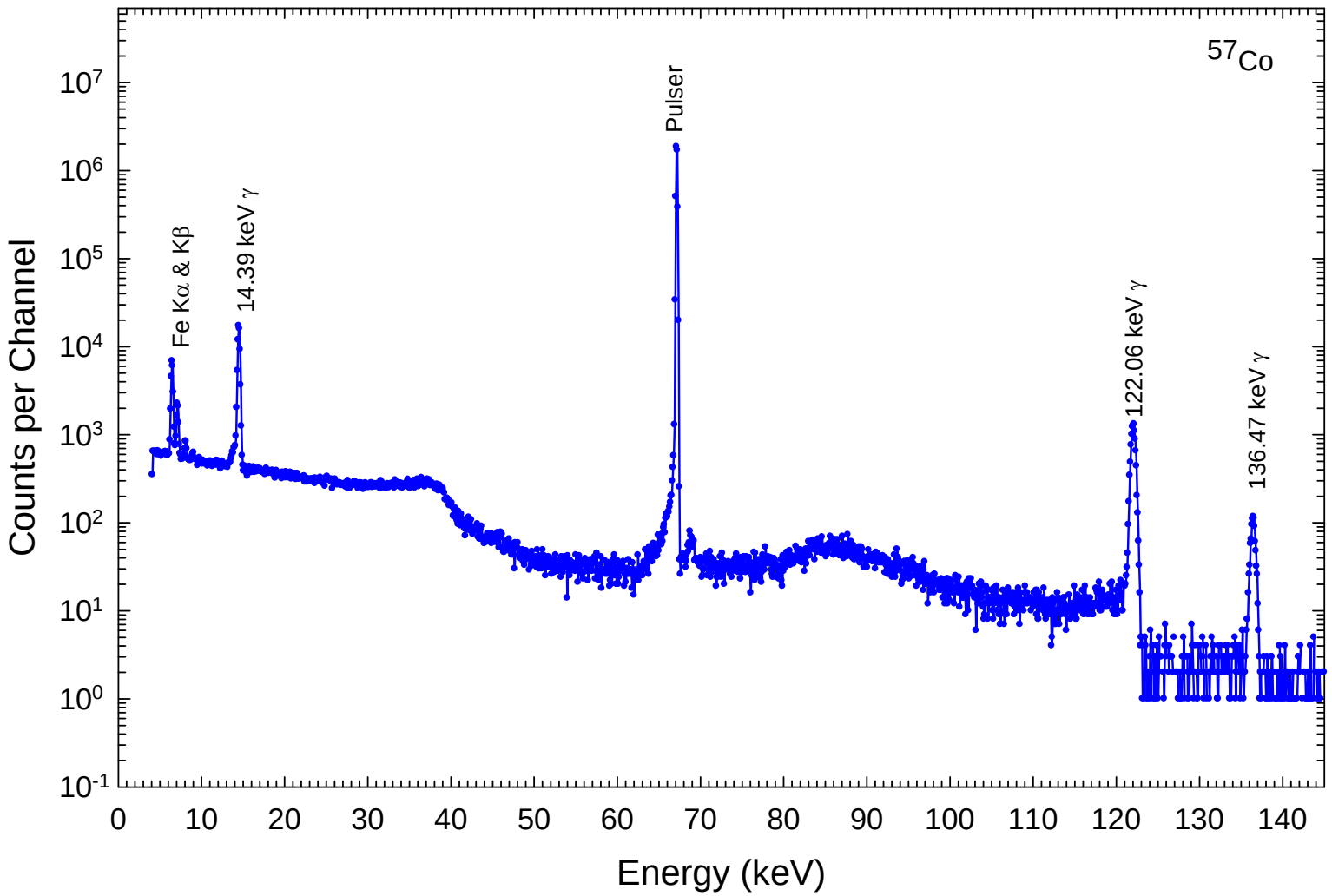

FIG. 13. A typical ^{57}Co calibration spectrum.

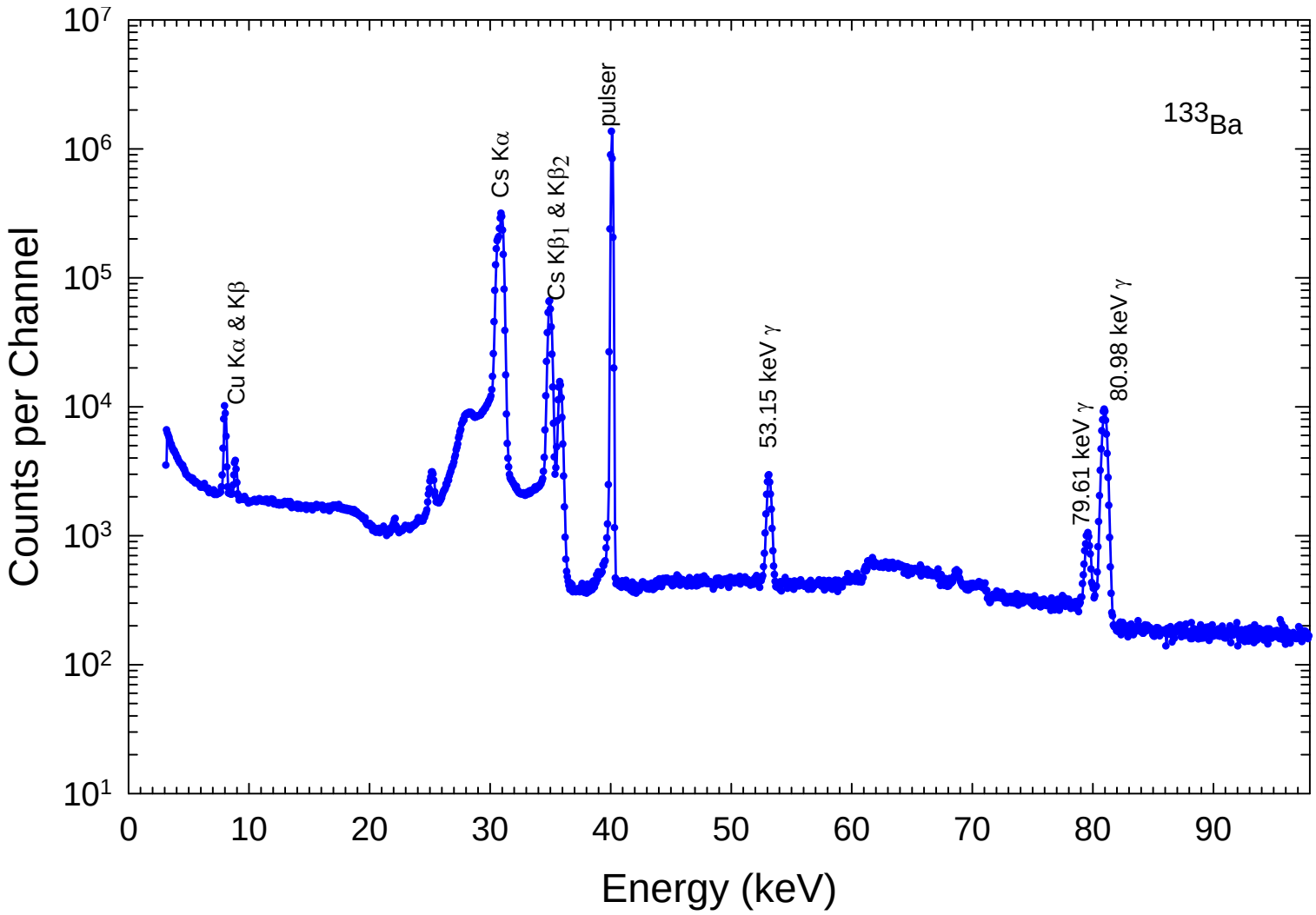

FIG. 14. A typical ^{133}Ba calibration spectrum.

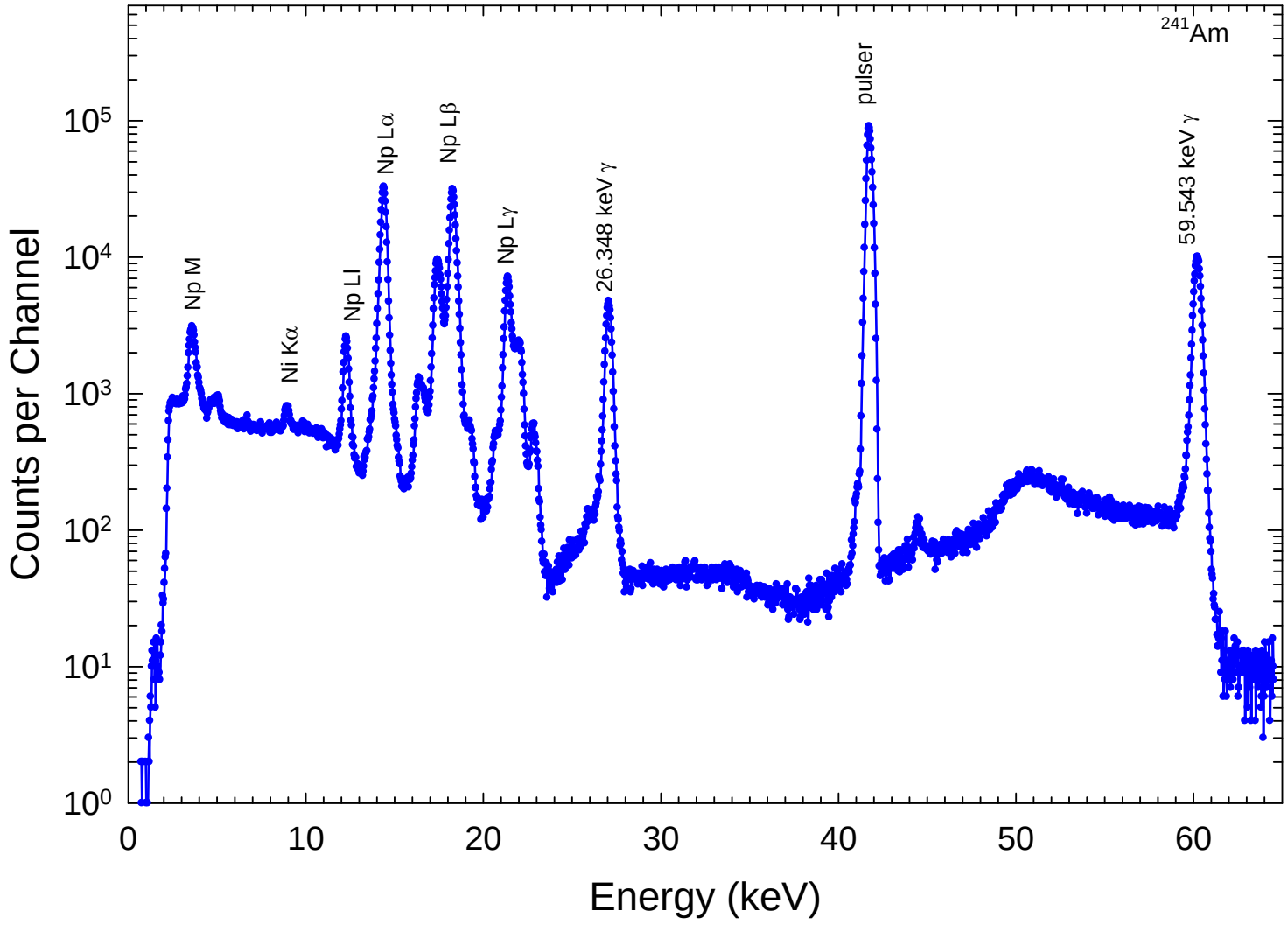

FIG. 15. A typical ^{241}Am calibration spectrum.

The probability of detecting a photon emitted by an isotropic source is given by the quantity Ωε, where Ω is the fraction of the solid angle intercepted by the detector and ε is the detector efficiency. In the present case of a Si(Li) detector, the incident x-rays are attenuated as they pass through the Be window, Au contact layer, and Si dead layer. Including these attenuation factors in the definition of ε, the total detection probability may be expressed as

$$\Omega\varepsilon = \frac{\omega}{4\pi}\left[e^{-a_1}(1-e^{-a_2})\right], \tag{28}$$

where $\frac{\omega}{4\pi}$ is the solid angle fraction, the first exponential factor accounts for attenuation of the incident x-rays in the various layers, and the factor in parentheses is the x-ray photoabsorption probability in the depletion region. The quantity a_1 is given by

$$a_1 = \sum_i \mu_i t_i \,, \tag{29}$$

where μ_i is the total mass absorption coefficient (expressed in cm^2/g) and t_i is the layer thickness (expressed in g/cm^2). The sum includes the three attenuation layers mentioned above. The quantity a_2 is

$$a_2 = \mu_{Si} t_{Si} \,. \tag{30}$$

where the μ_{Si} is the mass absorption coefficient for photoelectric absorption in Si and t_{Si} is the thickness of the Si depletion region.

The unknown thicknesses of the Au layer, Si dead layer, depletion region, and the solid angle fraction were determined by fitting Eq. (28) to the experimental calibration points using the method of least squares. Initially, the thickness of the Be window was set to 0.0254 mm as given by the manufacture but this value resulted in large deviations

from the experimental data. Therefore, it was treated as one of the fitting parameters.

The fitted values of the thickness of the Au layer, the Be window, the Si dead layer, and the Si depletion region, as well as the value of the solid angle fraction are listed in Table III. Fig. 16 shows the measured efficiencies and the calculated efficiency curve based on Eq. (28) with the fitted parameters.

The efficiency was routinely checked before each beam run, and was found to remain constant. Efficiency values needed in the data analysis were calculated with the model function and are believed to have an uncertainty of no more than $\pm 3\%$ over the energy region from 8 to 60 keV. The efficiency uncertainty in the energy region from 1.5 to 8 keV is estimated to be $\pm 10\%$.

The energy calibration of the Si(Li) detector was performed using an ^{241}Am source. A Ni foil and a mixture of La_2O_3 and Sm_2O_3 powder were placed behind the source in order to produce the corresponding K x-rays by x-ray fluorescence. The Ni, La, and Sm $K\alpha$ and $K\beta$ peaks were used to fill the large energy gaps between the ^{241}Am calibration points. A typical energy calibration spectrum obtained with the ^{241}Am source is shown in Fig. 17. Energy calibration of the Si(Li) detector was performed at the beginning, during and at the end of each run to check the stability of the electronic system.

TABLE III. The fitted thicknesses of different layers of the Si(Li) detector in g/cm^2 and the solid angle fraction.

Au	Be	Dead Si	Active Si	Ω
0.0000200	0.00280	0.0000100	1.137	1.75×10^{-3}

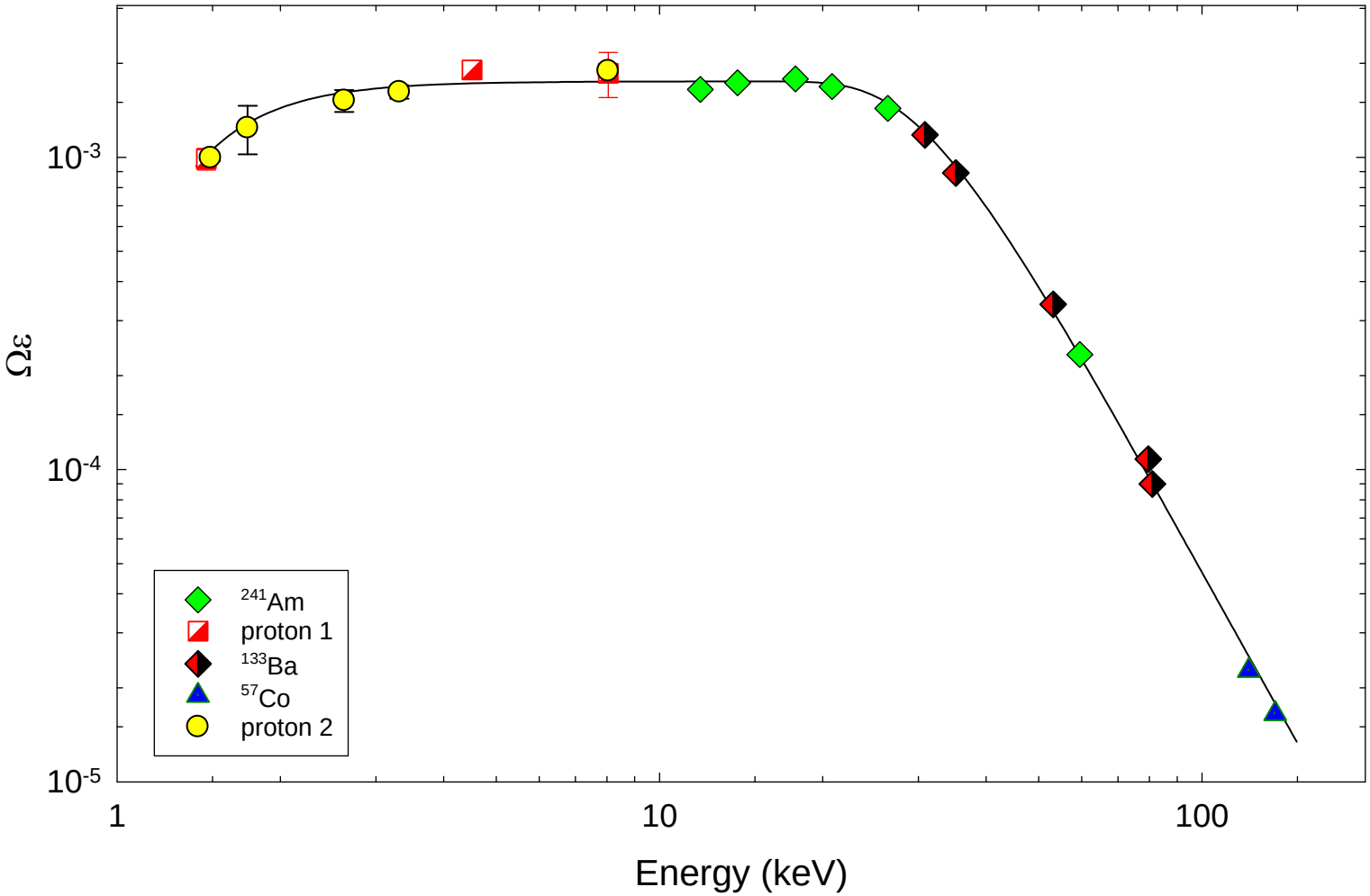

FIG. 16. Energy dispersive Si(Li) spectrometer detection probability as function of photon energy. Data from three separate calibrations employing radioactive sources and two separate calibrations using proton bombardment are shown.

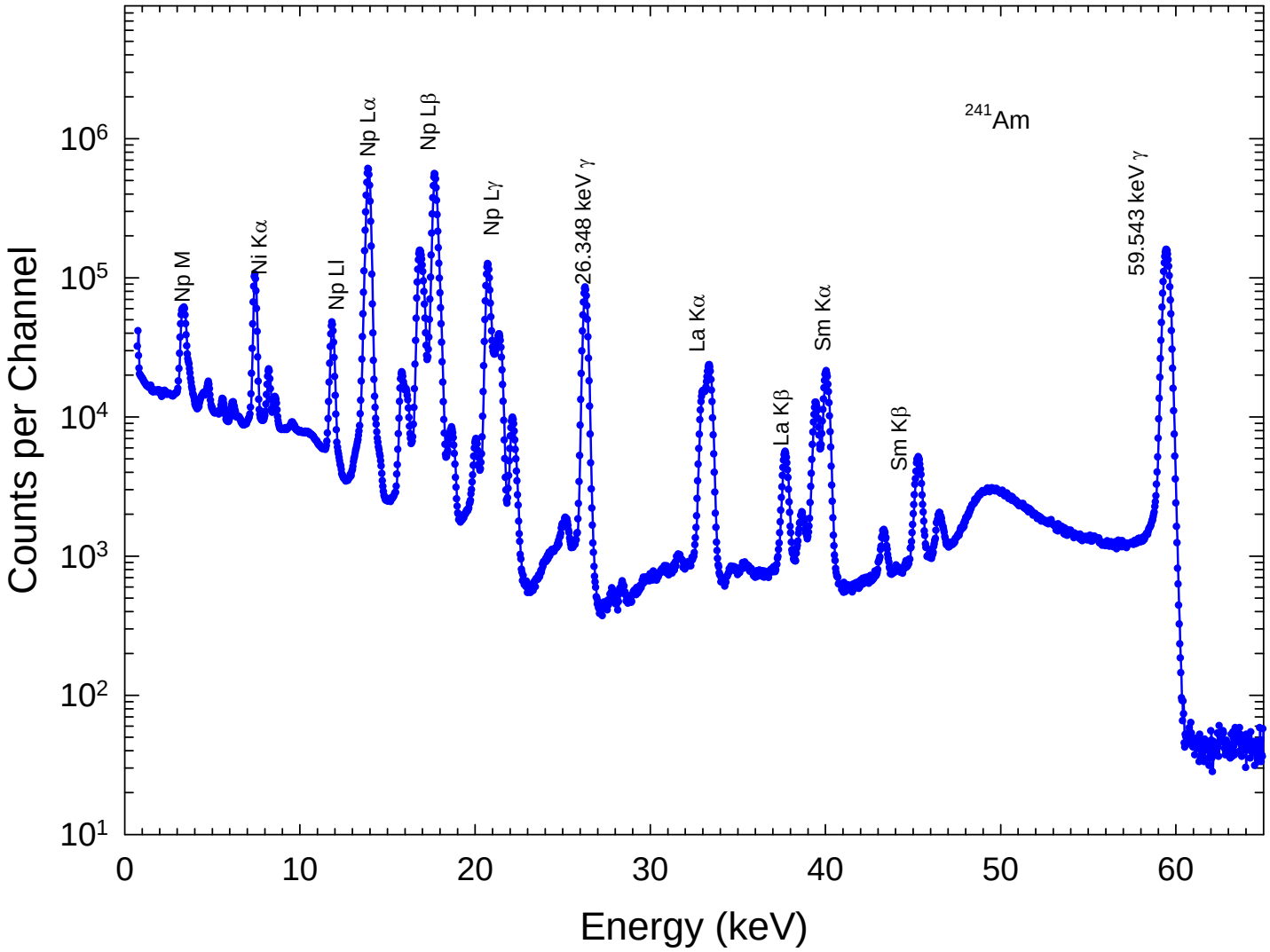

FIG. 17. A typical energy calibration spectrum obtained with ^{241}Am source.

3.3. Wavelength-dispersive measurements

A Johansson-type curved crystal spectrometer was employed to record high resolution K x-ray spectra for the purpose of investigating the effects of multiple ionization and excitation by secondary processes. Experimental details concerning the high resolution measurements are described in the following sections.

3.3.1 Bragg reflection

A two-dimensional depiction of Bragg reflection is shown in Fig. 18. X-rays with incident angle θ, defined as the angle between the incident x-rays and the crystal planes, are reflected by the crystal lattice. As the crystal in a spectrometer is rotated, θ changes, causing the projection of the spacing between the crystal planes along the direction of the beam to also change. Along the incident vector, the difference in the x-ray path length between two adjacent planes is $d\sin\theta$, where d is the distance between the crystal planes. When the diffracting crystal is oriented in such a way that twice this difference ($2d\sin\theta$) equals an integer (n) multiple of the x-ray wavelength, λ, a reflected x-ray experiences constructive interference with reflected x-rays (same wavelength) from adjacent planes. When integer n equals one, two, three, etc., the corresponding constructive reflective is named a first order, second order, third order, etc. reflection. High order reflections are much weaker than the first order reflection, hence the detection probability is much lower than that for the first order reflection. The relation between θ and the wavelength, λ, is given by the well known Bragg equation

$$n\lambda = 2d\sin\theta, \tag{31}$$

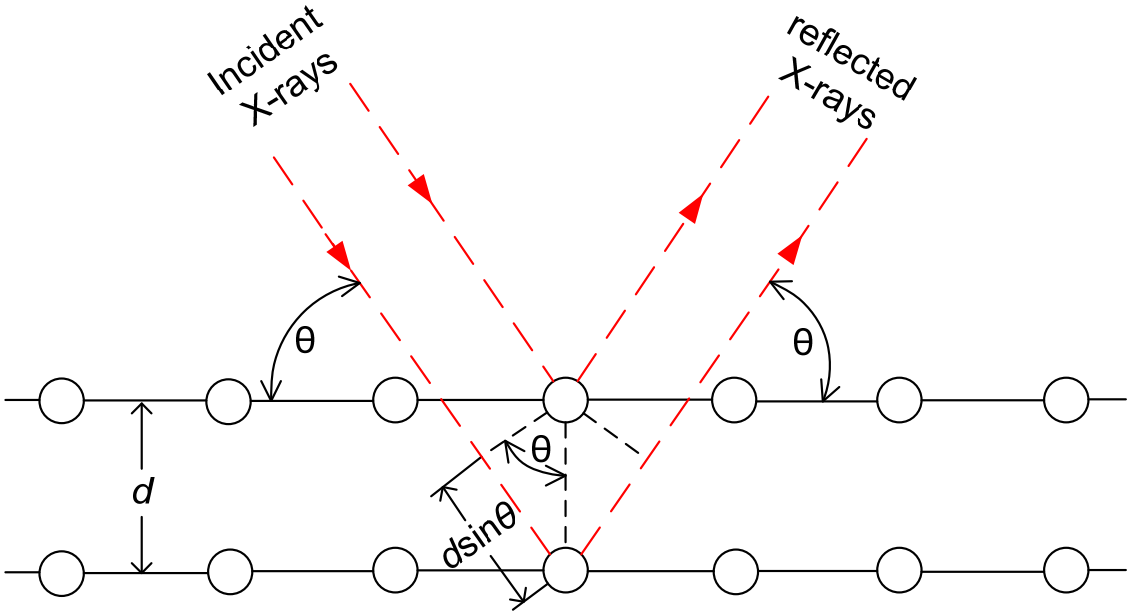

FIG. 18. Schematic diagram for determining Bragg's law.

where n represents the order of reflection (n = 1, 2, 3,…). Differentiation of Bragg's equation leads to an expression for the rate of change of the wavelength with respect to the Bragg angle

$$\frac{d\lambda}{\lambda} = \cot\theta d\theta, \tag{32}$$

which shows that the higher the diffraction angle, the better the resolution. The

resolution is also related to the lattice spacing d, and the perfection of the crystal lattice over its entire diffraction surface.

From the Bragg equation [Eq. (31)], the maximum wavelength that can be diffracted in first order is $\lambda_{max} = 2d$ since $\sin\theta$ can not exceed unity. Because such spectrometers operate by precisely orienting the crystal with respect to the incident x-ray beam, the mechanical tolerances are of critical importance. Due to the enhanced resolution for larger angles (θ) as well as mechanical considerations, each Bragg spectrometer has an optimal range of angles for which it is suited.

Due to the limitations on the accessible wavelength range of the current spectrometer, only x-rays from atoms up to Z = 32 can be measured in first or second order. The angular dispersion from Eq. (32) is given by

$$\frac{d\theta}{d\lambda} = \frac{1}{\lambda}\tan(\theta). \tag{33}$$

Table IV lists some of the common crystals used in the crystal spectrometer along with their characteristics.

TABLE IV. Characteristics of commonly used crystals for the curved crystal spectrometer [131-133].

Crystal	Double lattice spacing, 2d(Å)	Wavelength range(Å)
LiF [Lithium Fluoride(200)]	3.027	0.7 to 3.8
NaCl [Sodium Chloride (002)]	5.642	0.9 to 5.3
PET [Pentaerythritol(002)]	8.74	1.4 to 8.3
ADP[Ammonium dihydrogen phosphate (101)]	10.64	1.8 to 10.3

3.3.2 Detector

A gas flow proportional counter was employed as the detector in the high resolution measurements of the current project. The gas flow proportional counter consisted of a metal cylinder with a volume of 1.5 cm^3 and flowing P-10 gas (10% methane, 90% Ar) operated at atmospheric pressure. A Mylar window having dimensions of $5\ mm \times 20\ mm$ and a thickness of 530 $\mu g/cm^2$ separated the gas from the vacuum of the target chamber and transmitted the diffracted photons. A 0.127 mm diameter tungsten center wire served as the anode. Photons passing through the Mylar window photoionize gas atoms creating free electrons, which are then accelerated by the applied high voltage (1750 V) between the metal cylinder and the anode. The resulting electron cascade is collected by the anode and detected as an electrical pulse.

3.3.3 Targets

Solid targets used in the measurements with the curved crystal spectrometer were in the form of either metallic foils or pressed pellets. The Al, Ti, and Cu targets were the same as those used for the energy-dispersive measurements. The pellets were prepared by placing a small amount of a powdered compound, containing the element to be investigated, into a pellet mold. A hydraulic press was then used to press the powder into the form of a pellet. Before forming it into a pellet, a small amount of graphite powder was mixed with the target material to help bind target material and to make the target conductive to prevent electric charge build-up during the bombardment by the projectile ions. The target holder (Fig. 19) was designed to hold the targets at 45 degrees

with respect to both the beam and the spectrometer, and to allow reproducible target positioning. The drawback of this design is that it can hold only one target at a time and so the target chamber must be vented for each target change. The target was positioned to allow the spectrometer to view its front surface. A cover contained a 3-mm diameter collimator to limit the size of the beam.

3.3.4 The curved crystal spectrometer

The crystal spectrometer employed for the current work was a Johansson curved crystal spectrometer, manufactured by Applied Research Laboratory (ARL) of Sunland, CA. Such a spectrometer is frequently referred to as a focusing crystal spectrometer because of its capability of diffracting x-rays in such a way that they converge at the detector position. Though this focusing action complicates the spectrometer design, it improves the detection efficiency and resolution.

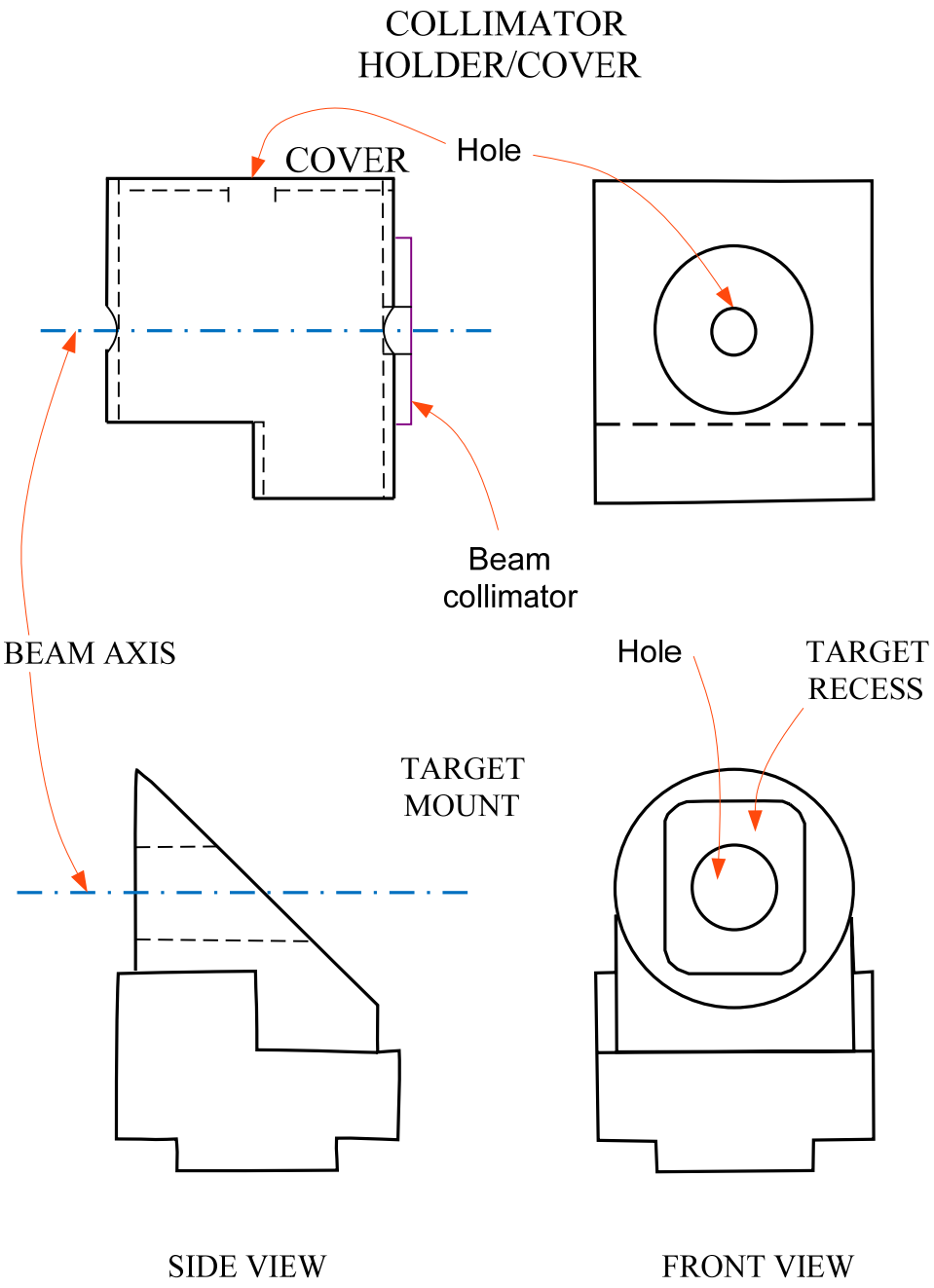

FIG. 19. A schematic drawing of the solid target mount used in the wavelength-dispersive measurements.

Fig. 20 shows a cross sectional schematic of the spectrometer-target chamber assembly with the relevant features indicated. The coupling assembly was fabricated out of welded aluminum plate and the finished surfaces were machined to ensure that the spectrometer/coupling assembly O-ring surfaces were vacuum tight. The target chamber was machined from a cylindrical aluminum tube.

The curved crystal allows a divergent beam of x-rays to be used, while maintaining the Bragg criteria. This is illustrated in 21, where x-rays emitted in slightly different directions are shown being reflected into the detector at the same wavelengths. If the crystal shown in Fig. 21 was flat, only the central x-rays would reach the crystal at the appropriate Bragg angle.

The Bragg angles available with this spectrometer range from 13.3 to 71.8 degrees. Using a LiF (200) crystal (d = 2.013 Å), this range of angles allows x-rays varying from about 3.2 to 12 keV to be observed in first order.

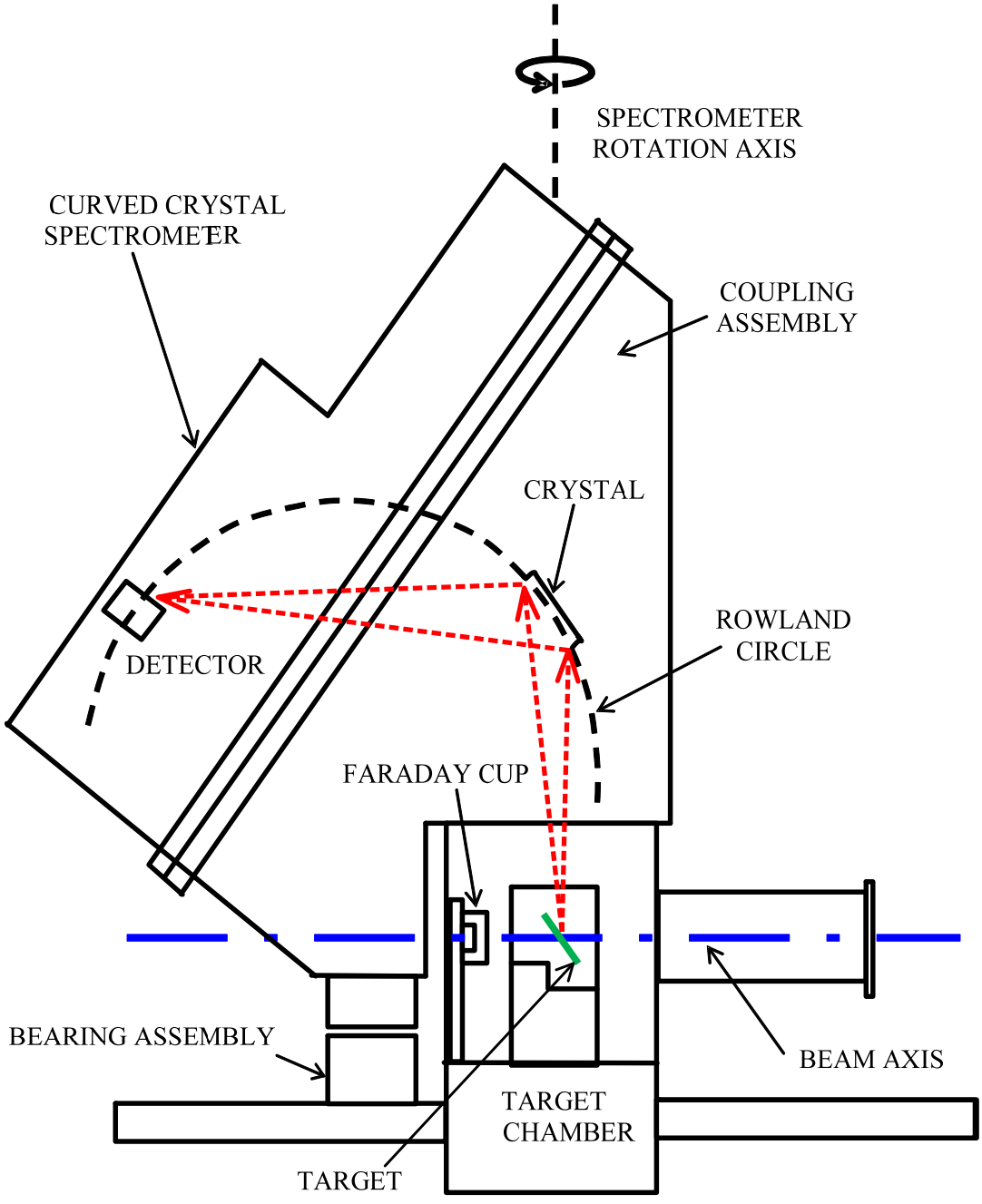

FIG. 20. Schematic drawing of the spectrometer and target chamber assembly.

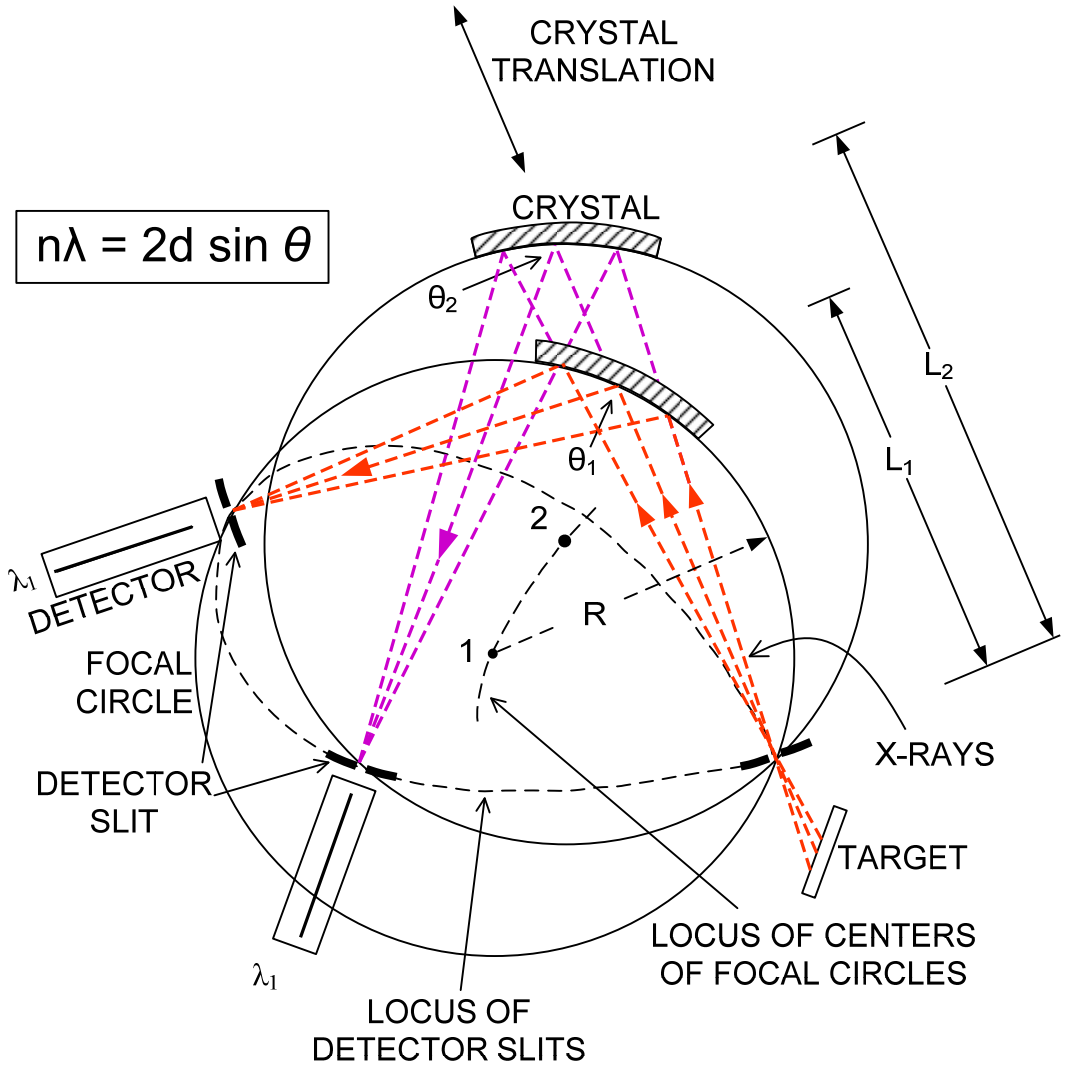

FIG. 21. Reflection geometry of the curved crystal x-ray spectrometer at two wavelength settings: $\lambda_1 < \lambda_2$ [134].

The Johansson geometry (see Fig. 21) requires that a crystal be bent to radius 2R and ground to a radius of R, where R is the radius of the focal circle. The focal circle diameter and radius of curvature of the crystal planes were fixed at 25.4 cm, and the crystal surface had a 12.7 cm radius of curvature. The target-to-crystal and crystal-to-detector, distances always remain equal to L, which is given by

$$L = \frac{n\lambda R}{2d} = R\sin\theta . \tag{34}$$

As indicated in Fig. 21, the crystal follows a straight line path moving either toward or away from the target, while rotating slightly to maintain the proper Bragg angle. Movement of the proportional counter is shown in Fig. 21 by the dashed line. The motion of all of the moving parts of the spectrometer is mechanically coordinated and a single stepping motor propels the spectrometer from one wavelength position to the next. In addition to this stepping motor, the curved crystal spectrometer has two DC motors used to remotely adjust the crystal plane orientation and the focal circle position.

The width of a peak in an x-ray spectrum recorded with a crystal spectrometer depends on the natural line width of the x-ray transition, the divergence of the crystal spectrometer at the wavelength of interest, and intrinsic properties of the crystal. The divergence of a curved crystal spectrometer is dependent on the degree of perfection of the crystal lattice, the size of the x-ray source, the degree of accuracy achieved in the curving and grinding processes, the mechanical tolerances in the complicated motion of the crystal and proportional counter, and the diffraction of x-rays that have penetrated the crystal to planes that are beyond the focal circle. The combination of these factors makes it nearly impossible to accurately calculate the divergence. Though calculation of

the absolute spectrometer response is not feasible, calculation of its general form is rather straight forward. The photon energy, E, is related to its wavelength, λ, by

$$E = hc / \lambda , \tag{35}$$

where h is Planck's constant and c is the speed of light. Taking the derivative of Eq. (35) yields

$$\frac{dE}{d\lambda} = -\frac{hc}{\lambda^2} . \tag{36}$$

Therefore,

$$\Delta E \approx -\frac{hc}{\lambda^2}\Delta\lambda , \tag{37}$$

where the uncertainty in the measured photon energy, ΔE, is given in terms of the spectrometer's uncertainty in wavelength determination, $\Delta\lambda$. Alternatively, from Eq. (32) and Eq. (37) one can obtain

$$\Delta E = -\frac{hc}{\lambda}\cot\theta\Delta\theta , \tag{38}$$

which shows that the spectrometer's contribution to the line width, ΔE, is given in terms of the spectrometer's uncertainty in the Bragg angle, θ.

3.3.5 Data acquisition procedure

Before data collection, the beam alignment was checked by reading the beam current on a Faraday cup located directly behind the target holder, while steering the beam horizontally and vertically. When the optimum beam current reading on the Faraday cup was attained, the beam alignment was considered complete. Then the x-ray intensity was maximized by remotely adjusting the crystal orientation and the focal circle angle, respectively. A schematic of the data acquisition system is shown in Fig. 22. Pulses

from the proportional counter were amplified and shaped using a 2 μs shaping constant linear amplifier and then sent to an Ortec 420 A timing single channel analyzer (TSCA), which had the upper and lower level discriminators set to define the x-rays of interest. The TSCA output was sent to the spectrometer control unit. The beam current collected in the Faraday cup was digitized by a integrated digitizer (model 1000C) manufactured by Brookheaven BIC Instruments Co. and sent to the spectrometer control unit for the purpose of normalization. When pellet targets were used, the current was integrated directly from the target because the pellets were thick enough to stop projectiles ions. Once a preset amount of charge was collected, the control unit automatically stepped the spectrometer to the next position and a signal was sent to the computer, operating in a multichannel scaling mode, to advance to the next channel in the spectrum.

The data were stored on a personal computer via a data collection card (manufactured by Oxford Co. Ltd) using software named PCAII.

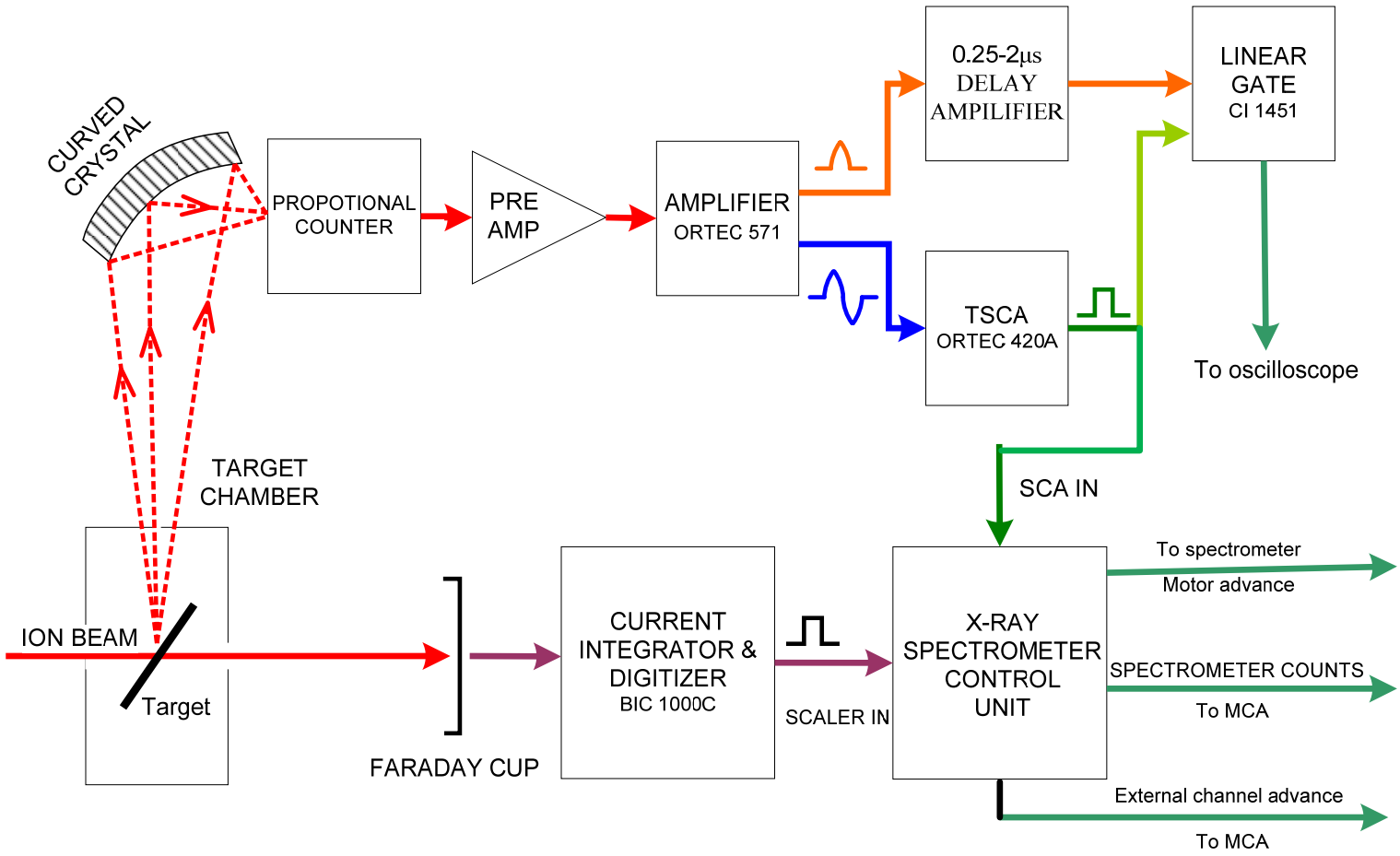

FIG. 22. Electronic setup for high resolution measurements.

CHAPTER IV

X-RAY PRODUCTION IN HEAVY ION COLLISIONS

This chapter focuses on the characteristics of K x rays emitted from multiply ionized atoms. A general description of inner-shell vacancy creation and its decay by x-ray and Auger transitions are presented. Fluorescence yields for K x-ray decay also are discussed.

4.1. Ionization

The cross section for the removal of an inner-shell electron from an atom in a collision with an ion depends predominantly on the projectile atomic number Z_1, the projectile speed v_1, and the target inner-shell electron speed v_2. Projectiles such as photons, electrons, and protons predominantly produce only single inner-shell vacancies. When heavy ions ($Z_1 > 2$) are employed, there is a significant probability that an inner-shell ionization will be accompanied by the removal of additional electrons, leaving the target atom in a multiply ionized state. Because the absence of the electrons reduces the screening of the nuclear charge felt by the remaining electrons, the binding energies of those electrons increase.

Inner-shell vacancies can be produced through various mechanisms, depending on the values of the collision parameters that characterize the process. Direct Coulomb

excitation (DE) or ionization (DI) is the dominant process for low-Z_1 projectiles and high-Z_2 target atoms. When Z_1 becomes comparable to the target atomic number (Z_2), and when the projectile speed v_1 is lower than the orbital speed of the electron to be removed, the electron's quantum state adjusts adiabatically as the projectile approaches the target nucleus and forms molecular orbitals from which electrons are excited, and the resulting vacancies correlate to the projectile or target K shells or are shared between the two K shells according to the relative asymmetry between the two collision partners. This is known as the molecular orbital mechanism. An inner-shell vacancy can also be produced via electron capture from the inner shell of a target atom to an available bound level of the projectile. This process peaks when the speed of the electron in the initial state is comparable to its speed in the final state.

4.2. De-excitation

An inner-shell vacancy is most likely to be filled by an electron from a higher shell or subshell, resulting in the emission of an x ray or an Auger electron. The difference between the total energy of the atom in the initial and the final state (transition energy) determines the energy of the emitted x-ray, or electron. The two processes are competing, but they are not equally probable. The probability that an inner vacancy will be filled in an x-ray transition is known as the fluorescence yield. The two vacancy decay processes are shown schematically in Fig. 23. Auger decay is a special case of a non-radiative decay in which the emitted electron is ejected from a higher shell relative to the electron that fills the inner vacancy. Non-radiative transitions are predominant

when the transition energy is low, while x-ray emission is more important when the transition energy is high (this will be discussed in detail in section 4.4).

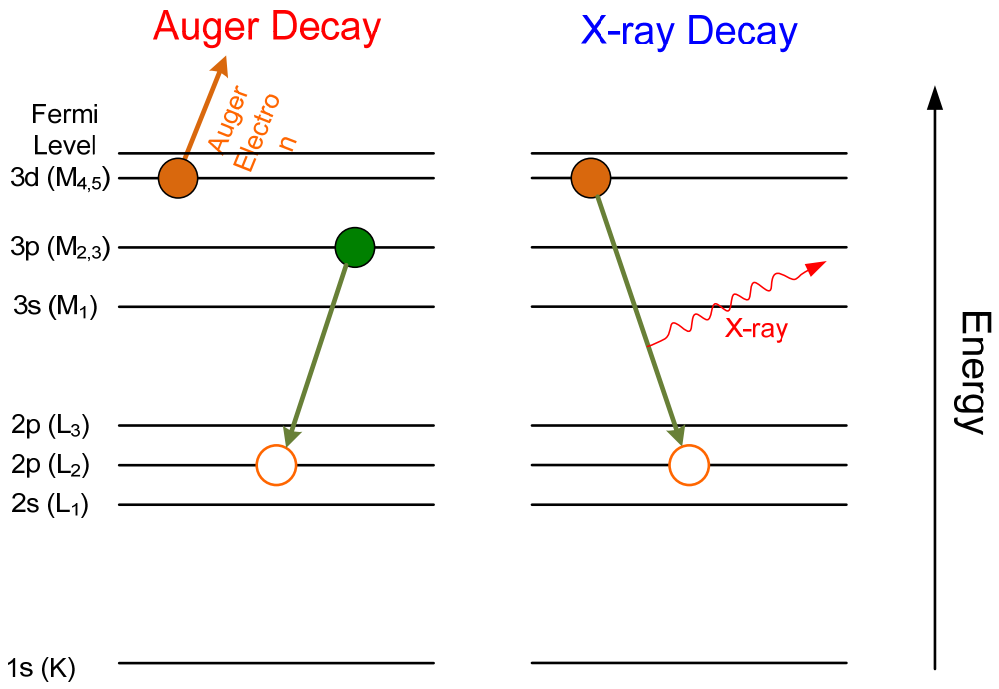

FIG. 23. Examples of competing transitions in which an inner-shell vacancy is filled.

Allowed x-ray transitions follow the dipole selection rules ($\Delta S = 0,\ \Delta l = \pm 1,\ \Delta L = 0,\ \pm 1,$ and $\Delta J = 0,\ \pm 1$). X-ray transitions that violate the electric dipole selection rules are said to be forbidden and have much lower transition rates. The dipole-allowed x-ray transitions to the K and L shells of single-vacancy atoms are shown in Fig. 24. Their transition energies are tabulated by Bearden [135, 136], Porter [137], Sevier [138], and Deslattes [139].

The de-excitation of K-shell vacancies is straightforward in that there is only one possible initial state. However, the de-excitation process is complicated for L-shell or higher shell vacancies by two factors: i) shells higher than the K-shell consist of more than one sub-shell and the de-excitation process depends on how the sub-shells are ionized, since different methods of ionization will yield different primary vacancy distributions, and ii) The original vacancies in a shell may rearrange through Coster-Kronig transitions [140] (i.e., transitions between the sub-shells of a major atomic shell). Coster-Kronig transitions make it is possible for a primary vacancy created in one of the sub-shells to be transferred to a higher sub-shell before the vacancy is filled by another transition. Therefore, the x-ray and Auger transition probabilities, and hence the fluorescence yield can differ by many orders of magnitude among various multiplet states of a given initial vacancy configuration [141-146].

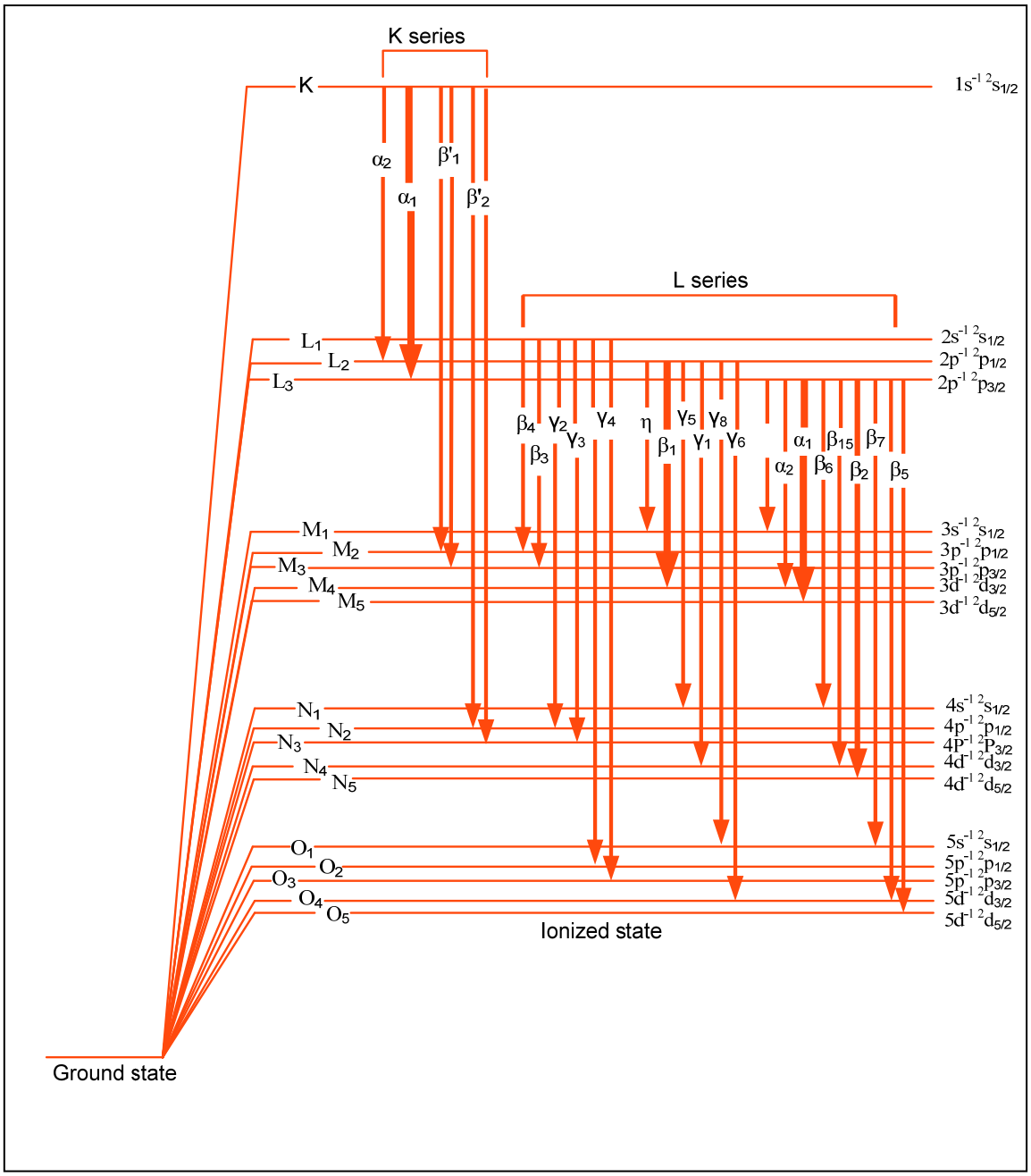

FIG. 24. Energy level diagram showing the allowed K and L x-ray transitions for a single-vacancy atom. Coupling with the angular momentum of other incomplete orbitals is neglected.

Spectra of x-rays emitted from multiply ionized atoms are more complex compared to those involving singly ionized atoms. For example the K x ray spectra of low to intermediate Z_2 atoms excited in heavy ion collisions are dominated by a series of satellite lines from initial states having single K- plus multiple L-shell vacancies and they contain prominent hypersatellite peaks from initial states having double K- plus multiple L-shell vacancies.

Two types of notation have been used to designate x-ray transitions. The conventional notation (Siegbahn notation) for x-ray transitions uses the capital letters K, L, M,… to indicate the location of the initial vacancy. Each x-ray transition is further specified by a Greek letter α, β, γ, etc., and a number. Another notation is the International Union of Pure and Applied Chemistry (IUPAC) notation, which is based upon the energy-level designations. The IUPAC x-ray nomenclature has the advantage of being simple and self-explanatory. A comparison of the IUPAC notation and the traditional (Siegbahn) notation for K x-rays is given in Table V.

The notation for satellite and hypersatellite transitions in the IUPAC nomenclature consists of the capital letters K, L, M, … with a superscript number to indicate the location and number of vacancies. For example, KL^n and K^2L^n, refer to initial states for K x-ray satellite and hypersatellites, respectively.

It should be kept in mind that each $K\alpha L^n$ or $K^2\alpha L^n$ group includes many transitions that are not normally resolved experimentally. These transitions are due to the coupling of angular momenta in the initial and finial states. Fig. 25 shows the allowed transitions in the L S coupling scheme for the Kα satellites when outer-shell vacancies are ignored.

Detailed studies of allowed x-ray transitions in multiply ionized atoms can be found in references [147-149].

TABLE V. Correspondence between the IUPAC and Siegbahn notation for K x-ray transitions [150]

IUPAC	Siegbahn		
K-L_3	$K\alpha_1$	$K\alpha$	
K-L_2	$K\alpha_2$		
K-M_3	$K\beta_1$	$K\beta_1'$	$K\beta$
K-M_2	$K\beta_3$		
K-$M_{4,5}$	$K\beta_5$		
K-$N_{2,3}$	$K\beta_2$	$K\beta_2'$	
K-$N_{4,5}$	$K\beta_4$		
K-$O_{2,3}$	$KO_{2,3}$		
K-$P_{2,3}$	$KP_{2,3}$		

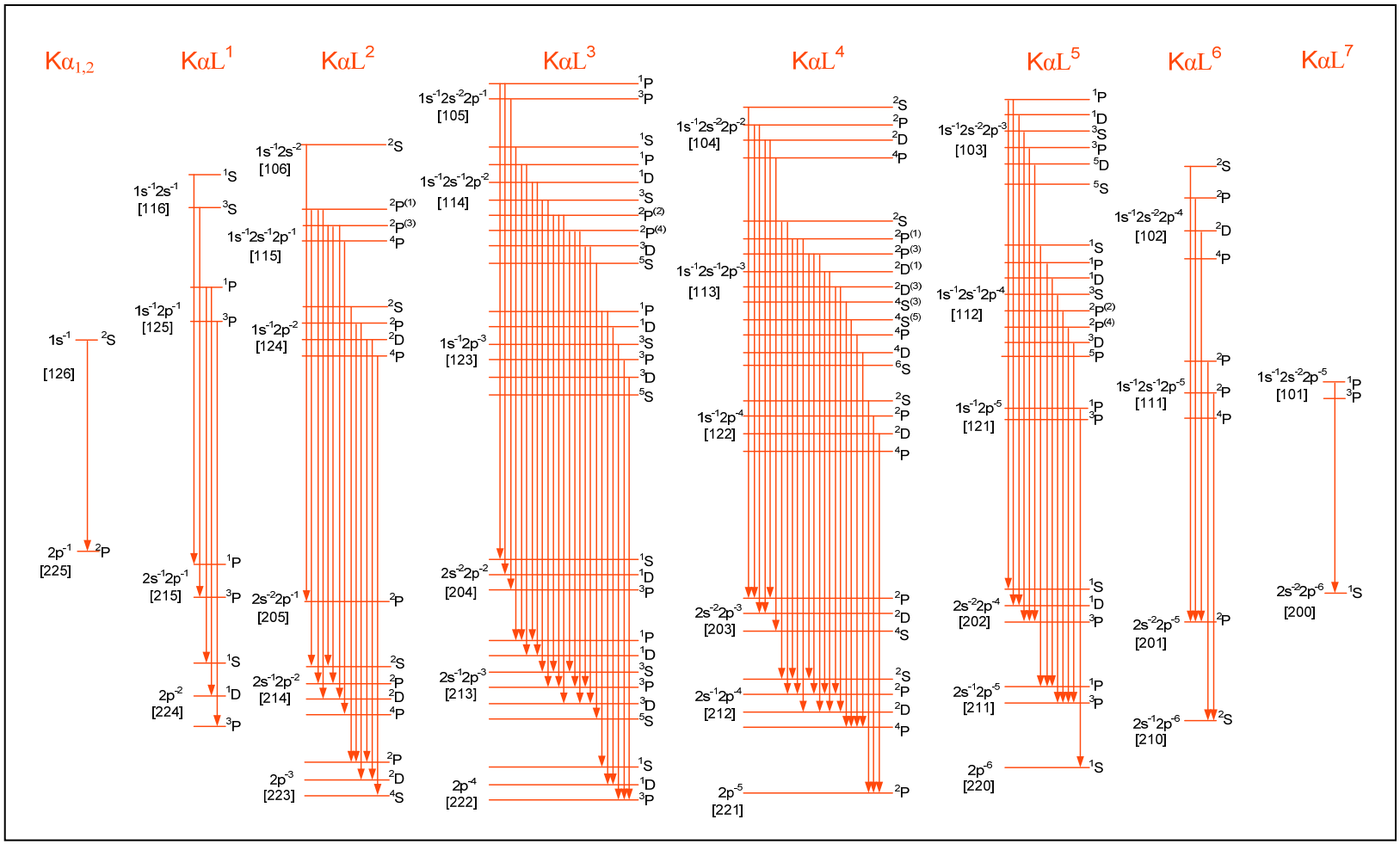

FIG. 25. Schematic representations of the allowed Kα x-ray transitions in singly and multiply ionized atoms, in the LS coupling scheme. Outer-shell vacancies (in the M shell and above) are ignored. $KαL^n$ represents transitions from the L-shell to the K-shell in atoms with n vacancies in L-shell and a single vacancy in the K shell in the initial state.

4.3. Transition rates

The natural energy profile of an electronic level can be described by a Lorentzian function. Likewise, the profile of a radiative transition can be described by a Lorentzian curve whose full width at half maximum (FWHM) is determined by the energy widths of the two states. The transition rate, S_{if}^{x}, from initial state i to final state f is given by

$$S_{if}^{x} = \Gamma_{if}^{x} / \hbar, \tag{39}$$

where Γ_{if}^{x} is the FWHM for the radiative transition and $\hbar$ is the reduced Plank's constant. The transition rate (S_{if}^{x}) also depends upon the strength of the coupling and upon the ways of the transition (i.e., the density of the final states). Assuming that different decay modes of the hole in the initial state are independent, the total transition rate S for the hole is given by the sum of the transition rates for all possible transitions. Specifically,

$$S = S_R + S_{NR} \tag{40}$$

where $S_R = \Gamma_R / \hbar$ and $S_{NR} = \Gamma_{NR} / \hbar$ are the total rates for radiative and nonradiative transitions respectively, while Γ_R and Γ_{NR} are the corresponding total FWHM's. The total FWHM is given by

$$\Gamma = \Gamma_R + \Gamma_{NR} \tag{41}$$

The theoretical natural widths for the K shell are shown in Fig. 26 as a function of atomic number. This figure also shows that the Auger process is dominant for light atoms while the radiative process is dominant for heavy atoms.

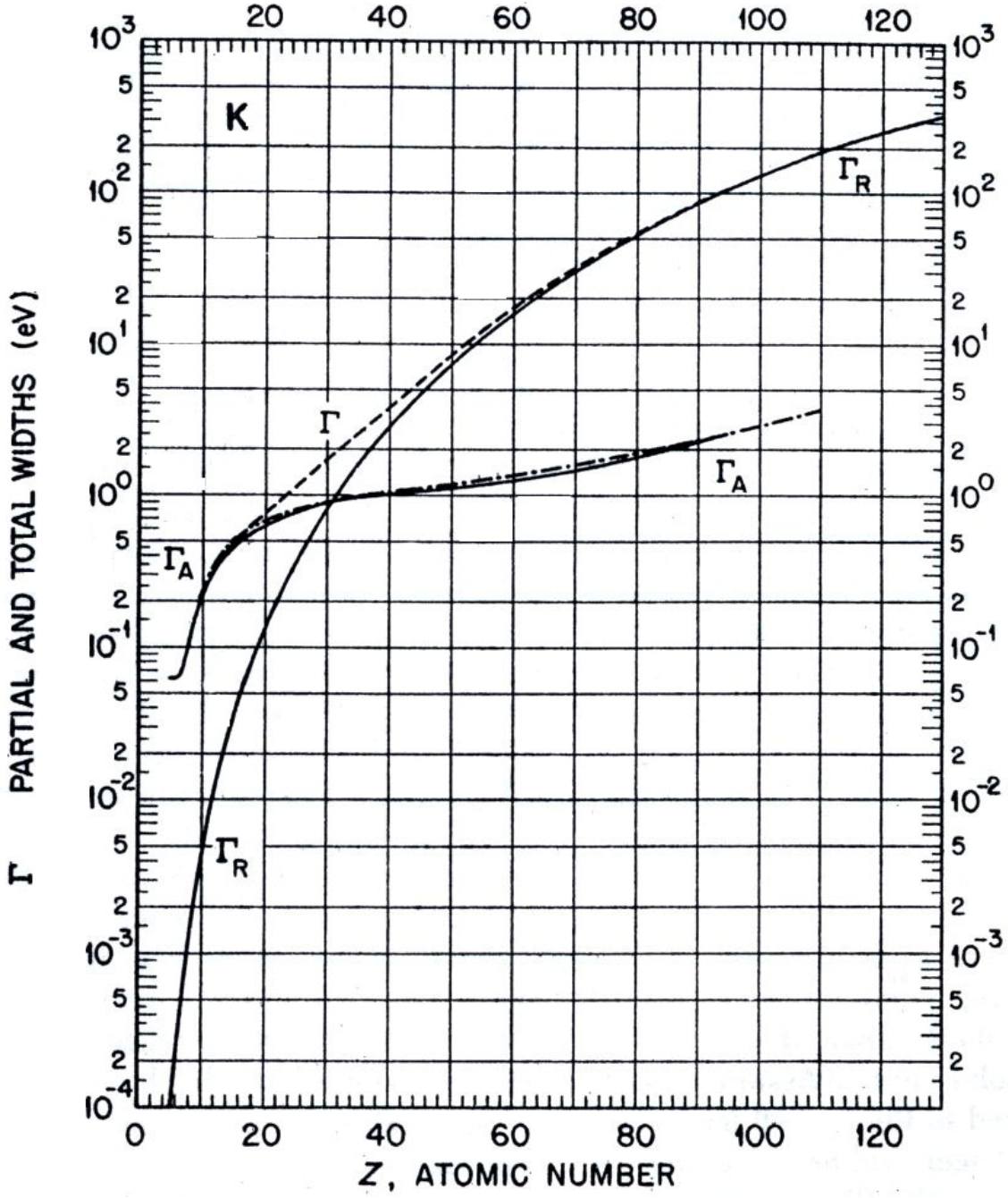

FIG. 26. Theoretical level widths for atomic K shells as a function of the atomic number (Taken from Ref. [151]).

4.4. Fluorescence yield

The K-shell fluorescence yield ω_K is given by

$$\omega_K = \Gamma_R^K / \Gamma^K , \tag{42}$$

where Γ_R^K and Γ^K are the radiative rate and the total rate, respectively, of all transitions that fill a K vacancy. Thus, the number of emitted K x-rays is $\omega_K n_K$, where n_K is the number of K vacancies produced in the excitation process.

4.4.1. Single vacancy K-shell fluorescence yield

Fig. 27 (adapted from reference [151]) shows the theoretical K-shell fluorescence yield as a function of atomic number. Evidently, the theoretical values of ω_K were obtained for atomic number $4 \leq Z \leq 54$ by McGuire [152, 153] and Walters et al. [154-156] using the Hartree-Fock-Slater method. Chen et al. [157] used a Dirac-Hartree-Slater approach to determine the ω_K values of elements in the atomic number range of $18 \leq Z \leq 96$. Kostroun et al. [158] and Crasemann [159] presented computations of ω_K for elements in the atomic number range of $10 \leq Z \leq 70$, combining Scofield's [160] radiative transition rates. Other studies of single-vacancy K-shell fluorescence yields are described in ref. [161-169].

Based on the fit of experimental values of K-shell fluorescence yield ω_K as a function of target atomic number, several semiempirical formulas have been suggested [1, 161, 170]. One such formula was given by Wentzel

$$\omega_K /(1-\omega_K) \approx 10^{-6} Z^4 . \tag{43}$$

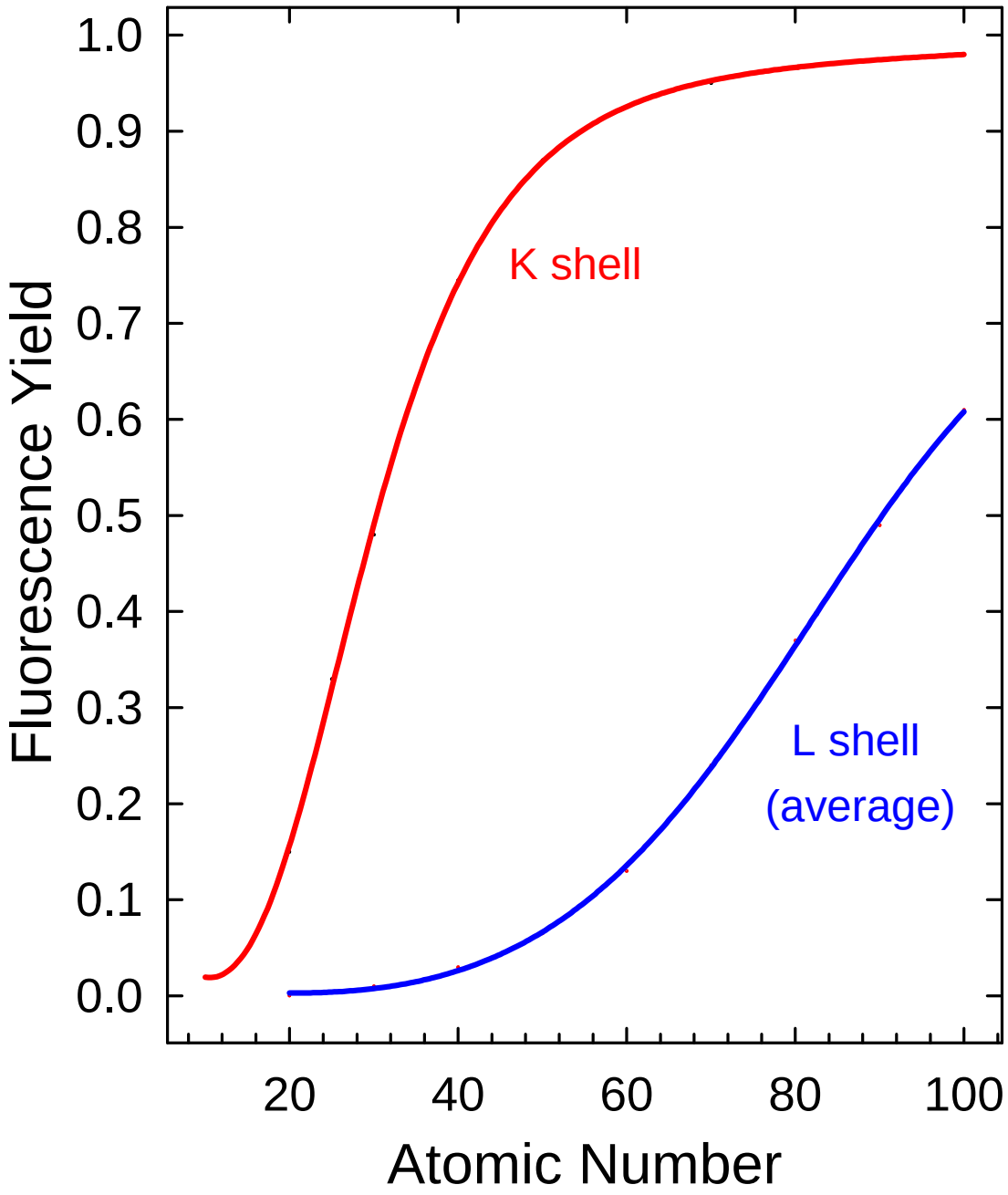

FIG. 27. Theoretical single vacancy fluorescence yields of the K and L shells. The plotted curve for the L shell represents an average of L_1, L_2, and L_3 yields [151].

Burhop [171] developed a semiempirical equation based on Eq. (43),

$$\omega_K/(1-\omega_K) = (-0.217 + 0.03318Z - 1.14\times10^{-6}Z^3)^4 . \quad (44)$$

Bambynek et al. [161] reevaluated the experimental ω_K values and fitted 44 'most reliable' values of ω_K. Their result was given by

$$\omega_K/(1-\omega_K) = [(0.015\pm0.010) + (3.27\pm0.05)\times10^{-2}Z - (0.64\pm0.071)\times10^{-6}Z^3]^4 . \quad (45)$$

Langenberg [170] used a seven-parameter fit over a large range of experimental fluorescence yields and his result is given by

$$\begin{aligned}\omega_K/(1-\omega_K) = [&(-0.0205\pm0.014) + (4.75\pm0.35)\times10^{-2}Z \\ &-(16\pm3)\times10^{-4}Z^2 + (70\pm14)\times10^{-6}Z^3 \\ &-(145\pm30)\times10^{-8}Z^4 + (135\pm30)\times10^{-10}Z^5 \\ &-(46\pm12)\times10^{-12}Z^6]^4 .\end{aligned} \quad (46)$$

Hanke et al [172] developed the following expression for elements from Mg to Zr

$$\omega_K/(1-\omega_K) = 0.3704 - 6.0447\times10^{-2}Z + 3.1331\times10^{-3}Z^2 - 3.9215\times10^{-5}Z^3 \quad (47)$$

Hubbell et al. [1] combined theoretical and experimental data and derived the following analytical expressions

$$\omega_K(1\le Z\le100) = \left[\sum_{i=0}^{3} C_i Z^i\right]^4 \left\{1+\left[\sum_{i=0}^{3} C_i Z^i\right]^4\right\}^{-1} , \quad (48)$$

where

$$C_0 = 0.0370\pm0.0052 ,$$

$$C_1 = 0.03112\pm0.00044 ,$$

$$C_2 = (5.44\pm0.11)\times10^{-5} ,$$

$$C_3 = -(1.25\pm0.07)\times10^{-6} .$$

Comparison of these semiempirical predictions as function of the atomic number is shown in Fig. 28. Results of the early work by Burhop are significantly different from the other predictions in the low atomic number range due to insufficient available experimental data. Langenberg's predictions, which were employed in the current investigation, are slightly lower than the others in the atomic number range of around 45 to 80. Hubbell's predictions are slightly higher than the others for Z_2>82.

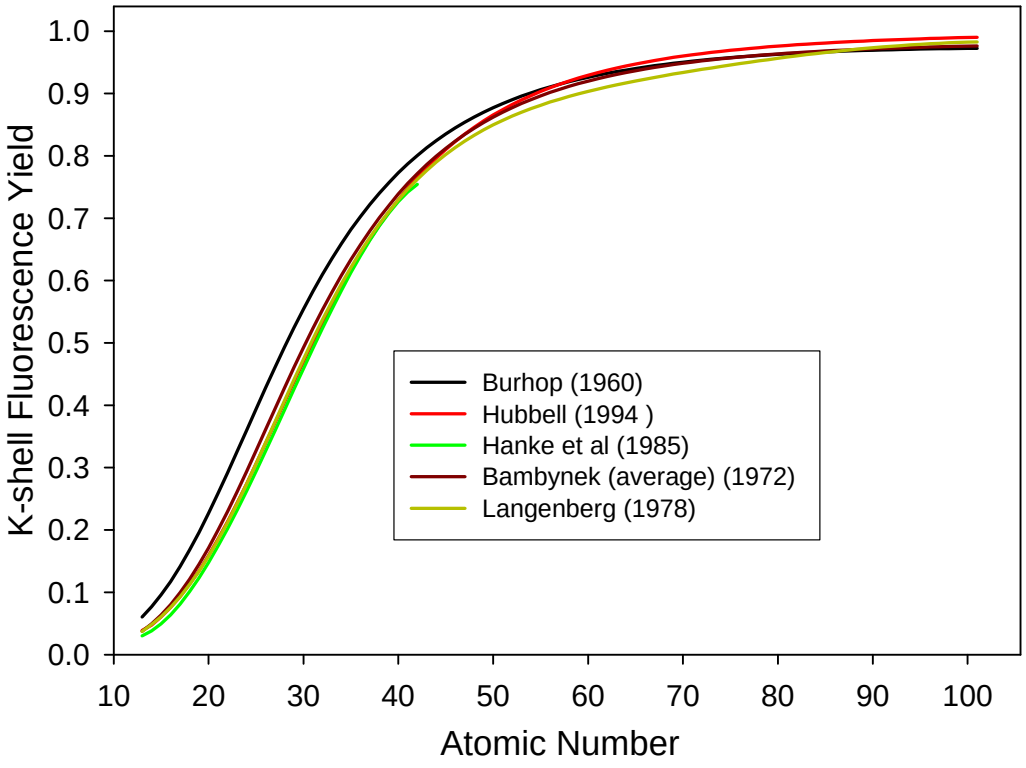

FIG. 28. Comparison of semiempirical predictions of K-shell fluorescence yields. Black line: Burhop [171], red line: Hubbel [1], green line: Hanke et al. [172], brown line: Bambynek [161], dark green line: Langenberg [170].

4.4.2. Multiple vacancy fluorescence yield

Multiple vacancies in the K, L and outer shells affect the radiative and nonradiative rates by reducing the number of electrons available for a given transition, making some nonradiative transitions energetically forbidden, and modifying the atomic wave functions in the initial and final state. Therefore, the fluorescence yield of a multiply ionized atom may be significantly different from that of a singly ionized atom.

In order to derive the K vacancy production cross section from the K x-ray production cross section for heavy-ion collisions, one needs to know the distribution of vacancy configuration in the initial state and the corresponding sets of transition rates. However, neither is very well known.

So far, multiple vacancy fluorescence yield calculations have been attempted for a limited number of rearrangement transitions and decay channels by Watson [143], Anagnostopoulos [173, 174], Polasik et al. [175], Pajek et al. [119], Horvat et al. [176], Kobal [177], and Kadhane et al [178].

Recently, Horvat et al. [176] have developed a method for deducing the original L-shell vacancy distribution, the average number of M-shell vacancies at the time of the collision, and the effective K-shell fluorescence yield. The method is based on K x-ray spectra measured in high resolution and takes into consideration multi-step rearrangement of the initial electronic configurations due to allowed radiative and non-radiative transitions occurring between the time of collision and the time of K x-ray emission. The steps involved in method are summarized as follows.

i) The original electronic configuration distribution (produced at the time of the

collision) is estimated from the spectrum and the L shell vacancy distribution is assumed to be binomial [20, 65], characterized by the average ionization probability per electron p_L^0. The distribution of L electrons over the L subshells (L_1, L_2 and L_3) is taken to be statistical, and the distribution of M-shell electrons is such that the 3p orbitals are preferentially populated. It was assumed that no electrons are present in the N shell and above. The original average number of L electrons, n_L, and M electrons, n_M, were related by employing Sulik et al.'s formula [64]. The transition rates for multiply ionized ions were derived from the available single vacancy transition rates employing the scaling procedure of Larkins [179].

ii) Then the evolution of each contributing configuration is followed along all decay branches until no further decays are possible except those that result in the filling of the K vacancy. An inventory list of the resulting K x-ray transitions provides the information necessary to determine the relative intensities of the Kα and Kβ satellite peaks, the average number of M vacancies associated with each one of them, and, most importantly, the average fluorescence yield.

iii) After comparison between the predicted and the measured x-ray spectrum, the assumed original distribution of configurations is modified, and the calculations repeated until satisfactory match between the two spectra is achieved.

4.5. K x-ray spectra

A typical K x-ray spectrum obtained with the curved crystal spectrometer for a Cu target bombarded by 20 MeV/amu Xe projectiles is shown in Fig. 29. In the spectrum,

the two most intense peaks on the low energy side, labeled $K\alpha_1$ and $K\alpha_2$ originate from single K-vacancy initial states and are referred to as diagram lines. In the current investigation, the $K\alpha_1$ and $K\alpha_2$ peaks were used for energy calibration because their energies are known with good accuracy since transitions from multiply ionized states contribute very little to these peaks.

The peaks labeled $K\alpha L^n$ (n = 1, 2, …7) are known as the Kα x-ray satellites. They are due to Kα x-ray transition in atoms having single K- plus multiple L- vacancy initial states. The intensity distribution of the Kα satellite peaks has been found to closely follow a binominal distribution[142]. Since a maximum of eight electrons can occupy the L-shell, there should be eight Kα satellite peaks. However, the $K\alpha L^0$ is very small and obscured by much stronger Kα diagram peaks while $K\alpha L^8$ peak does not exist because at least one L electron is needed for a Kα transition.

The set of peaks to the right of the Kα satellites are called the Kα hypersatellites. They are due to Kα x-ray transitions in atoms having double K- plus multiple L-vacancy initial states, and have structure similar to that of the Kα satellites but with lower intensities. .

The right most peak in Fig. 29 labeled Kβ is due to the transitions from the M-shell to the K-shell. Structure of the Kβ satellites and Kβ hypersatellites (not shown) is similar to that of the Kα satellites and hypersatellites, but the x-rays that contribute to these peaks have energies above the Cu K edge and are greatly attenuated inside the target. These peaks are located at higher energies than the Kβ peak and are not shown in Fig. 29.

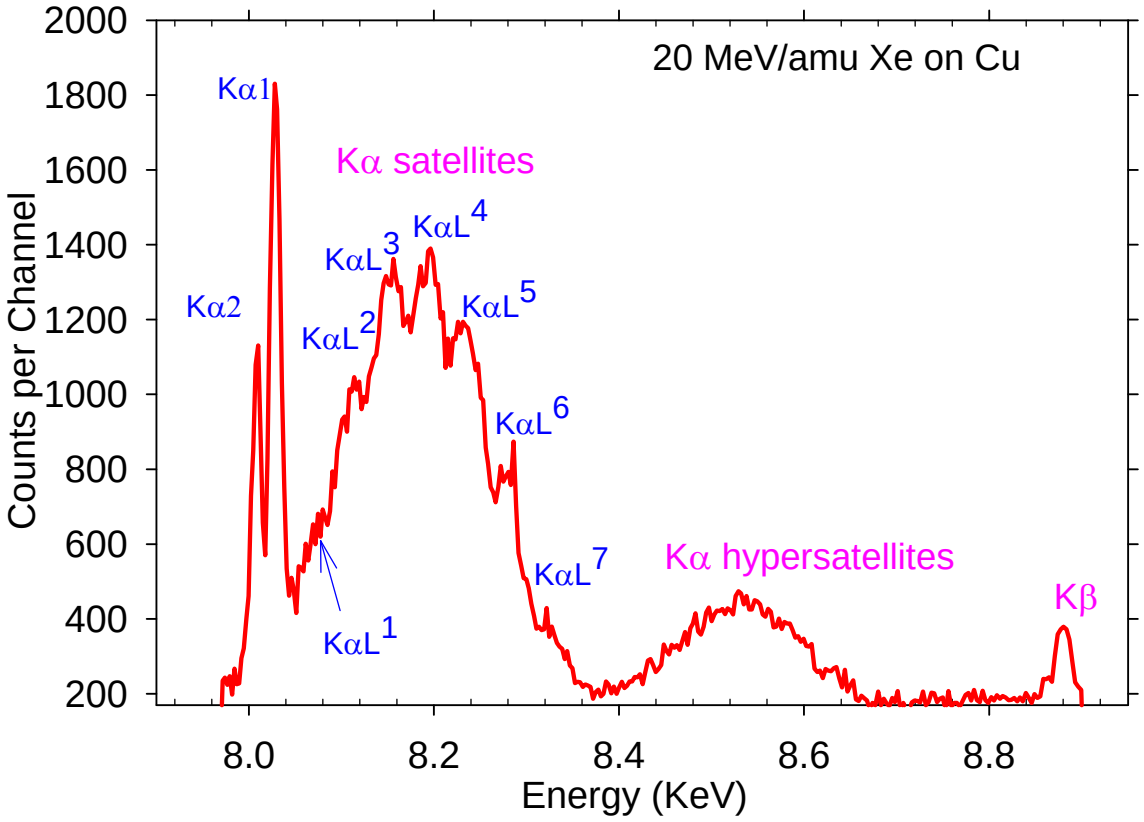

FIG. 29. High-resolution K x-ray spectrum of Cu, produced by bombardment with 20 MeV/amu Xe projectiles.

Typical energy-dispersive x-ray spectra obtained with a Si(Li) detector (having a resolution of about 200 eV) for Cu target bombarded by 20 MeV/amu Ar, Kr, and Xe projectiles are shown in Fig. 30. The dashed-lines show the Kα (black) and Kβ (red) diagram transition energies (8.041 and 8.905 keV, respectively). The Kα diagram and satellite peaks are not resolved here while the Kα hypersatellites are manifested as a shoulder on the high-energy side of the Kα peak. As the projectile atomic number increases, so does the degree of multiple ionization of the L and M shell. This causes a broadening of the satellite peaks and results in a shift toward higher energies. The other structures visible in the figure are due to x-rays emitted from the projectile or due to pulse pile-up. The projectile x-rays sometimes cause an overlap-problem which can make the accurate determination of target K x-ray yields difficult. The overlap-problem will be discussed in detail in Chapter V.

High and low resolution K x-ray spectra produced by 20 MeV/amu Xe projectiles for a Cu target are compared in Fig. 31. This figure shows that the dominant contributors to the low resolution Kα peak are the Kα satellite transitions.

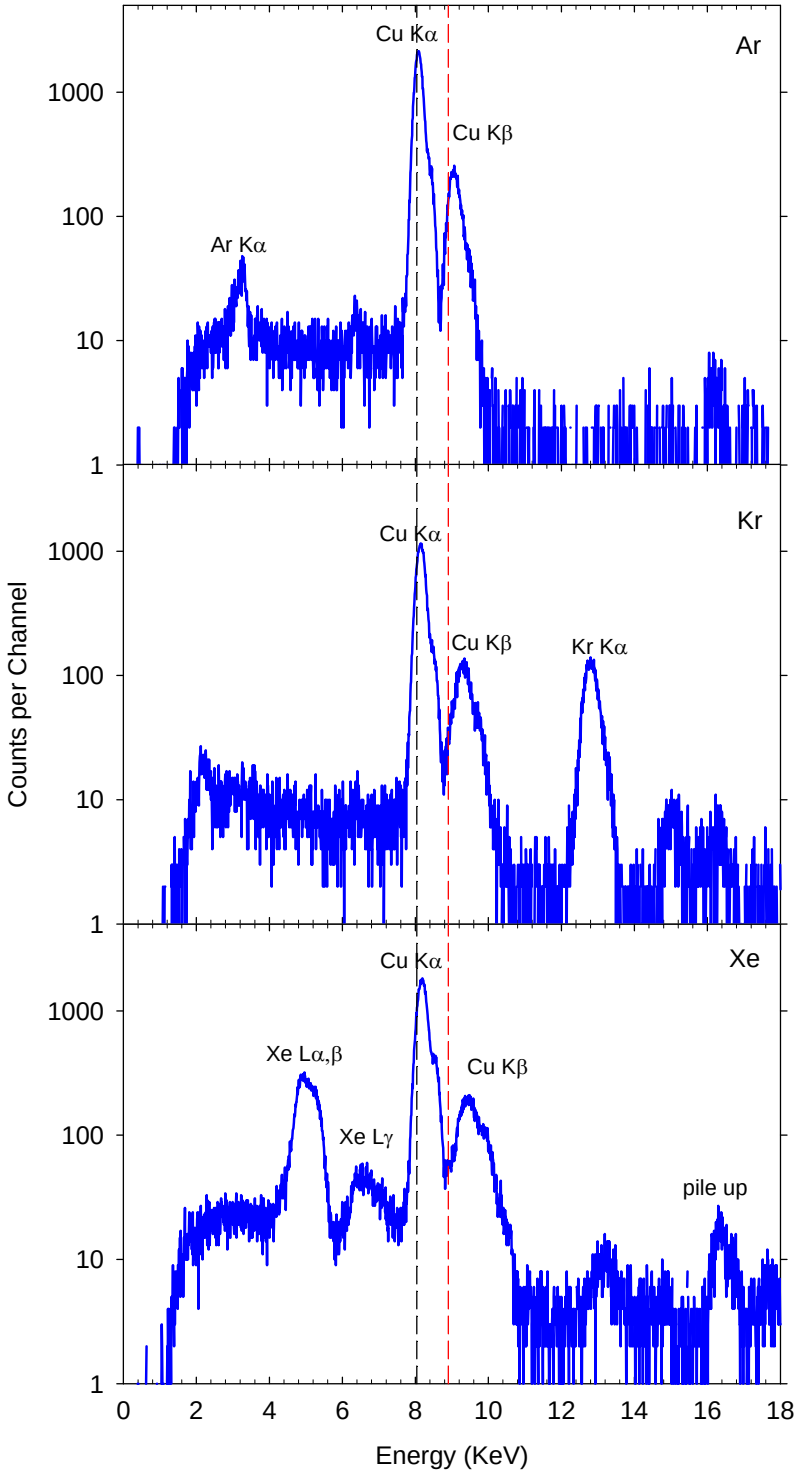

FIG. 30. K x-ray spectra excited by 20 MeV/amu projectiles passing through a Cu foil, measured using a Si(Li) detector.

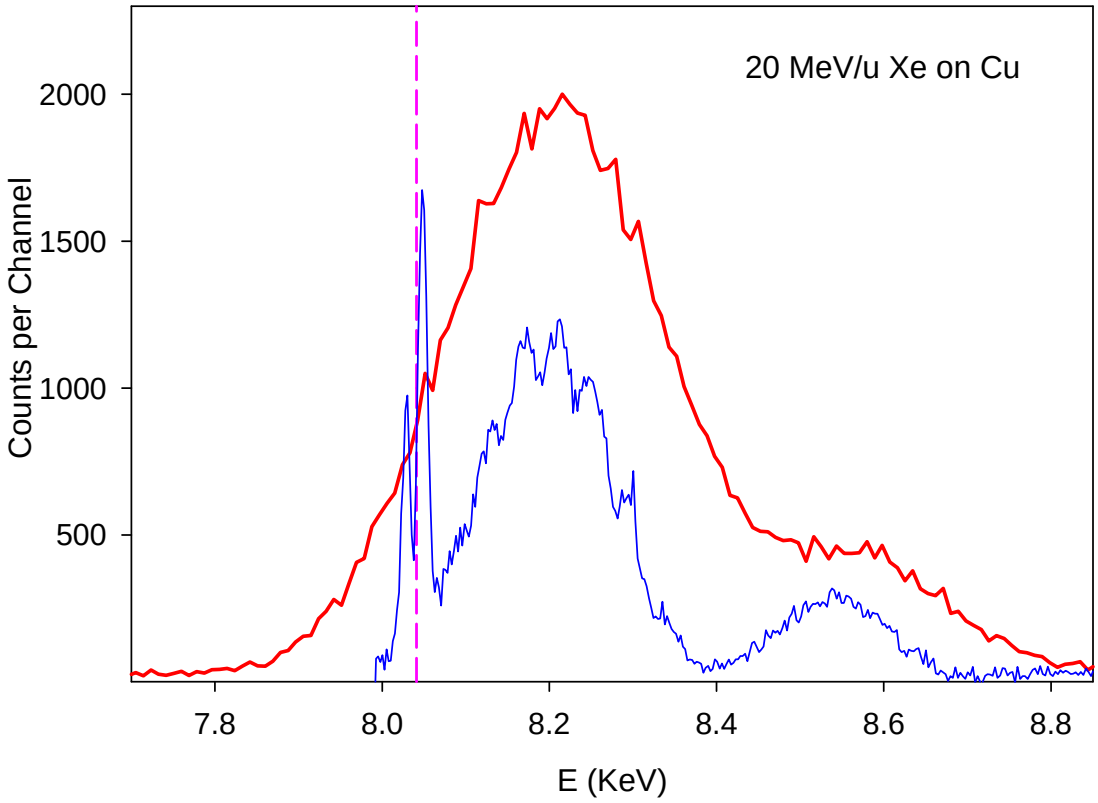

FIG. 31. Comparison of Cu K x-ray spectra produced by 20 MeV/amu Xe projectiles measured in high resolution (shown in blue) and low resolution (shown in red). The pink dashed line indicates the position of the average energy of the Cu Kα1 and Kα2 diagram lines.

CHAPTER V

DATA ANALYSIS AND RESULTS

5.1. Introduction

Target x-ray spectra were recorded using a personal computer featuring a dedicated pulse-height analyzer/multichannel scaler expansion board (Oxford Instruments, Inc.) and the accompanying software (PCA). The collected number of counts in each peak of interest was at least 1000 to keep the statistical errors below 3%. Each spectrum was measured at least twice to verify the consistency. Peaks in the spectra were fitted with Gaussian functions using the software PeakFit (Systat Software Inc., Richmond, California, USA). Yields from x-ray spectra taken in the same run generally were in agreement to within ±3%.

Analysis of the wavelength-dispersive spectra differed from the analysis of the energy-dispersive spectra. Therefore, the two cases will be discussed separately in the following sections.

5.2. Projectile energy loss effects

The average projectile energy for Kα x-ray detection ($\overline{E}$) was calculated by taking into account the Kα x-ray detection probability as a function of projectile penetration

depth, the dependence of the Kα x-ray production cross section on projectile energy, and the rate of projectile energy loss in the target. The number of x-rays $dN(x)$ that are produced in the depth interval dx and are transmitted over distance x through the target in the direction of the detector, is given by

$$dN(x) = N_p \sigma(x) \eta \Omega e^{-\mu x} dx, \tag{49}$$

where Np is the number of projectiles, $\sigma(x)$ is the x-ray production cross section, η is the number of target atoms per unit area, Ω is the geometry factor, and μ is the mass absorption coefficient. The total number of x-rays that reach the detector is

$$N = N_p \Omega \int_0^t \sigma(x) e^{-\mu x} dx, \tag{50}$$

where t is the target thickness. Therefore, the probability that an x-ray is produced between x and x + dx and transmitted through the target toward the detector is

$$P(x)dx = \frac{dN(x)}{N} = \frac{\sigma(x)e^{-\mu x}\ \mathrm{dx}}{\int_0^t \sigma(x)e^{-\mu x} dx}. \tag{51}$$

Thus, the average projectile energy for x-ray production and the average value of the target thickness are given respectively by

$$\overline{E} = \int_0^t E(x)P(x)dx = \frac{\int_0^t E(x)\sigma(x)e^{-\mu x} dx}{\int_0^t \sigma(x)e^{-\mu x} dx}, \tag{52}$$

and

$$\bar{x} = \int_0^t xP(x)dx = \frac{\int_0^t x\sigma(x)e^{-\mu x}dx}{\int_0^t \sigma(x)e^{-\mu x}dx}. \quad (53)$$

Numerical methods were employed to calculate the quantities $\bar{E}$ and $\bar{x}$, with the Kα x-ray transition energies taken from Ref. [139] and x-ray attenuation coefficients obtained from Ref. [180]. In Eq. (52), the quantity $E(x)$ was calculated with the following formula

$$E(x) = E_0 - \int_0^t S(x)dx. \quad (54)$$

In Eq. (54), the quantity E_0 is the incident projectile energy and $S(x) = dE/dx$ is the stopping power calculated with software SRIM [181]. The x-ray production cross section $\sigma(x)$ depends on projectile energy and was calculated using the ECPSSR theory. Results of the calculated average projectile energies ($\bar{E}$) are listed in Table VI along with the incident projectile energies.

In Fig. 32, the average projectile energy for Kα x-ray detection is plotted as a function of the projectile penetration depth for 4.0 and 24.8 MeV/amu Ar projectiles.

The relative average energy loss [defined as $(E_i - \bar{E})/E_i \times 100\%$] is plotted in Fig. 33 as a function of incident projectile energy. It was less than 10% in all cases except for the Sm target, which was significantly thicker than the others.

TABLE VI. Incident projectile energies and the average projectile energies (MeV/amu) used in the current project.

target $cm^2/\mu g$	Incident MeV/amu	Ar	Kr	Xe	$cm^2/\mu g$	MeV/amu	Ar	Kr
Al	2.5	2.33	2.31	2.31	Al	2.5	2.33	2.31
	4.0	3.85	3.81	3.81		4.0	3.85	3.81
	6.0	5.87	5.83	5.82		6.0	5.87	5.83
	9.9	9.80	9.76	9.74		9.9	9.80	9.76
	15.0	14.92	14.88	14.86		15.0	14.92	14.88
	20.0	19.94	19.90	19.87		20.0	19.94	19.90
	24.8	24.75	24.71	24.69		24.8	24.75	24.71
Cu	2.5	2.27	2.24	2.24	Cu	2.5	2.27	2.24
	4.0	3.78	3.73	3.50		4.0	3.78	3.73
	6.0	5.81	5.75	5.73		6.0	5.81	5.75
	9.9	9.75	9.68	9.65		9.9	9.75	9.68
	15.0	14.88	14.81	14.77		15.0	14.88	14.81
	20.0	19.9	19.83	19.80		20.0	19.9	19.83
	24.8	24.71	24.65	24.78		24.8	24.71	24.65
Ag	2.5	2.33	2.31	2.31	Ag	2.5	2.33	2.31
	4.0	3.84	3.80	3.80		4.0	3.84	3.80
	6.0	5.86	5.81	5.800		6.0	5.86	5.81
	9.9	9.78	9.73	9.70		9.9	9.78	9.73
	15.0	14.90	14.85	14.82		15.0	14.90	14.85
	20.0	19.92	19.87	19.84		20.0	19.92	19.87
	24.8	24.73	24.68	24.65		24.8	24.73	24.68
Ta	2.5	2.29			Ta	2.5	2.29	
	4.0	3.78	3.74			4.0	3.78	3.74
	6.0	5.80	5.87	5.86		6.0	5.80	5.87
	9.9	9.73	9.65	9.62		9.9	9.73	9.65
	15.0	14.88	14.81	14.78		15.0	14.88	14.81
	20.0	19.88	19.8	19.76		20.0	19.88	19.8
	24.8	24.72	24.63	24.70		24.8	24.72	24.63

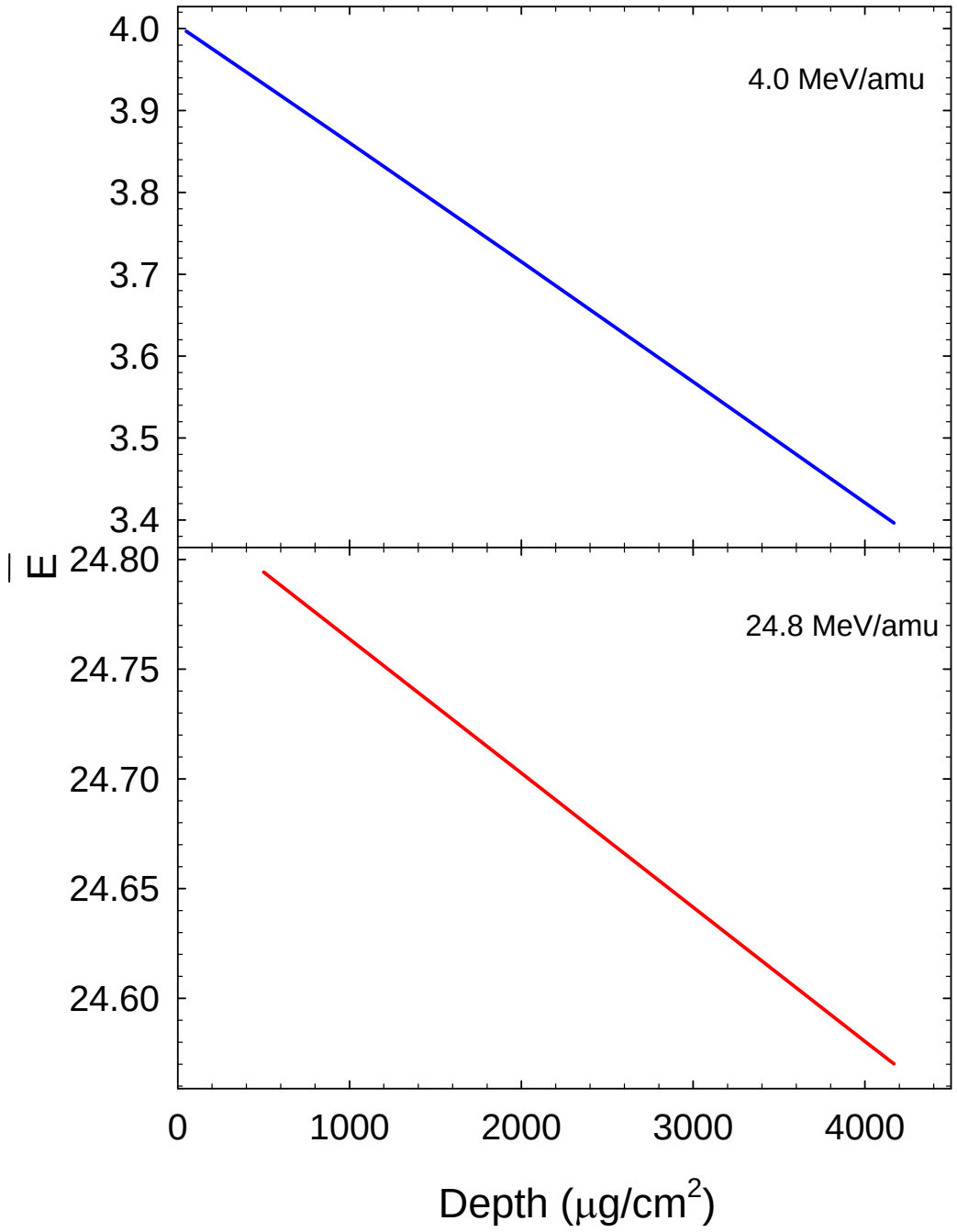

FIG. 32. The average projectile energy for Kα x-ray detection as a function of penetration depth for Ar on Sm.

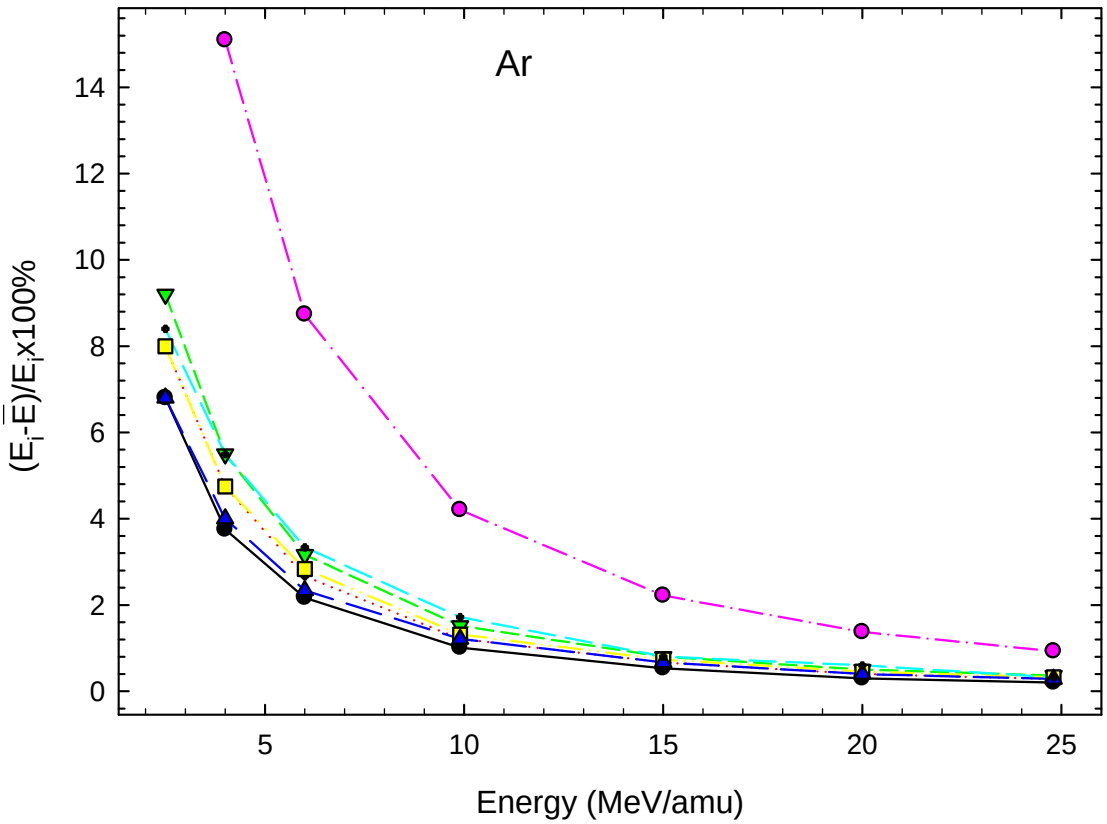

FIG. 33. Relative average energy loss as a function of incident projectile energy.

5.3. Wavelength-dispersive spectra

The purpose of the wavelength-dispersive measurements was to provide additional information needed in order to convert the measured x-ray production cross sections to vacancy production cross sections. Specifically, the systematics of L-shell ionization in K-shell ionizing collisions as a function of projectile energy as well as projectile and target atomic numbers was studied to help determine the appropriate values of K-shell fluorescence yields. Also, the relative contribution from the diagram transitions was determined in order to take into account the secondary ionization processes.

X-ray spectra collected with the crystal spectrometer usually have background that had to be subtracted (to be discussed in detail in 5.3.1.). K x-rays emitted below the surface of the target must travel through a portion of the target before being detected (to be discussed in 5.3.3.). However, some of the x-rays are absorbed before they can escape from the target media. This process also has an energy dependence and displays significant discontinuities at the photon energies corresponding to the binding energies of the target atoms (to be discussed in detail in 5.3.3. and 5.3.4.). For heavy ion-atom collisions, there are significant contributions from secondary process and these contributions must be taken into account (to be discussed in 5.3.6.). Finally, multiple vacancy fluorescence yields (to be discussed in 5.3.7.) have to be employed to obtain accurate ionization cross sections.

5.3.1. Background subtraction

For each group of peaks, the background was determined by selecting two surrounding regions, one on the low-energy side and the other on the high-energy side. The average number of counts was then computed for each region. These numbers were assigned to the mid-points of the regions and used to construct a linear function of channel number that represented the background. The background was then subtracted from the spectrum channel by channel. An example of this correction is shown in Fig. 34. In cases where only one background region was available (because the spectrum either began or ended at a point above background), the background was assumed to be constant.

5.3.2. Energy calibration

Two different crystals were used in present investigation. Ammonium dihydrogen phosphate (ADP) was used to measure Al x-rays, while LiF (200) crystal was used in the measurements with all the other targets. The spectra were measured in the first order of reflection, except for Cu K x-rays which were measured in second order.

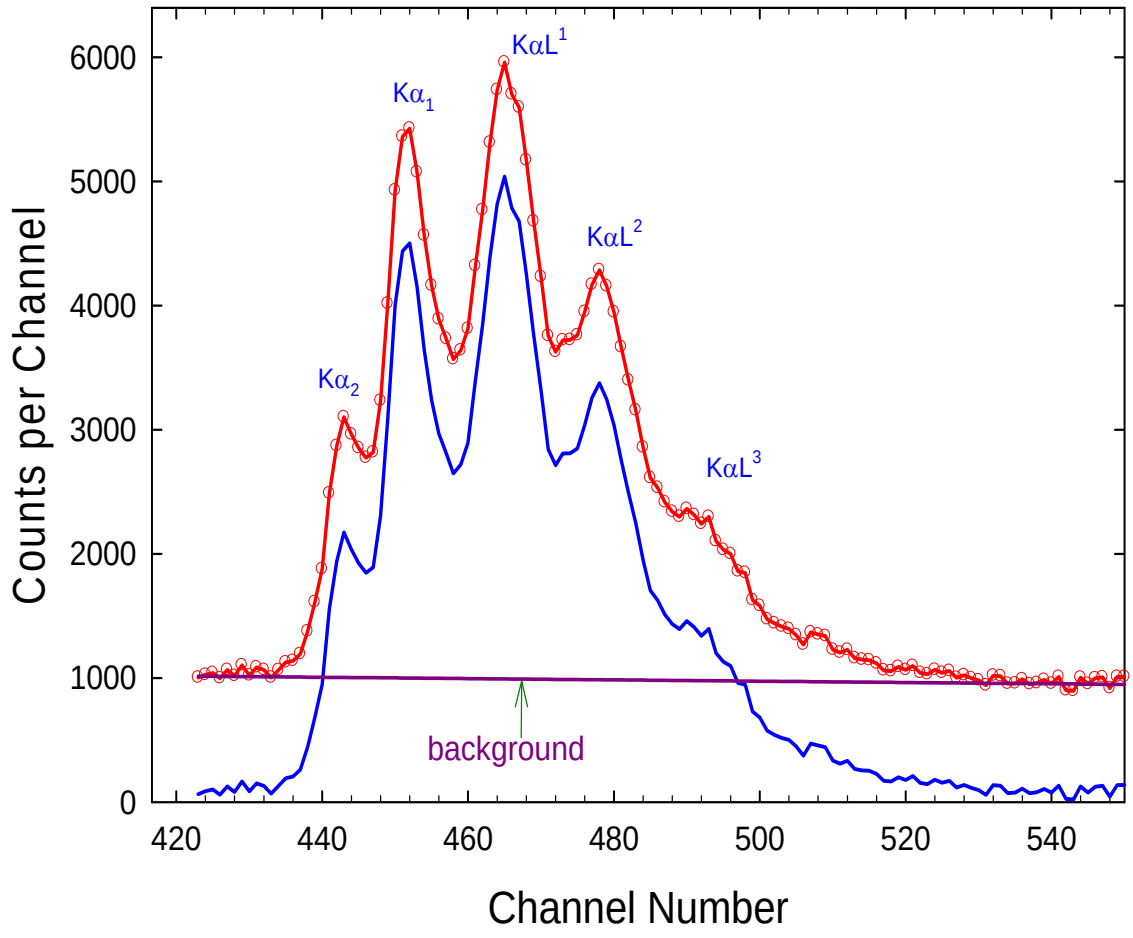

FIG. 34. Spectrum of Kα x rays produced by bombardment of Cu target by 25 MeV/amu Ar projectiles (red curve). The blue curve is the same spectrum after background subtraction. The purple linear line is the background. The two regions for the background determination were centered at 8.0 keV and 8.3 keV.

For each crystal and for each order of reflection, the position P of the spectrometer, identified by its odometer, is related to the wavelength λ of the detected x-ray according to the equation

$$P = \lambda s + b \tag{55}$$

where s and b are constants that depend on the orientation of the focal circle and crystal plane. Solving the equation for λ and converting wavelength to energy, one obtains the following expression relating the x-ray energy to the calibration parameters

$$E(keV) = \frac{s'}{P - b}, \tag{56}$$

where $s' = hcs$, h is the Plank's constant, and c is the speed of light in vacuum. Parameters s' and b can be determined in a least squares analysis based on Eq. (56) and a set of calibration points.

Centroids of the Kα and Kβ diagram peaks as well as the location of the absorption edge were chosen as the internal energy calibration points whenever they were available.

5.3.3. Correction for self-absorption

Photons can interact with matter by means of three mechanisms: 1) the photoelectric effect, in which the photon disappears and its entire energy is transferred to a bound electron in a single collision, 2) Compton scattering, in which a photon is deflected from its original path and transfers only a part of its energy to a bound electron, and 3) pair production, in which a photon with energy above 1.02 MeV is converted to a electron and positron, moving in opposite directions. The photoelectric effect is the dominant process for low-energy photons. The cross section for the photoelectric effect decreases

as the photon energy increases. The Compton Effect is the most important mechanism at photon energies between 100 keV and several MeV, while pair production dominates at high photon energies (see ref. [182] p.224-229).

The attenuation coefficient, μ, describing fractional reduction of the beam intensity, -dI/I, in a thin layer of thickness dt in an absorbing medium, is given by

$$-\frac{dI}{I} = \mu dt \,. \tag{57}$$

For a homogeneous medium, Eq. (57) is readily integrated to give the well known Beer-Lambert law:

$$I = I_0 e^{-\mu t}, \tag{58}$$

where t is the thickness along the beam path, I_0 is intensity of the incident beam, and I is the intensity of the emergent beam.

The mass attenuation coefficient is given by

$$\mu_{\mathrm{m}} = \mu\rho \,, \tag{59}$$

where ρ is the absorber density.

The mass attenuation coefficients for the above three processes are usually calculated and reported as cross sections in the units of barns per atom. A more convenient unit for the mass attenuation coefficient is cm^2/g, where the target atom's mass is used to make the conversion from barns per atom. The mass attenuation coefficient, μ_m, is proportional to the total photon interaction cross section, σ_{tot}, through the relation

$$\mu_m = \sigma_{tot} \frac{N_A}{M} \,, \tag{60}$$

where N_A is Avogadro's number and M is the atomic weight of the absorber material. In the energy range of interest here, the total photon interaction cross section is given by

$$\sigma_{tot} = \sigma_p + \sigma_c , \tag{61}$$

where σ_p is the photoelectric effect cross section and σ_C is the Compton scattering cross section. Fig. 35 shows the energy dependence of the mass attenuation coefficient for each of the targets used in the present work in the energy range between 1 keV and 100 keV.

Crystal spectrometers are very inefficient for x-ray detection, requiring that x-rays enter the spectrometer with the proper directional vector for acceptance, be diffracted by the crystal, and finally be detected. The efficiencies for the latter two processes depend on the x-ray wavelength, but that dependence can be neglected over a narrow energy range.

The number of photons, n, that penetrate thickness t of a medium is given by

$$n = n_0 e^{-\mu t} \tag{62}$$

where n_0 is the incident number of photons and μ is the total absorption coefficient of the medium. If one assumes that n_0 photons are produced by the beam particles uniformly by along their path over target thickness t' (see Fig. 36), then dn, the number of photons escaping from target depth z toward the detector is

$$dn = \frac{n_0}{t'} e^{-\mu x} dz , \tag{63}$$

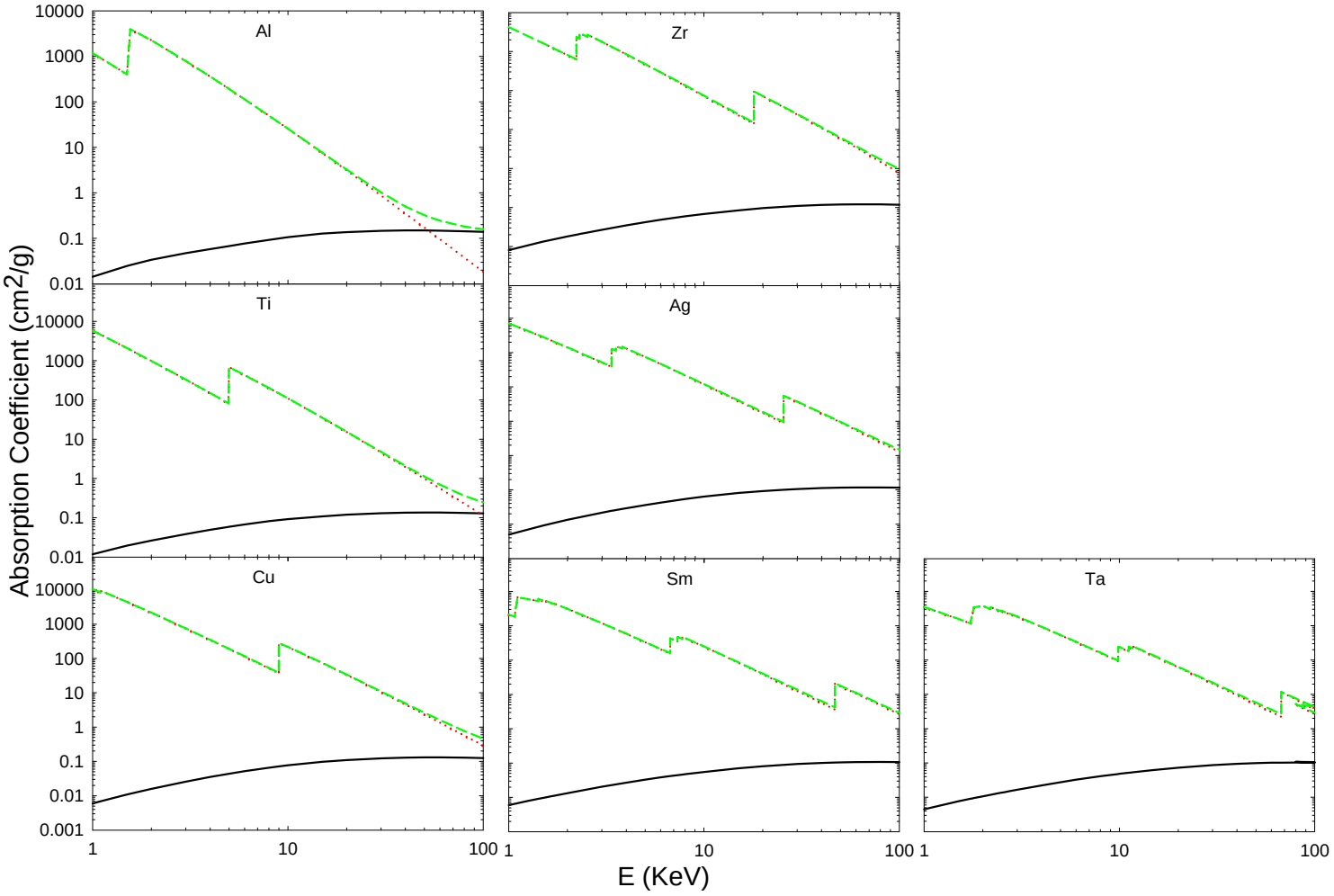

FIG. 35. Target absorption coefficients as a function of photon energy obtained with program XCOM [183] for Compton effect (solid black line), photoelectric effect (dotted red line), and the total (dashed green line).

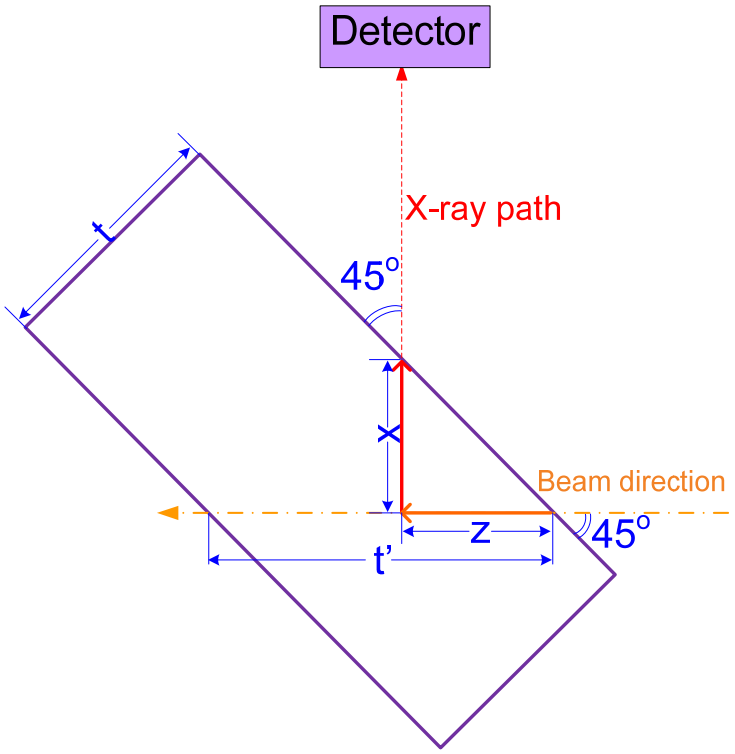

FIG. 36. Schematic view of projectile and x-ray trajectories inside the target (not to scale).

where x is the length of the x-ray path. As mentioned in Chapter III, the target in the present measurements was oriented at 45° with respect to both the beam direction and the spectrometer axis, so that z is equal to x. Making this substitution and integrating over depth from 0 to the effective target thickness t' ($t' = \frac{t}{\cos 45^\circ} = \sqrt{2}t$) yields the

number of photons transmitted through the target toward the detector

$$n = \int_0^{t'} n_0 e^{-\mu x} / t' dx = n_0 \frac{1 - e^{-\mu t'}}{\mu t'}. \quad (64)$$

Therefore, the number of x-rays produced by the beam is given by

$$n_0 = \frac{n \mu t'}{\left(1 - e^{-\mu t'}\right)}. \quad (65)$$

5.3.4. Correction for Al K absorption edge effects

The Al K absorption edge (at 1.559 keV) is just below the average energy of the KαL^6 satellite transitions, which results in significant absorption of the KαL^6 and KαL^7 peaks compared to KαL^0 through KαL^5 peaks. An example of an Al spectrum produced by 20 MeV/amu Xe is shown in Fig. 37, in which only KαL^0 to KαL^5 peaks are present while the KαL^6 and KαL^7 peaks are too small to be noticed.

From Eq. (64), the probability that an x-ray emitted toward the detector escapes out of the target of effective target thickness t' (the photon transmission) is

$$T_x = \frac{\left(1 - e^{-\mu_C t'}\right)}{\mu_C t'}. \quad (66)$$

The convolved Al K x-ray transmission curve (shown in Fig. 38) is given by

$$T_x^c(E') = \int g(E - E') T_x(E) e^{-\frac{(E_0 - E)^2}{2\sigma^2}} dE, \quad (67)$$

where the spectrometer resolution function is given by $g(E - E') = \frac{1}{\sqrt{2\pi}\sigma} e^{-(E-E')^2/2\sigma}$ and σ is the detector resolution.

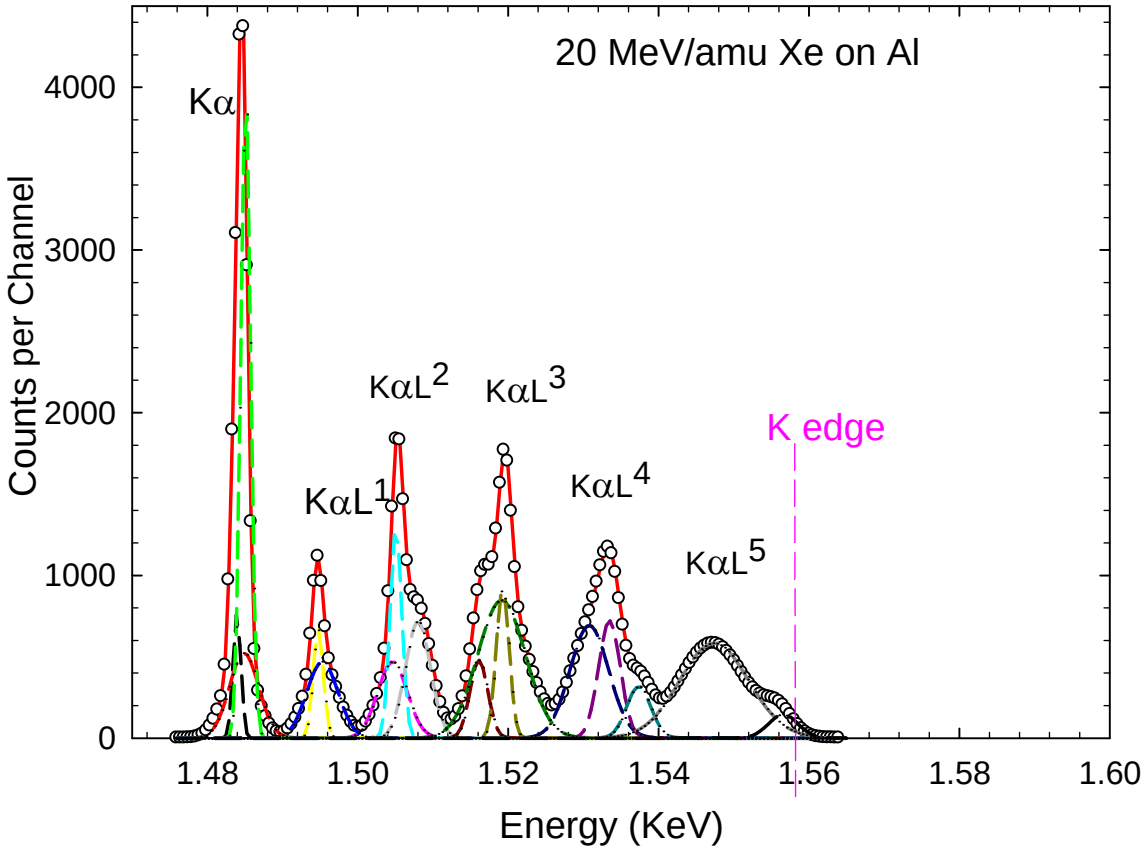

FIG. 37. Al Kα spectrum produced by 20 MeV/amu Xe ions. The K edge is indicated by the vertical pink line. Gaussians used to fit the peaks are shown with dashed lines. Their sum is shown by the solid red curve.

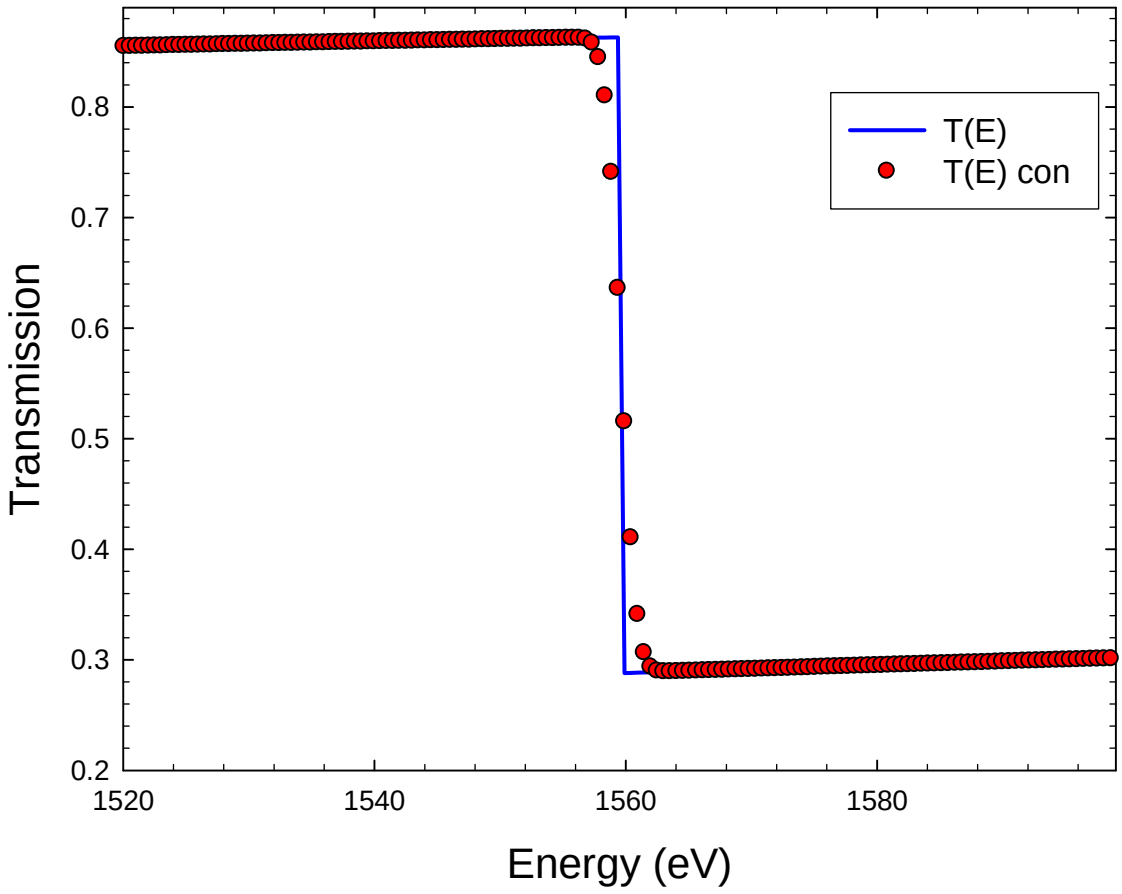

FIG. 38. Blue curve: actual Al x-ray transmission curves in the vicinity of the absorption edge. Solid red circles: convoluted transmission curve.

5.3.5. Fitting procedures

Peaks in the wavelength-dispersive spectra were fitted using Gaussian functions by employing program PeakFit [184]. An example of a fit for Ti Kα x-rays produced by 10 MeV/amu Kr projectiles is shown in Fig. 39, where the open circles represent the measured data points, the red dashed curves represent the Gaussian fits, and the sold green curve represents the overall fit. The overall fits for most spectra were very good except for those involving low-energy projectiles that featured unresolved $K\alpha L^{0+1}$ peaks near the diagram lines.

In fitting the Al spectra, multiple Gaussian functions were used for each satellite peak due to the partially resolved multiplet structure. An example spectrum for Al has been shown previously (Fig. 37).

Since a maximum of eight electrons can occupy the L-shell, there should be up to eight observed Kα satellite peaks. However, the $K\alpha L^0$ overlaps with Kα diagram peaks that originate from secondary processes, while $K\alpha L^8$ peak does not exist because at least one L electron is needed for a Kα transition. Therefore, the number N_0 of collision-produced counts in $K\alpha L^0$ peak and the total number of primary Kα satellite x-rays N_{tot} are not known apriori. From the fit, it was found that the relative intensities of Kα satellite peaks are well represented by a binomial distribution [142] as discussed in Section 4.5. Accordingly, the ratio of the number N_n of collision-produced counts in a $K\alpha L^n$ peak (n = 1 to 7) to N_{tot} is

$$\frac{N_n}{N_{tot}} = \binom{8}{n} p_L^n \left(1 - p_L\right)^{8-n}, \tag{68}$$

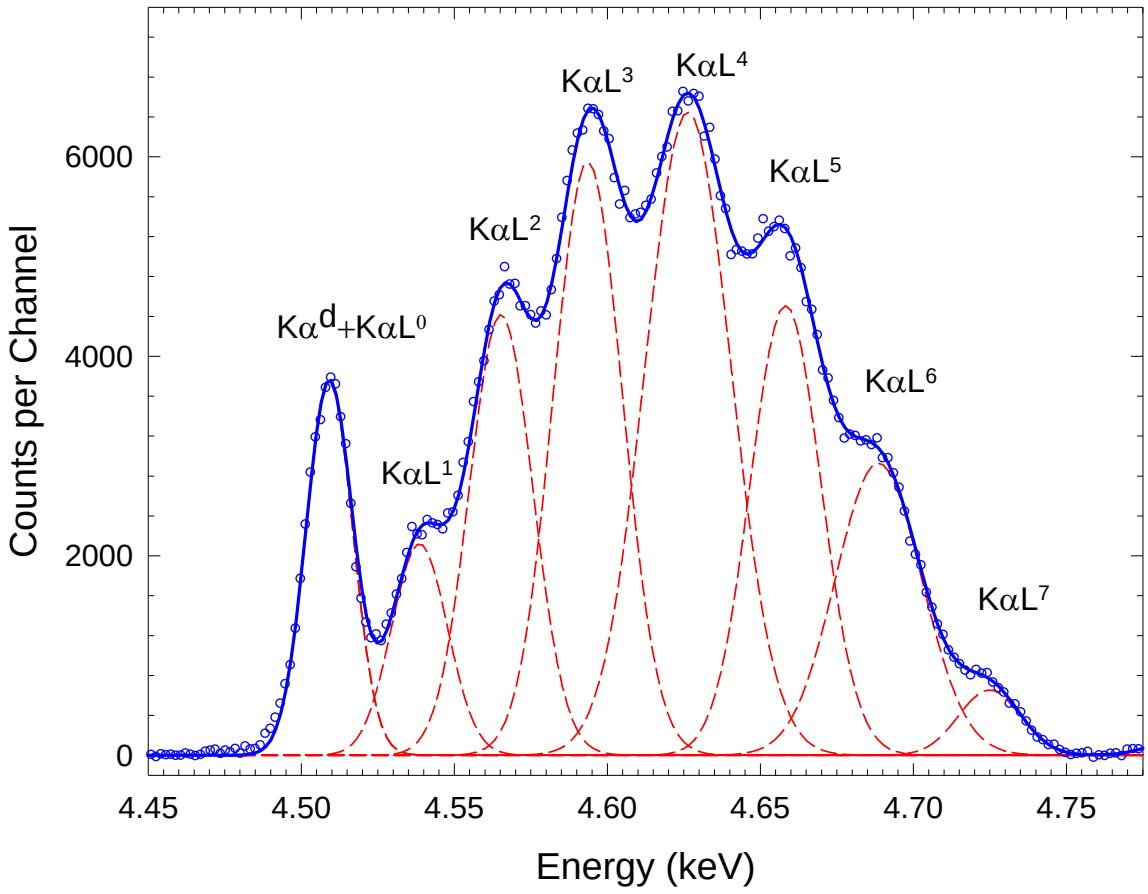

FIG. 39. A typical fit of a wavelength-dispersive target K x-ray spectrum (10 MeV/amu Kr projectiles on Ti target). Components of the spectrum are shown with dashed curves and their sum is shown by the solid curve. The circles represent the measured data points.

where

$$N_{tot} = \sum_{n=0}^{7} N_n \,, \tag{69}$$

in agreement with the independent electron approximation (IEA) (see Ref. [185] and Refs. therein). The parameter p_L is interpreted to be the apparent average L-shell ionization probability per electron in K-shell ionizing collisions. The term "apparent" is applied since vacancy rearrangement processes occurring between the time of collision and the time of x-ray emission may alter the primary distribution of L vacancies. By fitting the experimentally determined intensities of the Kα satellites from n = 1 to 7 with Eq. (68), the values of p_L and N_0 can be determined. The results for Ti are shown in Fig. 40, where the black bars represent the N_n values from independent peak fitting and the red bars represent the values obtained from the fit of the binomial distribution. The largest deviation of the binormial-fit value from the actual peak intensity was about 30% and occurred for the $K\alpha L^1$ peak due to the adjacent peak overlap. The close correspondence between the two intensity distributions lends credence to the method.

The best-fit values of p_L are listed in Tables VII, VIII, and IX. Measurements with additional targets were performed in order to extend the range of p_L values and establish the systematic dependence of p_L on the collision parameters.

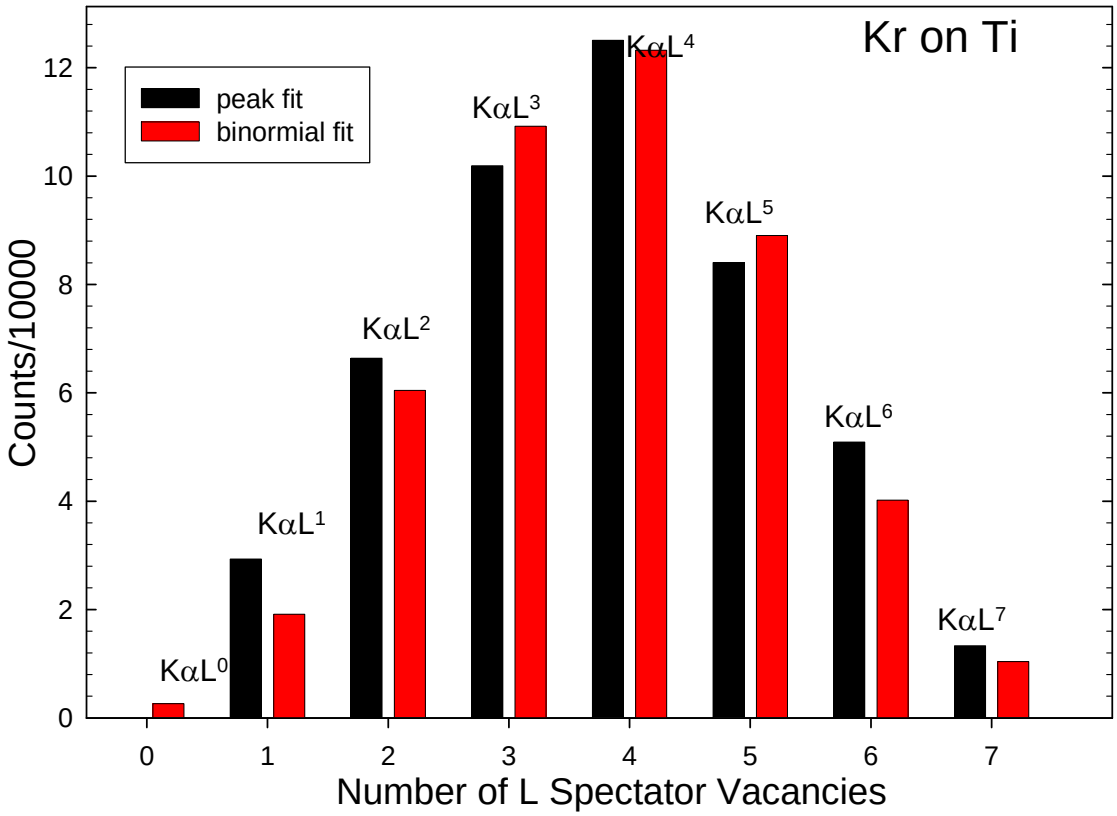

FIG. 40. Comparison of the measured (black bars) and fitted (red bars) Ti Kα satellite peak intensities obtained for 10 MeV/amu Kr on Ti. The fitted intensities follow a binomial distribution, as indicated by Eq. (68).

TABLE VII. Target apparent average L shell ionization probability per electron in K-shell ionizing collisions (p_L) for Ar projectiles at various energies.

Z2	E (MeV/amu)			
	2.5		2.5	
13	0.41	13	0.41	13
22	0.42	22	0.42	22
23	0.40	23	0.40	23
26	0.35	26	0.35	26
27		27		27
29		29		29

TABLE VIII. Target apparent average L shell ionization probability per electron in K-shell ionizing collisions (p_L) for Kr projectiles at various energies.

Z2	E (MeV/amu)			
	4		4	
13	0.41	13	0.41	13
22	0.51	22	0.51	22
23	0.49	23	0.49	23
26	0.47	26	0.47	26
27		27		27
29	0.46	29	0.46	29
32		32		32

TABLE IX. Target apparent average L shell ionization probability per electron in K-shell ionizing collisions (p_L) for Xe projectiles at various energies.

Z2	E (MeV/amu)					
	2.5		2.5		2.5	
13	0.42	13	0.42	13	0.42	
22	0.55	22	0.55	22	0.55	
23		23		23		
26	0.48	26	0.48	26	0.48	
29		29		29		

According to the Geometrical Model, the average L-shell ionization probability per electron at zero impact parameter (p_L) is a universal function of a universal variable, X, defined in Chapter II and repeated here for convenience,

$$X = (4\alpha c / v_1)V[G(V)]^{1/2} Z_1 / n , \quad (70)$$

where α is the fine structure constant given by [†]

$$\alpha = \frac{e^2 / \hbar c}{4\pi\varepsilon_o}, \tag{71}$$

in which e is the elementary charge, $\hbar$ is the reduced Planck's constant, and ε_0 is the permitivity of vacuum. In the present application, Z_1 is taken to be the projectile nuclear charge, and the effective mean values of v_2 are computed from the neutral atom L_3 energies. The form of the function G(V) employed here was developed by Gryzinski [84-86] and is presented in analytical form in Ref. [88]. In Fig. 41, the measured p_L values are shown plotted as a function of X for Z_1 ranging from 6 to 83, v_1 ranging from 9 to 30 a.u., and V ranging from 1.3 to 6.2. It is evident that the p_L values do indeed define a universal function of X, shown by the fitted solid curve, but they systematically deviate from the predictions of the Geometrical Model (shown by the dashed curve) that apply to the distribution of L vacancies at the time of collision. The empirical universal function was determined in a least squares fit [96];

$$p_L = a/[1+(b/X)^c]. \tag{72}$$

The best-fit values of the parameters were found to be a = 0.537 ± 0.006, b = 2.11 ± 0.08, and c = 2.02 ± 0.03. This semiempirical universal function will be used to predict p_L values for the collision systems in this study for which experimental data is not available.

[†] See the NIST website for more details: http://physics.nist.gov/cuu/Constants/alpha.html

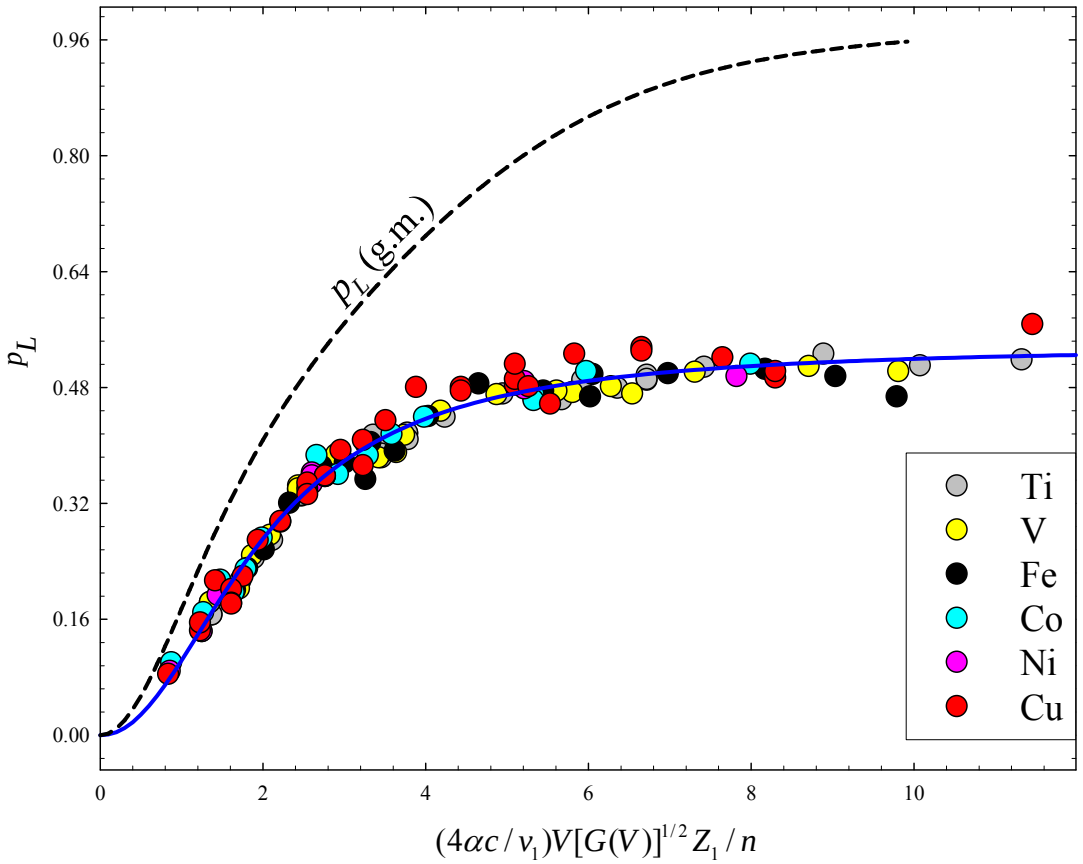

FIG. 41. Apparent average L-vacancy fractions at the time of Kα x-ray emission (p_L), plotted as a function of the universal variable (X) for n = 2. The data points represent the results of measurements involving a variety of solid targets (atomic number Z_2 = 17-32) under bombardment by fast heavy ions (atomic number Z_1 = 6-83) at 2.5-25 MeV/amu, while the solid line represents the best-fit logistic curve. The dashed curve represents the average L-vacancy fractions at the time of collision, predicted by the Geometrical Model [186].

5.3.6. Effect of secondary ionization

As explained in Section 4.5, the Kα diagram peaks contain substantial contributions from secondary ionization processes. As a consequence of this, the KL^0 peak intensity is generally much larger than that predicted by the binomial distribution determined from the peak intensities of the other satellite peaks. This is quite evident in Fig. 39. For low resolution measurements, these secondary contributions overlap the primary x-rays (produced by ion-atom collisions). Therefore, the high resolution measurements were employed to correct for these contributions. Since the primary x-ray distribution is well represented by a binominal distribution, the yield of x rays originating from secondary processes may be determined by comparing the measured intensity with the binomial intensity. For this purpose, it is useful to define the "enhancement" factor R_E as

$$R_E = \frac{\left(N_{K\alpha L^0}\right)_{\exp} - \left(N_{K\alpha L^0}\right)_{bin}}{N_{TOT}}, \tag{73}$$

where $\left(N_{K\alpha L^0}\right)_{\exp}$ is the number of counts in the peak containing the $K\alpha L^0$ satellites and the Kα diagram lines, $\left(N_{K\alpha L^0}\right)_{bin}$ is the number of $K\alpha L^0$ counts calculated using a binomial distribution having a p_L value determined by the intensities of $K\alpha L^1$ through $K\alpha L^7$ (as described in the previous section), and parameter N_{TOT} is the total number of counts in the entire Kα spectrum. The values of R_E for Al, Ti, and Cu targets are listed in Tables X, XI, and XII and are plotted in Fig. 42 as a function of projectile energy. In general, the enhancement factor increase with projectile atomic number except in the

case of Kr-Cu collisions, where they are larger than those for Xe-Cu collisions due to the proximity of Kr K x-ray energy to the Cu K absorption edge.

TABLE X. Enhancement factor (%) for Ar projectiles.

E (MeV/amu)	Al	Ti	Cu
2.5	7.81	1.90	1.50
4	9.10	2.47	2.12
6	9.83	2.93	2.66
10	9.39	3.42	3.32
15	8.00	3.76	3.83
20	7.49	3.98	4.19
25	6.98	4.14	4.46

TABLE XI. Enhancement factor (%) for Kr projectiles.

E (MeV/amu)	Al	Ti	Cu
2.5	15.00	3.05	2.98
4	15.10	4.01	4.34
6	15.10	4.82	5.71
10	15.10	5.68	7.46
15	14.40	6.26	8.81
20	13.30	6.62	9.61
25	11.70	6.89	10.13

TABLE XII. Enhancement factor (%) for Xe projectiles.

E (MeV/amu)	Al	Ti	Cu
2.5	14.10	5.85	2.09
4	18.00	7.32	3.04
6	19.40	8.39	4.35
10	19.40	9.29	5.99
15	17.90	9.64	7.39
20	16.40	9.69	8.28
25	14.40	9.64	8.89

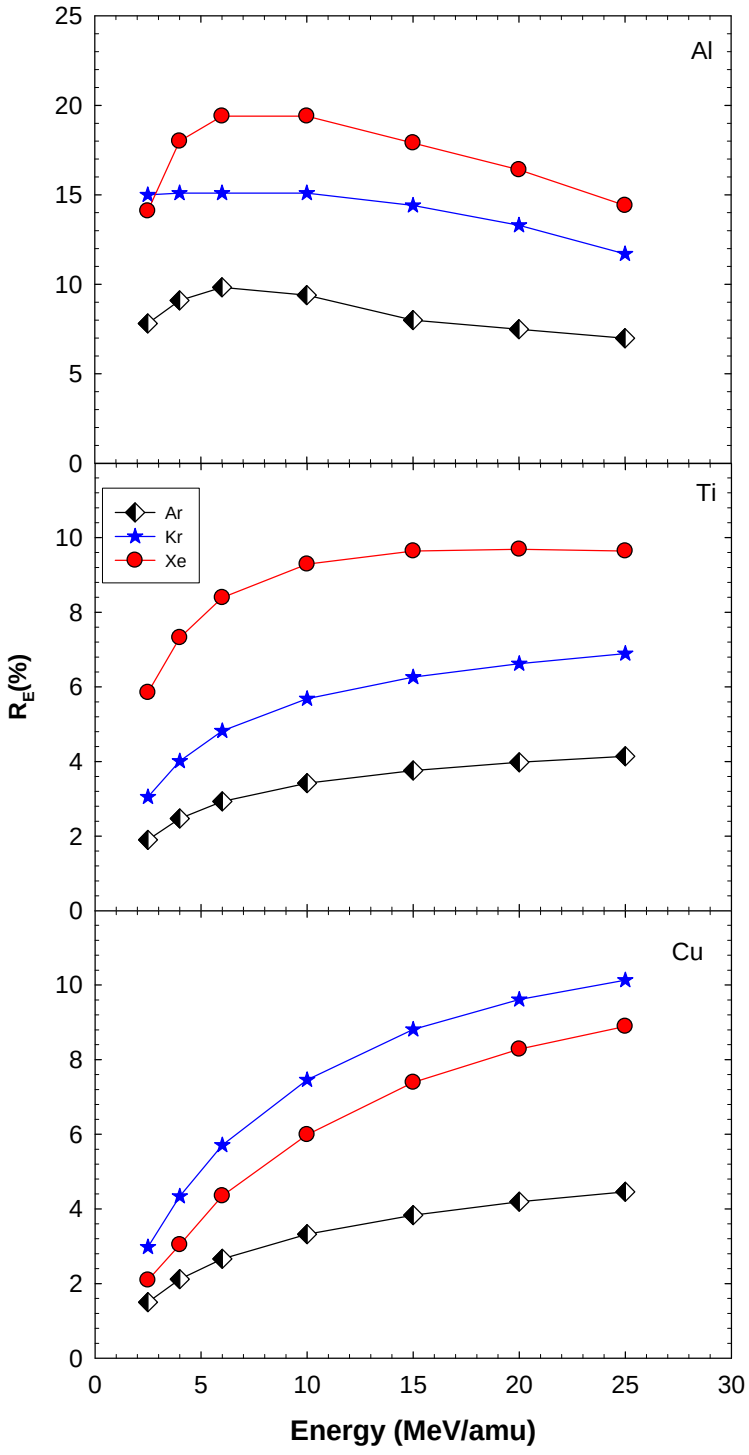

FIG. 42. Comparison of enhancement factors (%) for projectiles of Ar, Kr, and Xe with energies from 2.5 to 25 MeV/amu.

5.3.7. Calculation of fluorescence yields for multiply ionized atoms

As discussed in Sections 4.2. and 4.4.2. , the fluorescence yield of a multiply ionized atom may be significantly different from that of a singly ionized atom. The derivation of multiple vacancy fluorescence yields requires knowledge of the initial vacancy distribution, the sets of possible transitions, and the transition rates.

Using the method developed by Horvat et al. [176] (which was described in Chapter IV), fluorescence yields for multiply ionized Al, Ca, Ti, Mn, and Cu atoms were determined from their high resolution K x-ray spectra and plotted in Fig. 43 as a function of the apparent average L-shell vacancy fraction. At lower values of p_L, the fluorescence yield slowly rises as p_L increases because Auger rates in multiply ionized atoms scale down faster than x-ray rates. At larger values of p_L, the fluorescence yield rapidly decreases as a function of p_L, primarily because the atoms have lost most of their L electrons resulting in the rapid decrease of the Kα transition rates.

The relative change of Kα fluorescence yield, R_ω defined as

$$R_\omega = (\omega_{K\alpha} - \omega_0)/\omega_0 , \tag{74}$$

was calculated for Al, Ca, Ti, Mn, and Cu targets for values of p_L up to 0.5. The values of ω_0 (single vacancy Kα fluorescence yield) were derived from the relation $\omega_0 = \omega_K (1 + R_{\beta/\alpha})^{-1}$ using the total K shell fluorescence yields ω_K given in Table 8 of Hubbell et al. [1] and the theoretical Kβ to Kα intensity ratios $R_{\beta/\alpha}$ of Scofield [187]. The Kα fluorescence yield changes (R_ω) of Al, Ca, Ti, Mn, and Cu are plotted in Fig. 44 as a function of target atomic number for p_L = 0.5, in which the solid curve represents the best fit of the function $y = ae^{-bx}$, with a = 28.44 and b = 0.1734. At Z_2 = 92

(uranium), the extrapolated values of R_ω is negligible (3.6×10^{-6}). At smaller values of p_L, the values of R_ω will be much smaller than those at $p_L = 0.5$. Therefore, it is reasonable to assume that fluorescence yields for the high Z_2 targets Sm and Ta are equal to the single vacancy fluorescence yields in the collision regime studied here.

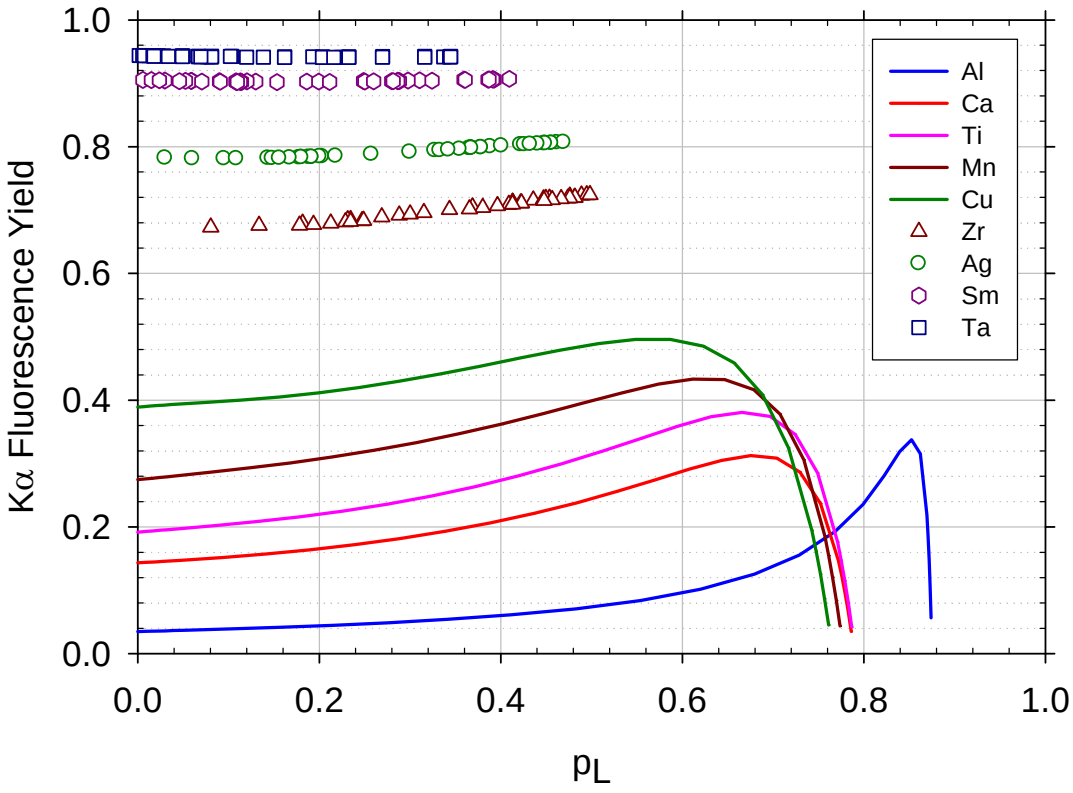

FIG. 43. Comparison of target fluorescence yields as a function of apparent average L-shell vacancy fractions. The solid lines represent the multiple-vacancy fluorescence yields of Al, Ca, Ti, Mn, and Cu targets calculated using the procedure outlined in ref. [176]. The symbols represent the extrapolated fluorescence yields for multiply ionized Zr, Ag, Sm, and Ta (see text for details).

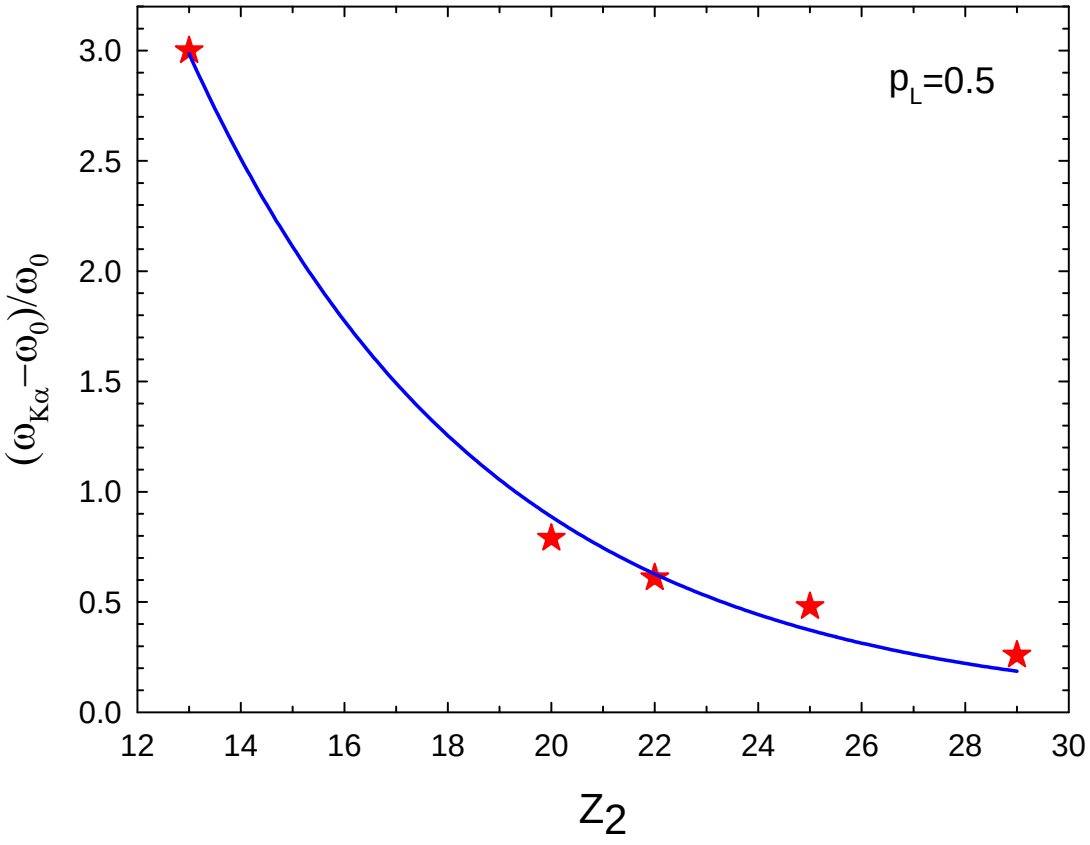

FIG. 44. Fluorescence yield change R_φ (defined in the text) as a function of target atomic number for $p_L = 0.5$.

The multiple-vacancy fluorescence yields were estimated for Zr, Ag, Sm, and Ta as follows. The first step was to calculate the value of the universal variable X for Zr, Ag, Sm, and Ta targets bombarded by Ar, Kr, and Xe projectiles with incident energies from 2.5 to 25 MeV/amu using Eq. (70). The results are listed in Tables XIII, XIV, and XV. For each value of the universal variable, the apparent average L-shell vacancy fraction (p_L) was calculated using the empirical scaling law [Eq.(72)] and these results are listed in Table XVI. For each value of p_L, multiple vacancy fluorescence yields of Al, Ca, Ti, Mn, and Cu were read from Fig. 43. Then each set of fluorescence yields was plotted as a function of Z_2, as shown in Fig. 45. These fluorescence yield curves were fit with the function

$$\omega_{K\alpha} = a/[1+(b/Z_2)^c] \quad (75)$$

and multiple-vacancy fluorescence yields of Zr, Ag, Sm, and Ta were obtained by extrapolation using Eq. (75). The extrapolation curves were required to join with the single vacancy fluorescence yield for uranium, as shown in Fig. 45.

The estimated Kα fluorescence yields for multiply ionized Zr, Ag, Sm, and Ta atoms are listed in Table XVI and plotted as a function of the apparent average L-shell vacancy fraction (p_L) in Fig. 43, using open symbols.

The validity of Eq. (75) was checked by comparing the predicted K shell fluorescence yields (converted from the predicted Kα fluorescence yields using theoretical ratios of Kβ/Kα [187]) at $p_L = 0$ with the single-vacancy fluorescence yields that were based on theoretical calculations and experimental values [1, 161, 170]. The good match between the estimated fluorescence yields at $p_L = 0$ and the single-vacancy fluorescence yields

(see Fig. 46) lends credence to this method.

TABLE XIII. Universal variable X for Zr, Ag, Sm, and Ta targets excited by Ar projectiles with incident energy from 2.5 to 25 MeV/amu.

E(MeV/u)	40	47	62	73
2.5	1.69	1.22	1.21	0.37
4	1.83	1.40	0.79	0.53
6	1.85	1.49	0.90	0.65
10	1.76	1.50	1.02	0.78
15	1.62	1.43	1.06	0.85
20	1.51	1.36	1.06	0.87
25	1.42	1.30	1.04	0.87

TABLE XIV. Universal variable X for Zr, Ag, Sm, and Ta targets excited by Kr projectiles with incident energy from 2.5 to 25 MeV/amu.

E(MeV/u)	40	47	62	73
2.5	3.36	2.43	2.42	0.74
4	3.65	2.80	1.51	1.05
6	3.70	2.98	1.84	1.31
10	3.52	3.00	2.04	1.55
15	3.25	2.86	2.12	1.69
20	3.02	2.72	2.11	1.73
25	2.84	2.59	2.07	1.74

TABLE XV. Universal variable X for Zr, Ag, Sm, and Ta targets excited by Xe projectiles with incident energy from 2.5 to 25 MeV/amu.

E(MeV/u)	40	47	62	73
2.5	5.05	3.65	3.63	1.10
4	5.48	4.20	2.26	1.57
6	5.55	4.47	2.76	1.97
10	5.28	4.50	3.06	2.33
15	4.87	4.30	3.18	2.53
20	4.53	4.08	3.17	2.60
25	4.27	3.89	3.11	2.61

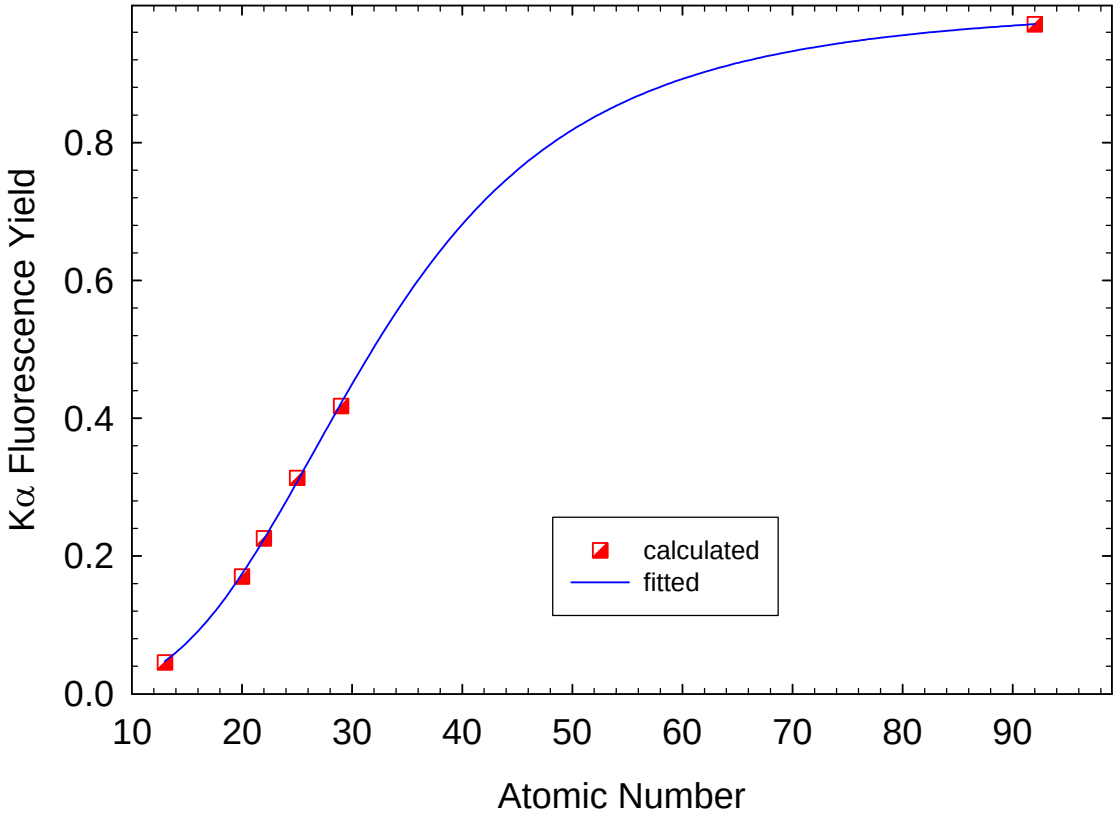

FIG. 45. Kα fluorescence yields of multiply ionized Al, Ca, Ti, Mn, and Cu atoms with $p_L = 0.229$ as a function of the atomic number. The data point at $Z_2 = 92$ is the single vacancy fluorescence yield of uranium. The solid blue curve represents a fit to the data points using Eq. (75) with a = 1.00, b = 31.87, and c = 3.34.

TABLE XVI. Apparent average L-shell vacancy fractions and the estimated Kα fluorescence yields of multiply ionized Zr, Ag, Sm, and Ta atoms.

	Zr		Ag			Sm		Ta
	p_L	ω_K	p_L	ω_K		p_L	ω_K	p_L
	0.229	0.562	0.148	0.646	Ar	0.229	0.562	0.148
	0.247	0.562	0.178	0.645		0.247	0.562	0.178
	0.249	0.562	0.192	0.645		0.249	0.562	0.192
Ar	0.235	0.562	0.192	0.645		0.235	0.562	0.192
	0.213	0.562	0.180	0.645		0.213	0.562	0.180
	0.194	0.562	0.167	0.645		0.194	0.562	0.167
	0.178	0.562	0.156	0.645		0.178	0.562	0.156
	0.409	0.562	0.333	0.646	Kr	0.409	0.562	0.333
	0.422	0.562	0.365	0.645		0.422	0.562	0.365
	0.423	0.562	0.378	0.644		0.423	0.562	0.378
Kr	0.413	0.563	0.378	0.644		0.413	0.563	0.378
	0.396	0.565	0.367	0.644		0.396	0.565	0.367
	0.380	0.566	0.355	0.644		0.380	0.566	0.355
	0.366	0.567	0.342	0.644		0.366	0.567	0.342
	0.474	0.562	0.426	0.645	Xe	0.474	0.562	0.426
	0.481	0.562	0.447	0.645		0.481	0.562	0.447
	0.482	0.565	0.456	0.644		0.482	0.565	0.456
Xe	0.476	0.569	0.456	0.644		0.476	0.569	0.456
	0.467	0.573	0.449	0.645		0.467	0.573	0.449
	0.457	0.575	0.441	0.646		0.457	0.575	0.441
	0.448	0.577	0.432	0.646		0.448	0.577	0.432

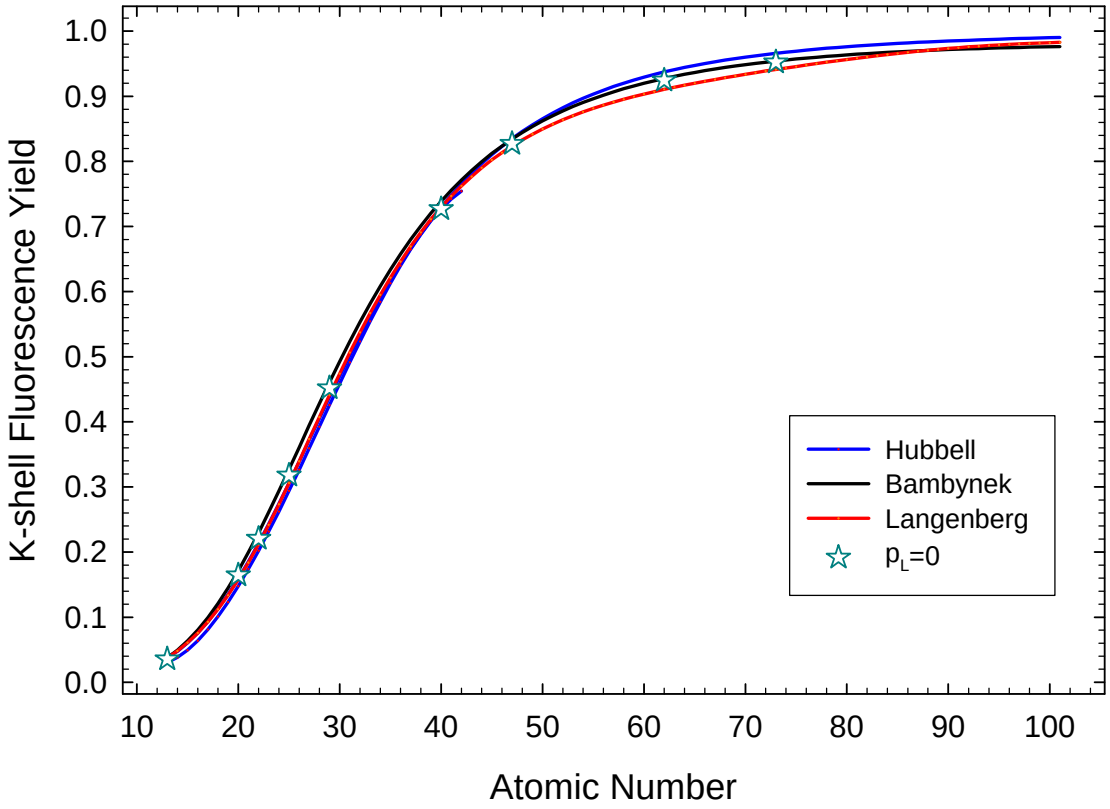

FIG. 46. Comparison of the estimated K shell fluorescence yields at $p_L = 0$ with single-vacancy fluorescence yields. Blue line: Hubble [1]; black line: Bambynek [161]; red line: Langenberg [170].

5.4. Energy-dispersive spectra

As mentioned in Chapter IV, the Kα diagram line and the Kα satellite peaks are not resolved from each other in the energy-dispersive spectra, while the Kα hypersatellite peaks appear as a shoulder on the high energy side of the Kα peak. Additionally, the Kβ peaks are well resolved from the Kα peaks only for targets with atomic number 29 (Cu) and above. Although the Ti Kβ peak is not well resolved from the Ti Kα peak, its intensity could be determined accurately using the PeakFit program. Typical x-ray spectra obtained in the present study are shown in Figs. 47, 48 and 49. The dashed lines show the energies of the Kα and Kβ diagram lines. Multiple vacancies in the L and M shells cause the K x-ray peaks to broaden and shift to higher energies. The effect becomes more pronounced as the projectile atomic number increases (see Fig. 47). Fig. 48 also shows that the relative intensity of the Kα hypersatellites increases with increasing projectile energy, because the higher the projectile energy, the larger the probability that two K electrons could be ejected out. Other peaks visible in these figures are due to projectile x-rays, target L x-rays, and pulse pileup. As mentioned in Chapter III, Ag reference foils were placed behind the Sm and Ta targets and hence strong Ag K x-ray peaks always appear in the Sm and Ta spectra (see Fig. 49).

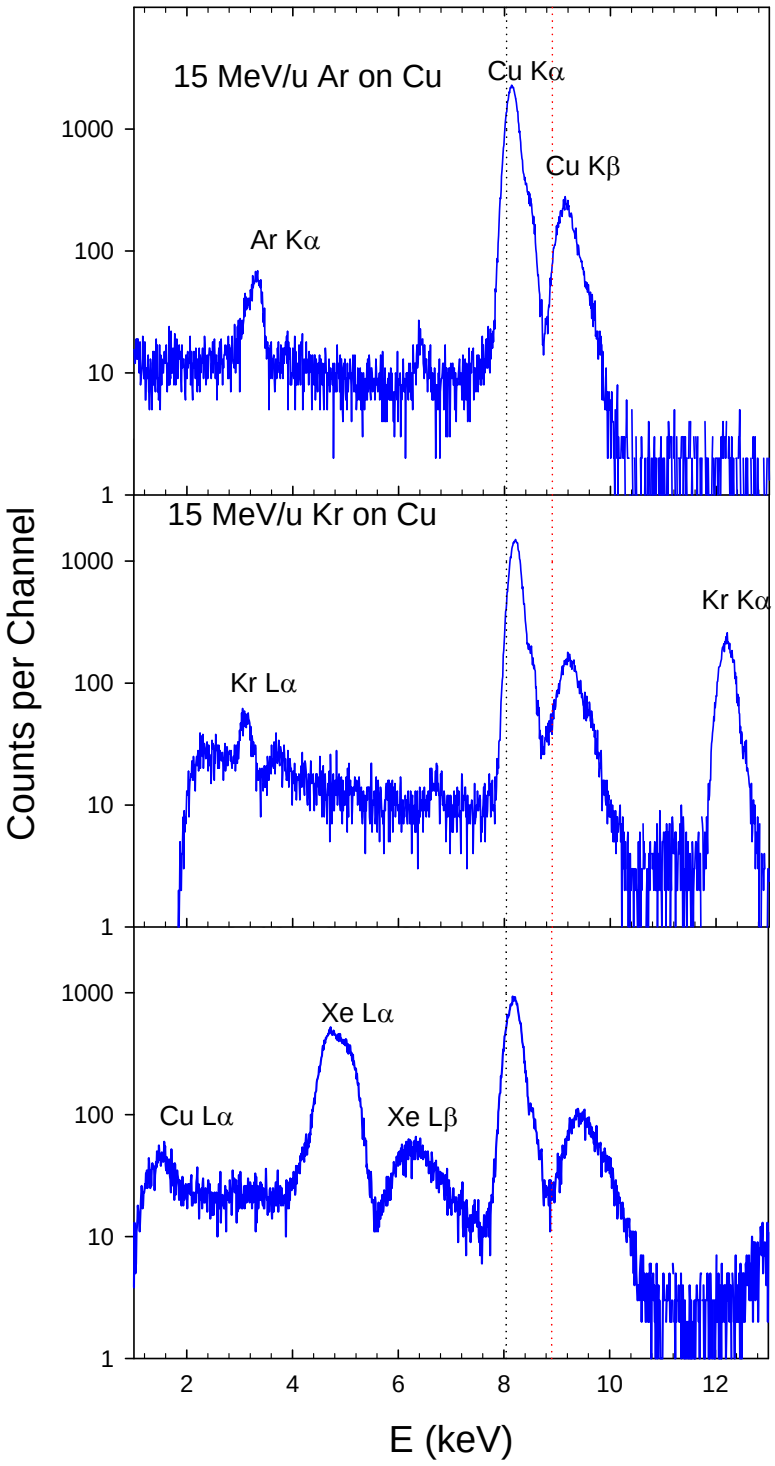

FIG. 47. Typical Cu K x-ray spectra generated in collisions with Ar, Kr, and Xe projectiles at 15 MeV/amu.

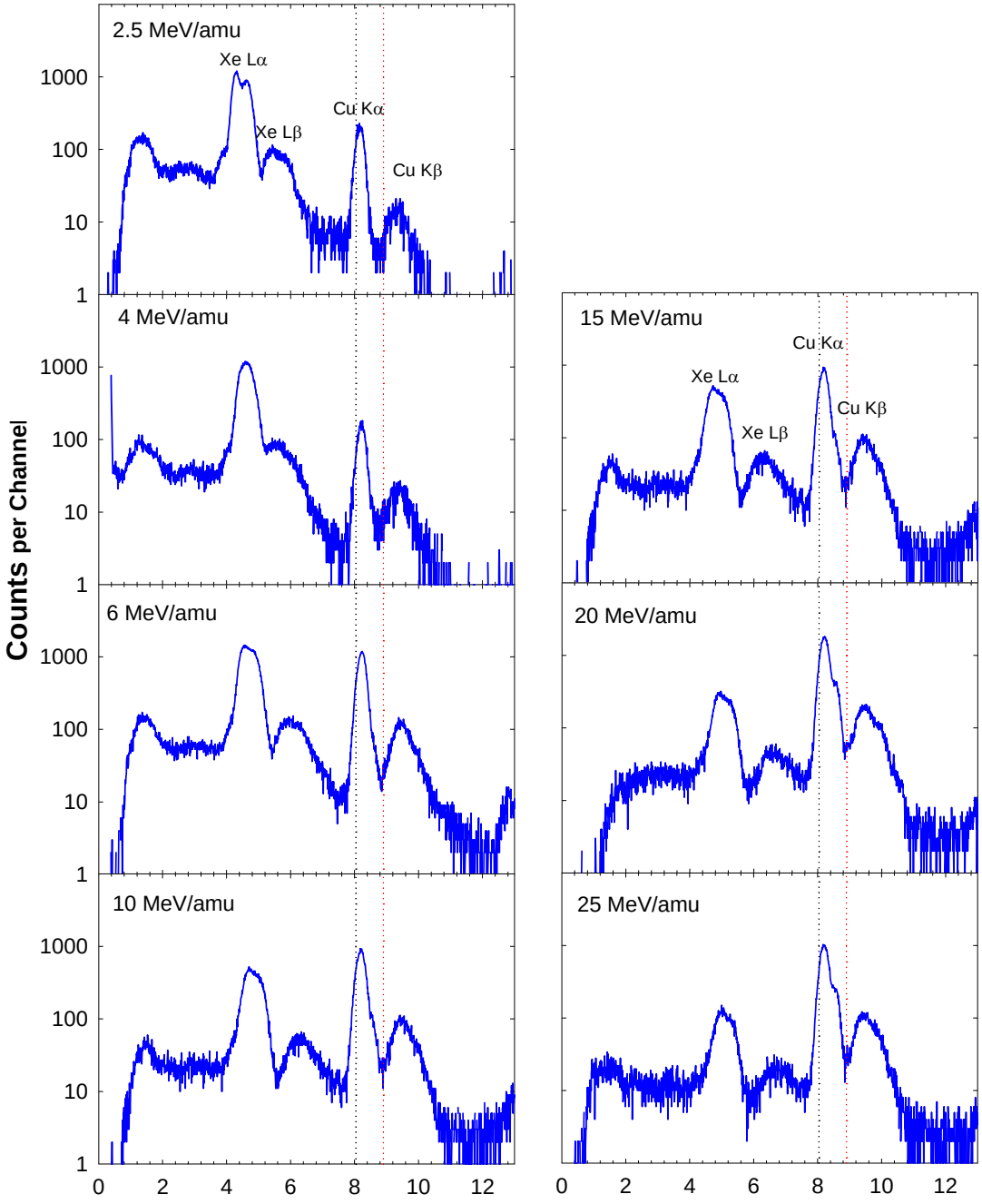

FIG. 48. Typical Cu x-ray spectra obtained with Xe projectiles at different energies.

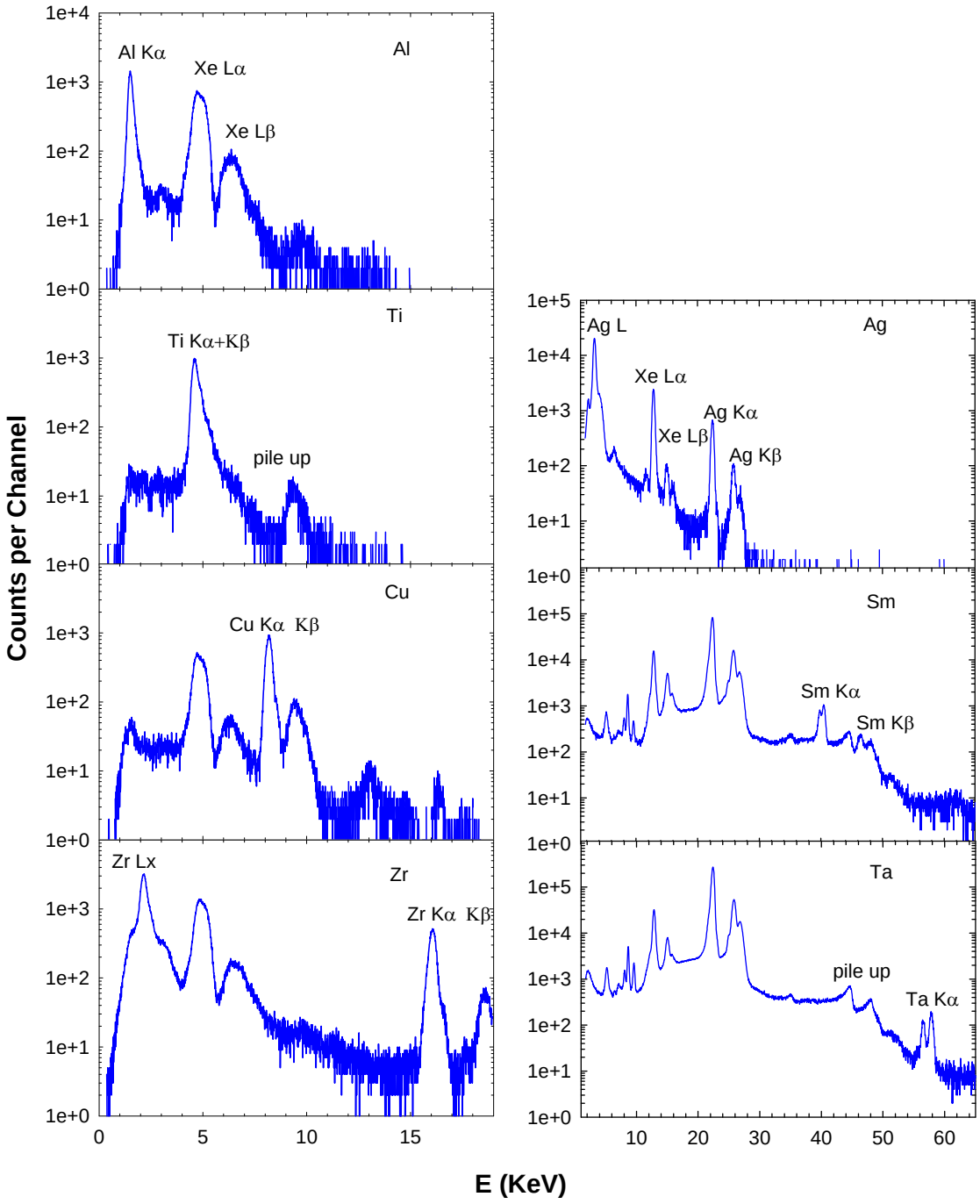

FIG. 49. Target x-ray spectra excited by 15 MeV/amu Xe projectiles. The strong Ag peaks in Sm and Ta spectra were due to the Ag reference foils positioned behind the targets (see section 3.2.3.).

5.4.1. Cross section calculations

The detected number of Kα x-rays, N_K , can be expressed as

$$N_{K\alpha} = N_p \eta T_x \Omega \varepsilon_{K\alpha} \sigma_{K\alpha}, \tag{76}$$

where N_p is the number of incident projectiles, η is the number of target atoms per cm^2, Ω is the detector solid angle fraction, ε_K is the detector efficiency at the corresponding x-ray energy, $\sigma_{K\alpha}$ is the target Kα x-ray production cross section, and T_x is photon transmission probability given by Eq. (66). By rearranging Eq. (76), the target Kα x-ray production cross section is given by the following expression

$$\sigma_{K\alpha} = \frac{N_{K\alpha}}{N_p \eta T_x \Omega \varepsilon_{K\alpha}}. \tag{77}$$

Eq. (77) indicates that the Kα x-ray production cross section can be determined by measuring the number of Kα x-rays and the number of projectiles if the x-ray transmission probability, target thickness, and detector efficiency are known.

Finally, the K vacancy production cross section can be determined by dividing the Kα x-ray production cross section with the average Kα fluorescence yield,

$$\sigma_K = \sigma_{K\alpha} / \omega_{K\alpha}. \tag{78}$$

In the current work, considerable care was exercised in determining the number of the detected target Kα x-rays. Background, absorption, peak overlap, and absorption edge effects were addressed just as in the analysis of the wavelength-dispersive spectra. The overlap of projectile L x-rays with target Kα x-rays, Al K edge absorption, and secondary ionization will be discussed in the following sections.

5.4.2. Correction for absorption at the Al K edge

The corrections for absorption at the Al K edge were similar to those applied to the wavelength-dispersive spectra, except that the transmission functions were convolved with broader Gaussian resolution functions. The result is shown in Fig. 50. A comparison of the corrected and uncorrected Al K x-ray spectra is shown in Fig. 51 for 4 MeV/amu Xe projectiles. The same method was applied to the Ti spectra because of the close proximity of the K absorption edge to the Ti Kα hypersatellites.

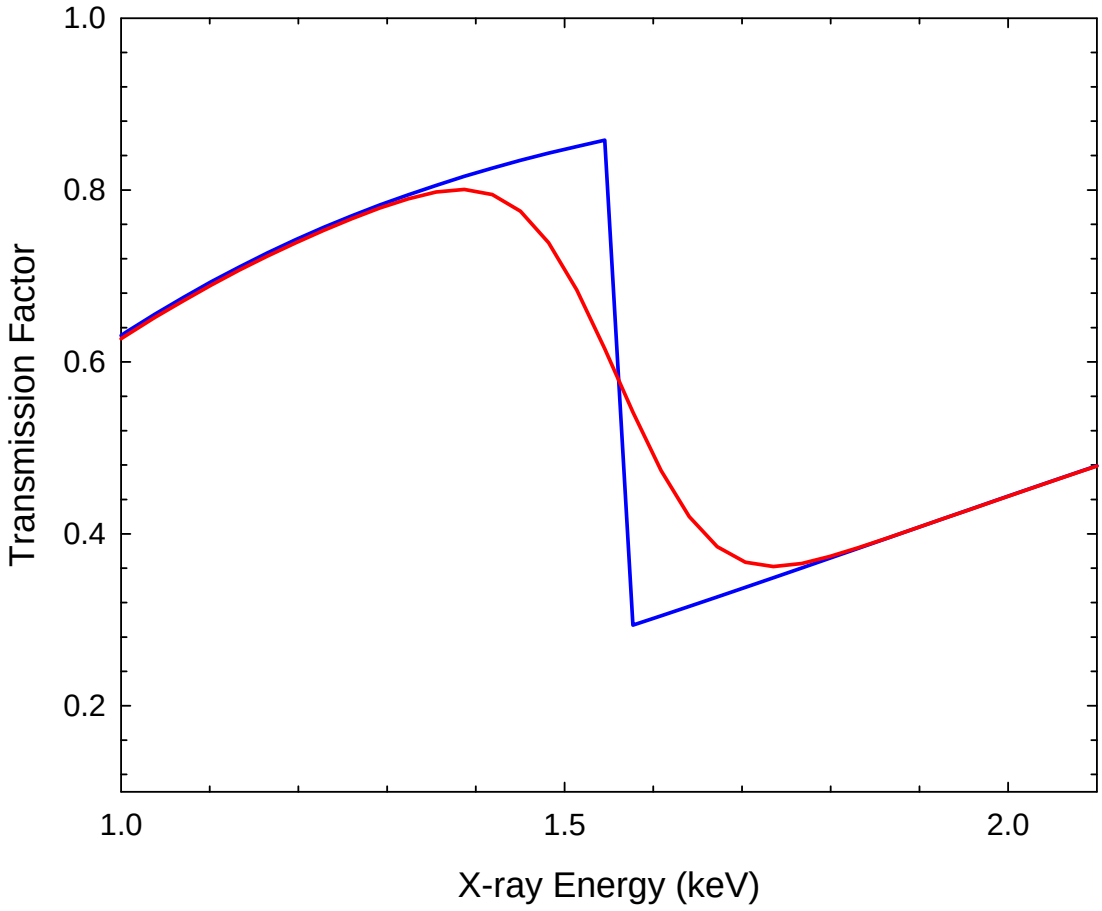

FIG. 50. Comparison of the actual (blue) and convolved (red) transmission function for Al K x-rays (energy-dispersive measurements).

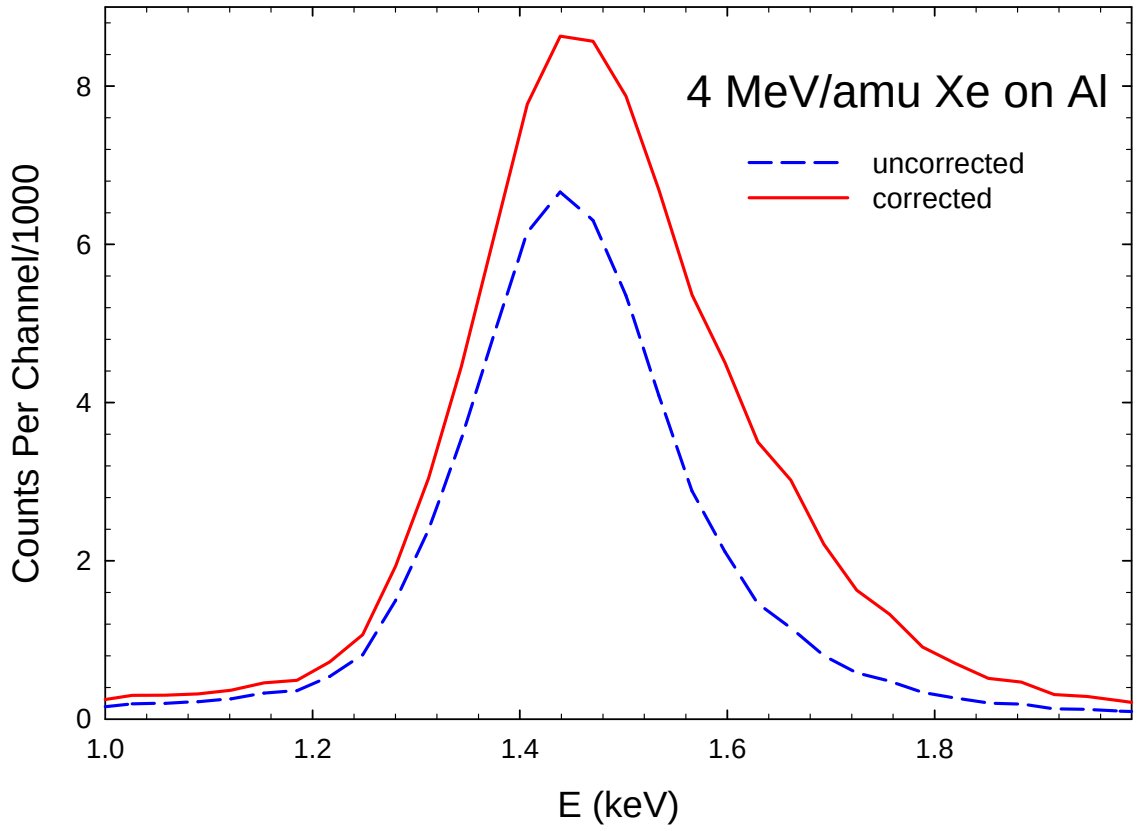

FIG. 51. Comparison of the Al K x-ray spectra without (blue) and with (red) correction for absorption in the measurements involving 4 MeV/amu Xe projectiles.

5.4.3. Separating contributions from overlapped peaks

The K x-ray energies of Al, Ti, and Cu are compared with K and L x-ray energies of Kr and Xe in Table XVII. The proximity of Al K x-ray energies (1.49 and 1.56 keV) to the Kr Lα and Lβ x-ray energies (1.59 and 1.64 keV) resulted in the overlap of Kr L x-ray and Al K x-ray peaks. Also, Ti K x-ray peaks (4.50 to 4.93 keV) overlap with the Xe L x-ray peaks (4.11 keV – 5.31 keV). Fig. 52 (a) shows the K x-ray spectra of Al (red) and Ti (blue) bombarded by 2.5 MeV/amu Kr projectiles. It is obvious that the Kr L x-ray peak overlaps the high-energy side of the Al K x-ray peak. The overlap of L x-rays from 2.5 MeV/amu Xe projectiles with K x-rays from the Ti target is shown in Fig. 52 (b). Contributions from projectile x-rays must be subtracted in the analysis of the spectra for these two collision systems. The contribution of Xe L x-rays was subtracted from the Ti K x-ray peak as follows. First, Xe projectile L x-ray production cross sections per channel were determined from the spectra for Xe on Al ($Z_2 = 13$) and Xe on Cu ($Z_2 = 29$) over the energy range from 3 to 7 keV using the following formula

$$\sigma_L(Z_2) = \frac{N_L}{N_p \eta T (\Omega\varepsilon)_L}, \tag{79}$$

where N_L is the number of detected Xe L x-rays per channel, N_p is the number of detected projectiles, $(\Omega\varepsilon)_L$ is the probability of L x-ray detection (from the efficiency curve in Fig. 16), η is the number of target in atoms per unit area, and T is the Xe L x-ray transmission probability. The Xe L x-ray production cross sections per channel for collisions with Cu and Al targets are shown in Fig. 53. Apparently, the Xe L x-ray production cross section does not depend strongly on the target atomic number.

Table XVII. K and L x-ray energies of Al, Ti, Kr, and Xe [139] in keV.

	$K\alpha_1$	$K\alpha_2$	$K\beta_1$	$L\alpha$	$L\beta$	$L\gamma$
Al	1.49	1.49	1.56			
Ti	4.51	4.50	4.93			
Kr	12.65	12.60	14.11	1.59	1.64	1.91[a]
Xe	29.78	29.46	33.62	4.11	4.42	5.31

[a] theoretical value for neutral atoms

Consequently, Xe L x-ray production cross sections per channel for the Ti target were linearly interpolated between those for Al and Cu. Using these interpolated cross sections, the contribution of Xe L x-rays to the spectrum of Ti K x-rays could be calculated. The calculated Xe L x-ray contribution (red) to the spectrum of Ti K x-rays, produced by 2.5 MeV/amu Xe ions, is shown in Fig. 54 along with the uncorrected Ti K x-ray spectrum.

A similar procedure was employed to subtract the contributions of Kr projectile L x rays from the spectra of Al K x rays, except that the Z_2 dependence was established based on the spectra obtained with Ti and Cu targets.

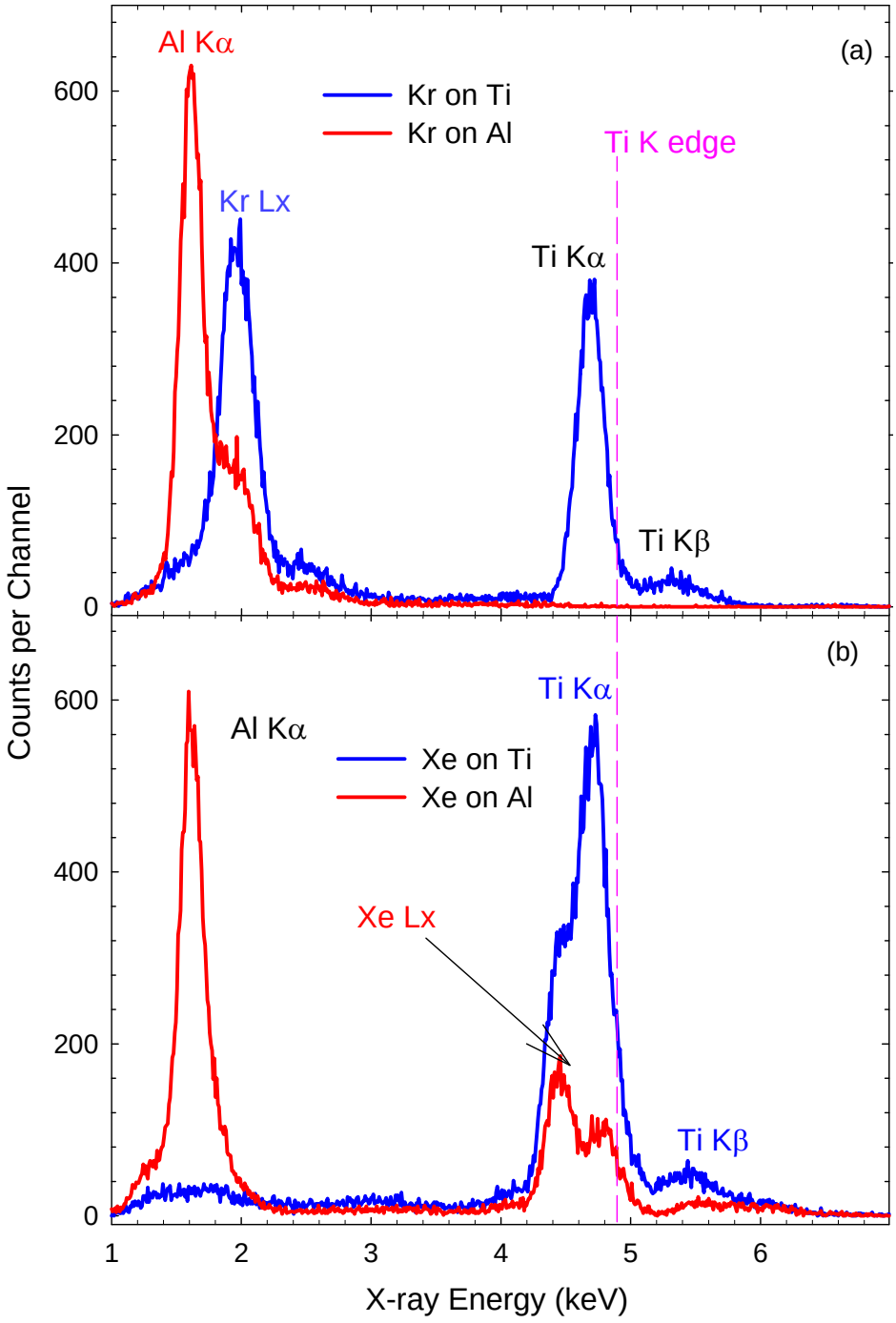

FIG. 52. Examples of the overlap of projectile L x-ray peaks and target K x-ray peaks for (a) Kr on Al and (b) Xe on Ti, both at 2.5 MeV/amu.

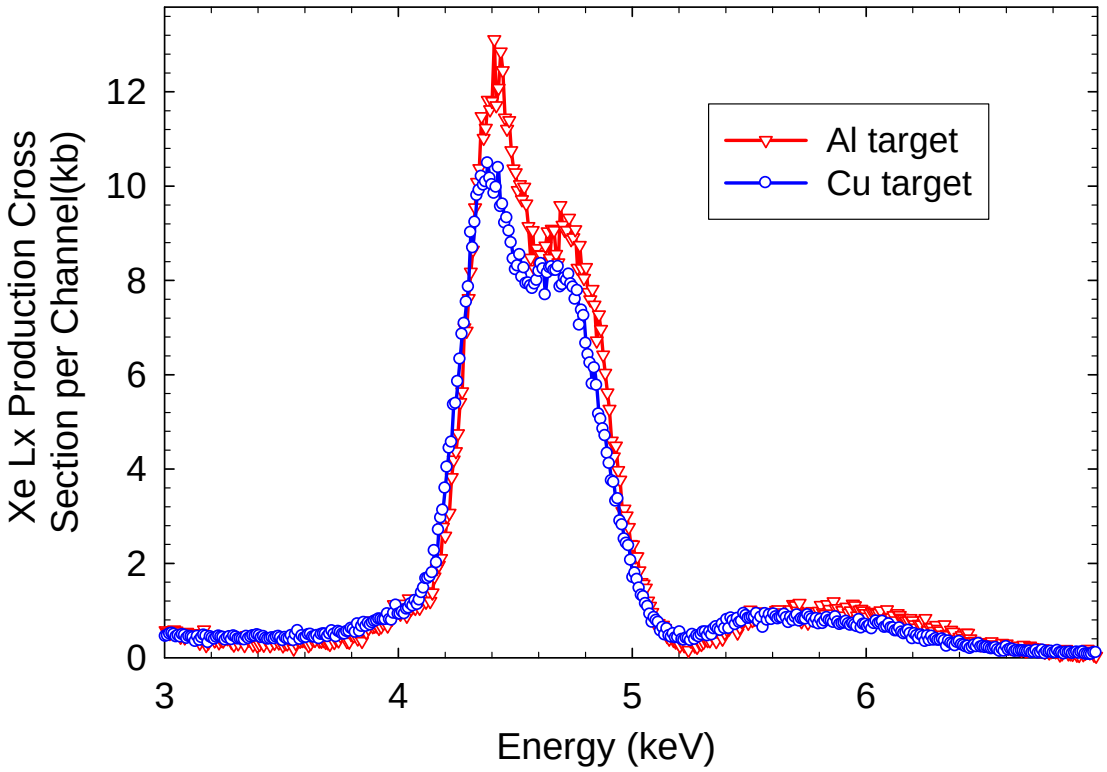

FIG. 53. Comparison of the Xe L x-ray production cross sections per channel for 2.5 MeV/amu Xe projectiles in Al (red) and Cu (blue) targets.

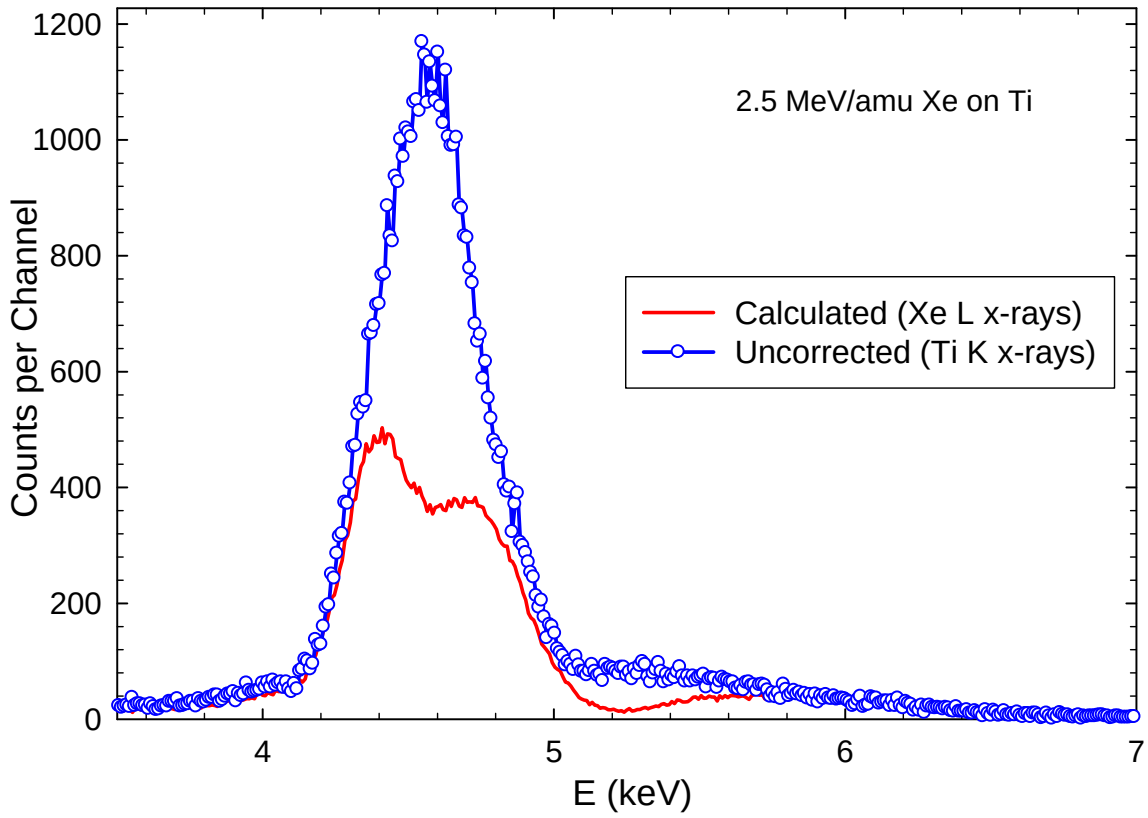

FIG. 54. Comparison of the calculated Xe L x-ray spectrum with the uncorrected Ti K x-ray spectrum.

5.4.4. Corrections for ionization by secondary processes

As described in Chapter IV, $K\alpha L^0$ peaks appear enhanced relative to the expectations based on a binomial distribution of satellite peak intensities. This is due to target K-vacancy production resulting from photoionization by projectile x-rays, ionization by secondary electrons ejected in ion-atom collisions, and photoionization by target x-rays with energies above the K binding energy of the neutral target atom. These secondary processes predominantly produce single vacancy states that decay by the emission of diagram lines and contribute to the counts in the $K\alpha L^0$ diagram peaks. The contributions from secondary processes should be separated from those due to primary K shell vacancy production in ion-atom collisions. Different methods were developed for different targets. For Al, Ti, and Cu targets, the correction was based on the R_E values determined from the wavelength-dispersive measurements. For Zr and Ag targets, Kβ diagram line intensities and theoretical values of Kβ to Kα intensity ratios were utilized to correct for secondary ionization. In the case of Sm and Ta, K x-ray contributions from secondary processes were deemed to be negligible because all projectile x-rays are below the target K binding energies and the binary encounter electron energies are either below (Ta) or slightly above (Sm) the target K binding energies (67.4 and 46.8 keV, respectively). Specifically, it is well known that binary-encounter electrons are produced with energies peaking around 4mE/M at zero degrees, where m is the mass of the electron, and M and E are the mass and energy of the projectile, respectively [20]. For 25 MeV/amu projectiles, the binary encounter peak energy is 55 keV, which is below the Ta K binding energy and slightly above the Sm K binding energy.

5.4.4.1. Secondary K-shell ionization in Al

The total number of detected Al K x-rays is

$$I_{tot} = I_{\alpha L} + I_{\alpha U} + I_{hs} + I_{\beta}, \tag{80}$$

where $I_{\alpha L}$ represents the number of detected Kα x-rays below the K edge, $I_{\alpha U}$ represents the number of detected Kα satellite x-rays above the K edge, I_{hs} represents the number of detected hypersatellite x-rays, and I_{β} represents the number of detected Kβ x-rays. Then the number of primary K x-rays is

$$I_{pri} = I_{tot} - I_s, \tag{81}$$

where I_s is the number of K x-rays from secondary processes. R_E [Eq. (73)], as determined from the wavelength-dispersive spectra can be expressed as $R_E = I_s / I_{\alpha L}$. Defining $R_{\alpha L} = I_{\alpha L} / I_{tot}$, the number of secondary x-rays can be expressed as

$$I_s = I_{\alpha L} R_E = I_{tot} R_{\alpha L} R_E. \tag{82}$$

Thus the number of primary x rays is given by

$$I_{pri} = I_{tot}(1 - R_{\alpha L} R_E) = I_{tot}(1 - R_s), \tag{83}$$

where $R_s = R_{\alpha L} R_E$. Both $R_{\alpha L}$ and R_E were determined from the wavelength-dispersive measurements.

5.4.4.2. Secondary K-shell ionization in Ti and Cu

The method used to correct for secondary K-shell ionization in Ti and Cu targets was similar to that described above for the Al target, but it was simplified by the fact that the Ti K edge lies above the Kα satellite and hypersatellite x-ray energies and the Kβ peak

can be accurately separated from the Kα peak in the spectrum. Utilizing the wavelength-dispersive measurements to determine the ratios R_E ($R_E = I_s / I_\alpha$) and R_{hs} ($R_{hs} = I_{hs} / I_\alpha$), the secondary ionization contribution could be determined as follows. Since the total number of Kα x-rays is

$$I_{tot} = I_\alpha + I_{hs} = I_\alpha + I_\alpha R_{hs} = I_\alpha (1 + R_{hs}) , \tag{84}$$

and

$$I_s / I_{tot} = I_s / [I_\alpha (1 + R_{hs})] = R_E / (1 + R_{hs}) = R_s , \tag{85}$$

the number of detected primary x-rays is given by [from Eq. (81) and (85)]

$$I_{pri} = I_{tot} (1 - R_s) . \tag{86}$$

5.4.4.3. Contribution from secondary ionization in Ag K x-ray spectra

As mentioned in Chapter III, the curved crystal spectrometer employed in this work was not capable of measuring high-resolution K x-ray spectra for elements above Ge (Z_2 = 32). However, it was found that the enhanced $K\beta_1'$ peaks in the energy-dispersive spectra of Zr and Ag were sufficiently displaced from the Kβ satellites that they could be resolved by peak fitting. Therefore, by measuring the $K\beta_1'$ x-ray diagram peak intensity and employing theoretical single vacancy intensity ratios from Scofield et al. [187], the values of R_s [Eq. (85)] could be determined.

Spectra of the Kβ x-ray region of Ag, recorded with the Si(Li) detector using 25 MeV/amu projectiles are shown in Fig. 55. In the spectrum excited by Ar ions, there is no indication of any significant contribution from the Kβ diagram lines. This is not surprising, since Ar K x-rays cannot photoionize the Ag K shell and the yield of

secondary electrons capable of ionizing the Ag K shell is expected to be low. However, the spectra excited by Kr and Xe ions both contain enhanced $K\beta_1$ peaks due to secondary ionization processes. It is evident that the intensity of the Kβ diagram line and the centroid of the satellite peak distribution are increasing with projectile atomic number. The shifted centroid of the satellite peak distribution is caused by multiple ionization. For Ar projectiles, secondary K-shell ionization was low enough to be negligible. The strong Kβ satellite peaks also indicate that the enhancement is relatively small (photoionization produces only diagram lines in most case).

The number of counts in the $K\beta_1^{'}$ peak ($I_{\beta 1}$) and the ratio $R_{\beta_1^{'}} = I_{\beta_1^{'}} / I_\alpha$ were determined by fitting Gaussian functions to the Zr and Ag spectra with program PeakFit. The number of counts in the Kα peak produced by secondary processes (I_s) was calculated using the relation

$$I_s = I_\alpha R_{\beta_1^{'}} S_{\alpha/\beta_1^{'}}, \tag{87}$$

where $S_{\alpha/\beta_1^{'}}$ is the Kα to $K\beta_1^{'}$ intensity ratio for atoms with a single K vacancy. This latter quantity was computed from the ratio of theoretical K vacancy radiative decay rates given by Scofield [187] as follows,

$$S_{\alpha/\beta_1^{'}} = \frac{\lambda_\alpha}{\lambda_{\beta_1^{'}}} = \frac{\lambda_{\alpha_1} + \lambda_{\alpha_2}}{\lambda_{\beta_1^{'}}} = \frac{\lambda_{\alpha_1}\left(1 + S_{\alpha_2/\alpha_1}\right)}{\lambda_{\beta_1^{'}}} = S_{\alpha_1/\beta_1^{'}}\left(1 + S_{\alpha_2/\alpha_1}\right). \tag{88}$$

Then the number of primary Kα x rays produced in ion-atom collisions is

$$I_{pri} = I_\alpha (1 - R_S), \tag{89}$$

where

$$R_s = R_{\beta_1^{'}} S_{\alpha_1/\beta_1^{'}} (1 + S_{\alpha_2/\alpha_1}). \tag{90}$$

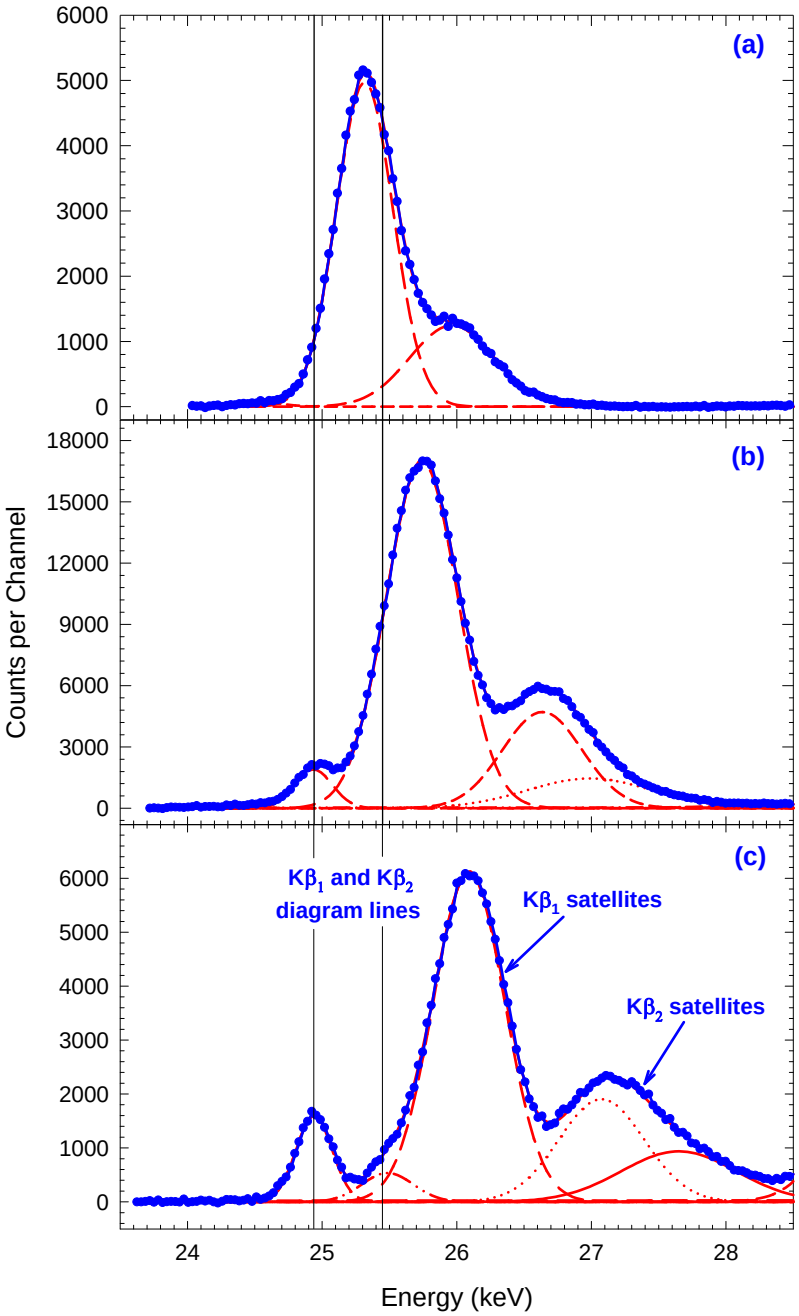

FIG. 55. Spectra of Ag Kβ x-rays produced by 25 MeV/amu Ar, Kr, and Xe projectiles. The vertical pink line indicates the position of the K'_{β} diagram peak.

5.5. Results

After all the corrections were applied, the target K x-ray production cross sections and the K-vacancy production cross sections were determined using Eqs (77) and (78). The Kα x-ray production cross sections are listed in Table XVIII for Al, Ti, Cu, and Zr targets and in Table XIX for Ag, Sm, and Ta targets.

The K vacancy production cross sections are listed in Tables XX, XXI, and XXII for Ar, Kr, and Xe projectiles, respectively. The ratios of multiple-vacancy fluorescence yields to single-vacancy fluorescence yields for Kα transitions as well as the enhancement factor (R_s) are also listed in these tables.

The average experimental uncertainties of the K vacancy production cross sections are listed in Table XXIII.

TABLE XVIII. Measured Kα x-ray production cross sections (Mb) for Al, Ti, Cu, and Zr targets.

	E(MeV/amu)	Ar	Kr	Xe
Al	2.5	2.154E-01	5.200E-01	8.423E-01
	4	3.162E-01	8.277E-01	1.242E+00
	6	2.697E-01	8.546E-01	1.487E+00
	10	2.625E-01	8.472E-01	1.151E+00
	15	2.174E-01	6.676E-01	1.175E+00
	20	1.695E-01	5.322E-01	9.938E-01
	25	1.531E-01	5.629E-01	8.294E-01
Ti	2.5	7.266E-02	8.603E-02	1.982E-01
	4	1.524E-01	2.396E-01	3.446E-01
	6	2.634E-01	5.246E-01	6.404E-01
	10	3.401E-01	7.648E-01	1.042E+00
	15	2.653E-01	7.475E-01	1.337E+00
	20	2.260E-01	7.231E-01	1.290E+00
	25	2.094E-01	6.758E-01	1.385E+00
Cu	2.5	8.173E-03	3.057E-02	1.814E-02
	4	4.193E-02	5.715E-02	7.802E-02
	6	1.028E-01	1.298E-01	2.391E-01
	10	2.493E-01	2.837E-01	5.616E-01
	15	2.308E-01	3.600E-01	7.756E-01
	20	2.270E-01	4.733E-01	8.847E-01
	25	1.940E-01	4.660E-01	9.689E-01
Zr	2.5	9.557E-05	2.783E-03	2.437E-03
	4	7.367E-04	7.961E-03	7.814E-03
	6	5.869E-03	1.744E-02	2.139E-02
	10	3.247E-02	3.964E-02	4.872E-02
	15	6.000E-02	6.386E-02	1.252E-01
	20	7.499E-02	1.089E-01	1.990E-01
	25	7.703E-02	1.454E-01	2.661E-01

TABLE XIX. Measured Kα x-ray production cross sections (Mb) for Ag, Sm, and Ta targets.

		Ar	Kr	Xe
Ag	2.5	1.656E-05	2.057E-04	1.793E-03
	4	1.056E-04	1.027E-03	4.125E-03
	6	6.923E-04	3.583E-03	9.904E-03
	10	5.919E-03	1.129E-02	2.099E-02
	15	1.861E-02	2.855E-02	4.017E-02
	20	2.949E-02	5.611E-02	6.402E-02
	25	3.588E-02	8.019E-02	8.946E-02
Sm	2.5	1.190E-04	7.565E-07	3.832E-05
	4	7.126E-06	5.804E-06	6.049E-05
	6	3.417E-05	7.393E-05	6.030E-04
	10	2.413E-04	3.515E-04	1.649E-03
	15	1.175E-03	1.704E-03	4.325E-03
	20	2.564E-03	4.901E-03	6.751E-03
	25	4.224E-03	9.843E-03	1.143E-02
Ta	2.5	2.352E-06	5.327E-06	6.679E-06
	4	5.193E-06	7.280E-06	1.110E-05
	6	1.361E-05	1.780E-05	4.656E-05
	10	5.146E-05	7.393E-05	1.788E-04
	15	2.390E-04	3.383E-04	7.261E-04
	20	5.370E-04	9.945E-04	1.567E-03
	25	1.003E-03	2.163E-03	2.877E-03

TABLE XX. Cross sections for K vacancy production by Ar ions. (Numbers in parentheses indicate powers of ten), shading is just for distinguishing different columns.

Target ω_0	E/M MeV/amu	R_s (%)	ω/ω_0	σ_{tot} (Mb)	Target ω_0	E/M MeV/amu	R_s (%)	ω/ω_0	σ_{tot} (Mb)
Al	2.33	7.81	1.79	2.75(0)	Ti	2.30	1.90	1.49	2.47(-1)
0.0382	3.85	9.10	1.72	4.10(0)	0.199	3.81	2.47	1.45	5.22(-1)
	5.87	9.83	1.65	4.08(0)		5.84	2.93	1.39	9.00(-1)
	9.80	9.39	1.53	4.43(0)		9.78	3.42	1.32	1.20(0)
	14.92	8.00	1.41	3.83(0)		14.9	3.76	1.25	1.01(0)
	19.94	7.49	1.33	3.24(0)		19.92	3.98	1.21	8.87(-1)
	24.75	6.98	1.27	2.95(0)		24.73	4.14	1.18	8.22(-1)
Cu	2.27	1.50	1.16	1.77(-2)	Zr	2.3	0	1.04	1.47(-4)
0.399	3.78	2.12	1.15	9.07(-2)	0.616	3.81	0	1.04	1.16(-3)
	5.81	2.66	1.14	2.30(-1)		5.83	0	1.04	8.67(-3)
	9.75	3.32	1.12	5.41(-1)		9.77	0	1.04	5.00(-2)
	14.88	3.83	1.1	5.26(-1)		14.89	0	1.03	9.46(-2)
	19.90	4.19	1.08	5.07(-1)		19.91	0	1.03	1.18(-1)
	24.71	4.46	1.07	4.32(-1)		24.72	0	1.03	1.23(-1)
Ag	2.33	1.48	1.01	2.34(-5)	Sm	3.5	0	1	9.74(-6)
0.685	3.84	1.63	1.03	1.49(-4)	0.738	5.52	0	1	4.76(-5)
	5.86	1.80	1.03	9.73(-4)		9.49	0	1	3.39(-4)
	9.78	2.01	1.03	8.29(-3)		14.79	0	1	1.65(-3)
	14.90	2.05	1.03	2.60(-2)		19.71	0	1	3.60(-3)
	19.92	1.83	1.03	4.26(-2)		24.65	0	1	5.87(-3)
	24.73	1.37	1.03	5.15(-2)					
Ta	2.29	0	1	3.17(-6)					
0.751	3.78	0	1	6.96(-6)					
	5.80	0	1	1.84(-5)					
	9.73	0	1	7.03(-5)					
	14.88	0	1	3.21(-4)					
	19.88	0	1	7.38(-4)					
	24.72	0	1	1.36(-3)					

TABLE XXI. Cross sections for K vacancy production by Kr ions. (Numbers in parentheses indicate powers of ten), shading is just for distinguishing different columns.

Target ω_0	E/M MeV/amu	R_s (%)	ω/ω_0	σ_{tot} (Mb)	Target ω_0	E/M MeV/amu	R_s (%)	ω/ω_0	σ_{tot} (Mb)
Al	2.31	15.0	1.72	6.11(0)	Ti	2.28	3.05	1.66	2.45(-1)
0.0382	3.81	15.1	1.73	1.09(1)	0.199	3.77	4.01	1.64	7.06(-1)
	5.83	15.1	1.73	1.06(1)		5.78	4.82	1.62	1.51(0)
	9.76	15.1	1.73	1.03(1)		9.72	5.68	1.57	2.24(0)
	14.88	14.4	1.7	9.18(0)		14.84	6.26	1.53	2.29(0)
	19.90	13.3	1.65	7.70(0)		19.86	6.62	1.49	2.20(0)
	24.71	11.7	1.59	7.84(0)		24.68	6.89	1.45	2.13(0)
Cu	2.24	2.98	1.24	6.18(-2)	Zr	2.28	0	1.07	4.35(-3)
0.399	3.73	4.34	1.24	1.13(-1)	0.616	3.77	0.76	1.07	1.21(-2)
	5.75	5.71	1.23	2.42(-1)		5.78	2.29	1.07	2.64(-2)
	9.68	7.46	1.21	5.52(-1)		9.70	4.65	1.07	5.46(-2)
	14.81	8.81	1.2	6.98(-1)		14.83	6.45	1.07	9.32(-2)
	19.83	9.61	1.18	9.12(-1)		19.85	6.81	1.06	1.59(-1)
	24.65	10.13	1.17	9.14(-1)		24.67	5.85	1.06	2.15(-1)
Ag	2.31	0	1.05	2.88(-4)	Sm	3.42	0	1	8.27(-6)
0.685	3.80	1.18	1.06	1.44(-3)	0.738	5.85	0	1	1.01(-4)
	5.81	2.84	1.06	4.90(-3)		9.31	0	1	4.80(-4)
	9.73	5.37	1.06	1.52(-2)		14.68	0	1	2.32(-3)
	14.85	7.25	1.06	3.77(-2)		19.52	0	1	6.71(-3)
	19.87	7.52	1.06	7.37(-2)		24.54	0	1	1.35(-2)
	24.68	6.33	1.06	1.05(-1)					
Ta	3.74	0	1	9.69(-6)					
0.751	5.87	0	1	2.34(-5)					
	9.65	0	1	1.01(-4)					
	14.81	0	1	4.53(-4)					
	19.8	0	1	1.36(-3)					
	24.63	0	1	2.93(-3)					

TABLE XXII. Cross sections for K vacancy production by Xe ions. (Numbers in parentheses indicate powers of ten), shading is just for distinguishing different columns.

Target ω_0	E/M MeV/amu	R_s (%)	ω/ω_0	σ_{tot} (Mb)	Target ω_0	E/M MeV/amu	R_s (%)	ω/ω_0	σ_{tot} (Mb)
Al 0.0382	2.31	14.1	1.71	1.01(1)	Ti 0.199	2.28	5.85	1.7	5.61(-1)
	3.81	18.0	1.72	1.55(1)		3.76	7.32	1.69	9.75(-1)
	5.82	19.4	1.73	1.66(1)		5.77	8.39	1.68	1.68(0)
	9.74	19.4	1.74	1.44(1)		9.69	9.29	1.65	2.98(0)
	14.86	17.9	1.74	1.52(1)		14.82	9.64	1.63	4.02(0)
	19.87	16.4	1.74	1.31(1)		19.83	9.69	1.60	3.99(0)
	24.69	14.4	1.72	1.16(1)		24.65	9.64	1.58	4.24(0)
Cu 0.399	2.24	2.09	1.26	3.60(-2)	Zr 0.616	2.28	0	1.08	3.75(-3)
	3.50	3.04	1.25	1.56(-1)		3.76	0.97	1.08	1.19(-2)
	5.73	4.35	1.26	4.64(-1)		5.76	2.95	1.08	3.19(-2)
	9.65	5.99	1.25	1.04(0)		9.68	6.21	1.08	6.99(-2)
	14.77	7.39	1.24	1.47(0)		14.80	9.21	1.08	1.78(-1)
	19.80	8.28	1.23	1.68(0)		19.82	10.77	1.08	2.79(-1)
	24.78	8.89	1.22	1.82(0)		24.63	10.98	1.07	3.64(-1)
Ag 0.685	2.31	3.71	1.07	1.92(-3)	Sm 0.738	3.41	0	1	8.54(-5)
	3.80	4.74	1.07	5.35(-3)		5.83	0	1	8.39(-4)
	5.80	6.02	1.08	1.30(-2)		9.34	0	1	2.24(-3)
	9.70	8.20	1.08	2.68(-2)		14.61	0	1	6.07(-3)
	14.82	10.42	1.07	5.00(-2)		19.42	0	1	9.50(-3)
	19.84	11.88	1.07	7.97(-2)		24.68	0	1	1.56(-2)
	24.65	12.62	1.07	1.07(-1)					
Ta 0.751	5.86	0	1	6.44(-5)					
	9.62	0	1	2.41(-4)					
	14.78	0	1	9.09(-4)					
	19.76	0	1	2.18(-3)					
	24.70	0	1	3.90(-3)					

TABLE XXIII. Average experimental uncertainties of the K vacancy production cross sections.

Target	E/M (MeV/amu)	Uncertainty (%)
Al	2.0 to 25	12
Ti	2.0 to 25	11
Cu	2.0 to 25	5.3
Zr	2.0 to 25	6.3
Ag	2.0 to 4.0	12
Ag	>4.0	4.9
Sm	2.0 to 4.0	13
Sm	>4.0	11
Ta	2.0 to 4.0	12
Ta	>4.0	9.3

CHAPTER VI

DISCUSSION

The present Kα x-ray production cross sections are compared with available experimental results in Section 6.1. Then the K vacancy production cross sections are compared with theoretical predictions in Section 6.2. In Section 6.3, semiemprical scaling laws for Kα x-ray production cross sections are presented.

6.1. Comparison with available experimental results

Balster et al. [188] measured two sets of solid target K x-ray production cross sections (σ_{Kx}). One was for targets of Zr (Z_2 = 40) to Th (Z_2 = 90) bombarded by Ar projectiles at 80 MeV (4.5 MeV/amu). The other one was for targets of Sn (Z_2 = 50) to Bi (Z_2 = 53) bombarded by Ar projectiles at 300 MeV (7.5 MeV/amu). In order to compare their results with the present measurements, they were converted to Kα x-ray production cross sections ($\sigma_{K\alpha}$) using the theoretical (single vacancy) Kβ to Kα intensity ratios of Scofield [187]. The Kα x-ray production cross sections obtained from the results of Balster et al. are plotted as a function of target atomic number in Fig. 56, along with cross sections interpolated from the current results for the same energies.

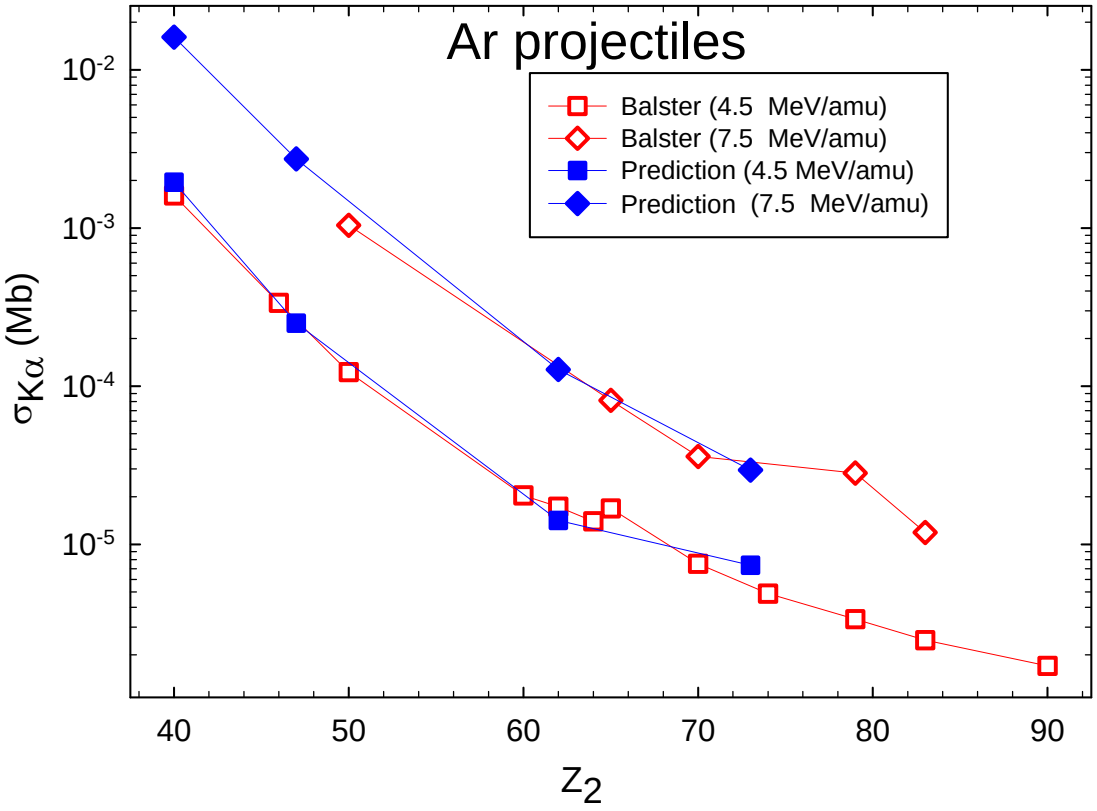

FIG. 56. Cross sections for Kα x-ray production by Ar projectiles at 4.5 and 7.5 MeV/amu as a function of target atomic number: red symbols (Balster et al. [188]), blue symbols (predictions based on interpolation of the current results). The symbols are connected just to guide the eye.

TABLE XXIV. Comparison of Balster et al.'s results with predictions based on interpolations of the current results for Kα x-ray production cross sections. Highlighted data were obtained by interpolation or extrapolation

	Z_2	Prediction (Mb)	Balster (Mb)	Relative deviation (%)	Average Absolute deviation (%)
4.5 MeV/amu	40	1.95E-03	1.61E-03	-21	
	47	2.50E-04	2.83E-04	12	
	62	1.42E-05	1.73E-05	18	21
	73	7.37E-06	5.55E-06	-33	
7.5 MeV/amu	47	2.74E-03	1.46E-03	-88	
	62	1.28E-04	1.61E-04	21	39
	73	2.95E-05	2.74E-05	-8	

It is evident that the two sets of results are in fairly good agreement. A detailed comparison for targets of Zr to Ta is presented in Table XXIV. The highlighted values of Balster et al. in this table were obtained by interpolation or extrapolation. The relative deviations (defined as $\Delta\sigma = \frac{\sigma_{bal} - \sigma_{curr}}{\sigma_{bal}}$, where σ_{bal} are the Balster et al. cross sections and σ_{curr} are the current cross sections) varied from -33% to 18% for 4.5 MeV/amu projectiles with an average absolute deviation of 21% and from -88% up to 21% for 7.5

MeV/amu projectiles with an average absolute deviation of 39%. The large discrepancy for 7.5 MeV/amu Ar on Ag may be caused by the extrapolation of the Balster et al. data.

Meyerhof et al. [29] measured K x-ray production cross sections using Kr ions having an energy of 202 MeV (2.4 MeV/amu) for a wide range of solid targets. Their results are plotted as a function of target atomic number along with the current results for 2.5 MeV/amu Kr projectiles in Fig. 57. The cross sections of Meyerhof et al. shown in Fig. 57 were extracted from their plots of ionization cross sections and converted back to Kα x-ray production cross sections using single vacancy Kα fluorescence yields. The effect of the slightly different incident projectile energies for the two measurements is expected to be less than the experimental uncertainty.

The results of the current measurements for Kr at 4 MeV/amu are also plotted in Fig. 57 for reference. All three sets of data display the same general features characterized by a rapid drop from target atomic number around 20 to 60, followed by a flat region up to Z_2 = 73. A detailed comparison of Kα x-ray production cross sections at 2.4/2.5 MeV/amu for Zr (Z_2 = 40) (the only target used in both measurements), Ti (Z_2 = 22), Cu (Z_2 = 29), and Ag (Z_2 = 47) is presented in Table XXV. Overall, the current results are significantly lower than those of Meyerhof et al. results. The largest relative deviation is 54% for Ag with an average absolute deviation of 38%.

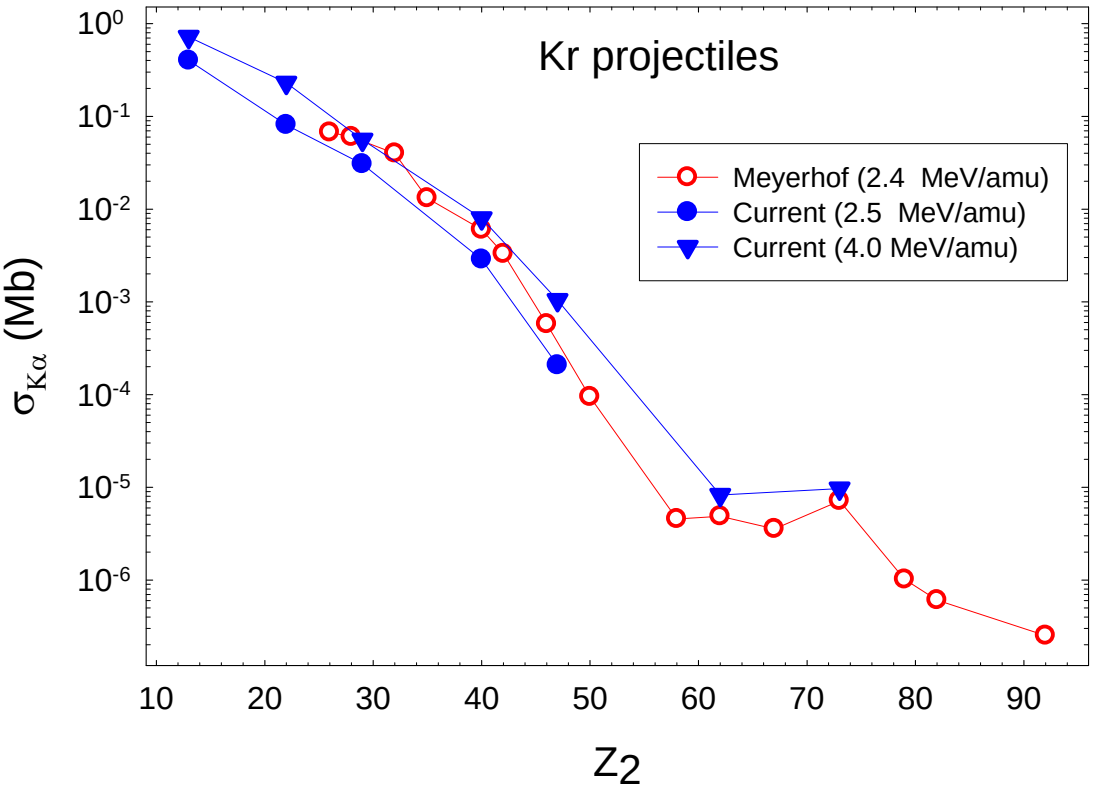

FIG. 57. Cross sections for Kα x-ray production for Kr projectiles at various energies as a function of target atomic number: red symbols (Meyerhof et al. [29]), blue symbols (current work). The symbols are connected just to guide the eye.

TABLE XXV. Comparison of Kα x-ray production cross sections between current measurements (2.5 MeV/amu) and those of Meyerhof et al. (2.4 MeV/amu) for Kr projectiles. Highlighted data were obtained by interpolation or extrapolation.

Z_2	Current	Meyerhof	Relative deviation	Average Absolute deviation
	(Mb)		(%)	
22	8.09E-02	8.10E-02	0	38
29	3.06E-02	5.47E-02	44	
40	2.87E-03	6.02E-03	52	
47	2.07E-04	4.54E-04	54	

In Meyerhof's measurements, the Ge (Z_2 = 32) cross section is enhanced relative to the trend defined by the surrounding targets. This is probably due to contributions from the molecular orbital level crossing mechanism since Ge (Z = 32) and Kr (Z = 36) have comparable atomic numbers.

Current Kα x-ray production cross sections for Xe projectiles at incident energies of 2.5 MeV/amu along with interpolated predictions for 2.95 MeV/amu, based on the current results are plotted as a function of target atomic number in Fig. 58. The results of Meyerhof et al. (extracted from their plots as explained previously) are also presented for Xe projectiles having energies of 326 MeV (2.4 MeV/amu) and 387 MeV (2.95 MeV/amu). For the most part, all of the data sets display similar trends from Z_2 around 29 (Cu) to 62 (Sm). Detailed comparisons of the cross sections for Ti, Cu, Zr, and Ag are shown in Table XXVI. For 2.4 and 2.5 MeV/amu, the current measurements and those of Meyerhof et al. are in close agreement for target atomic numbers from 22 to 47. The differences are almost negligible for Zr and Ag targets, while a very large discrepancy exists for Ti (71%). This large discrepancy might be caused by uncertainties in the detector efficiency calibration at low photon energies in the measurements of Meyerhof et al..

The 2.95 MeV/amu data display essentially the same features described above.

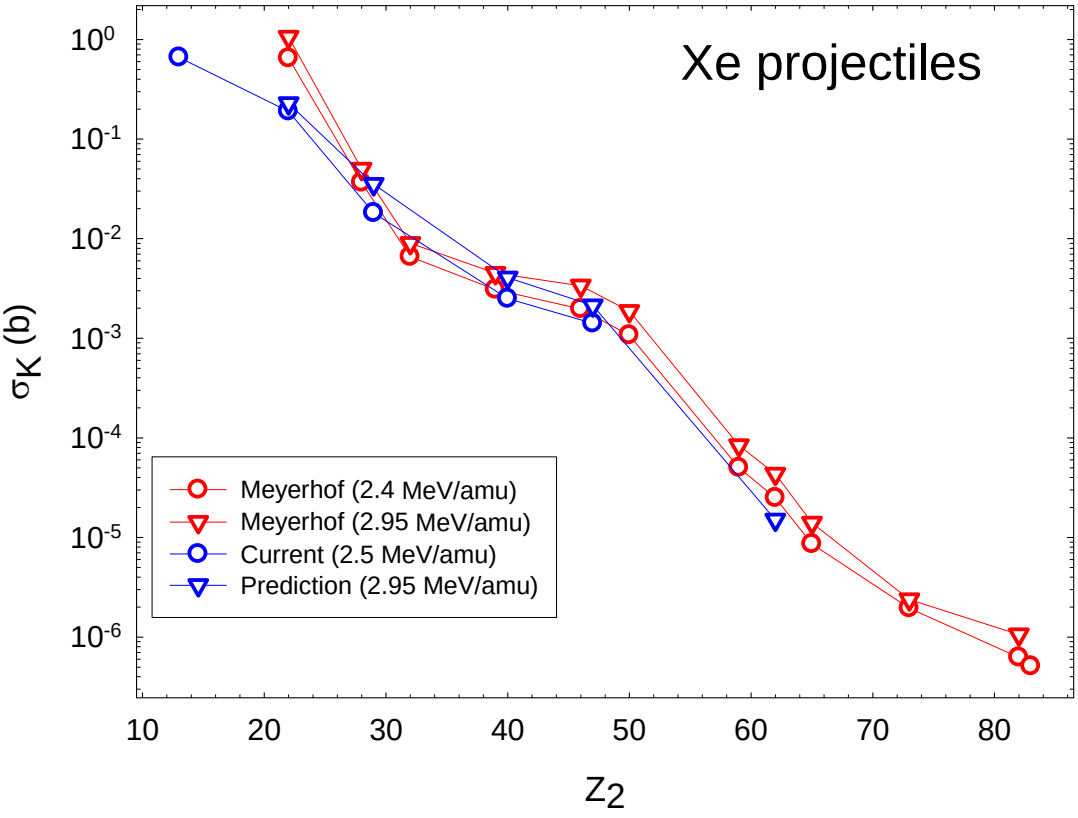

FIG. 58. Cross sections for Kα x-ray production by Xe projectiles at various energies as a function of target atomic number: red symbols (Meyerhof et al. [29]), blue symbols (current results or prediction). The symbols are connected just to guide the eye.

TABLE XXVI. Comparison between Kα x-ray production cross sections for Xe projectiles at 2.5 MeV/amu and at 2.95 MeV/amu. Highlighted data were interpolated or extrapolated.

	Z_2	Current (Mb)	Meyerhof (Mb)	Relative deviation (%)	Average absolute deviation (%)
2.4-2.5 MeV/amu	22	1.90E-01	6.50E-01	71%	
	29	1.81E-02	2.91E-02	38%	
	40	2.49E-03	2.92E-03	15%	36%
	47	1.41E-03	1.75E-03	19%	
2.95 MeV/amu	22	2.28E-01	1.06E+00	78%	
	29	3.52E-02	3.98E-02	12%	
	40	4.06E-03	4.34E-03	7%	38%
	47	2.13E-03	2.99E-03	29%	
	62	1.51E-05	4.35E-05	65%	

6.2. Comparison with theory

The K vacancy production cross sections divided by Z_1^2 are compared with the predictions of the ECPSSR theory in Fig. 59 through Fig. 61. The ECPSSR cross sections include contributions from both direct K-shell ionization [18, 79] and K-electron capture to the projectile [23, 80]. In the electron capture calculations, the

projectiles were assumed to have equilibrated ground state electron configurations. Also shown in the cross section figures are ECPSSR cross section curves for proton projectiles. The experimental results for Ar projectiles lie far below the theoretical predictions for Al, but for Ti, they are only 23% (on average) below, except for the point at the lowest V, which is 30% above. The Cu data are all substantially above the theoretical curve (65% on average), but the Zr and Ag data agree well with theory at V below 0.5 and rise above the theoretical curves beyond.

The experimental results for Kr and Xe projectiles on the targets Al through Ag are in very poor agreement with the theoretical curves. In the cases of the Al and Ti targets, the data points all lie far below the theoretical curves. For the Cu, Zr, and Ag targets, the data points start out considerably above the theoretical curves at low V, cross over at some intermediate V, and fall below at high values of V. The experimental data points for Kr on Sm and those for Kr on Ta (except for those at the lowest two values of V) agree quite well with theory. Evidence of cross section enhancement due to contributions from the molecular orbital level crossing mechanism can be seen at V below 0.5 in the data for Kr on Cu and Zr, and in the data for Xe on Ag, Sm, and Ta, as has been demonstrated in previous experiments at 10 MeV/amu [189, 190].

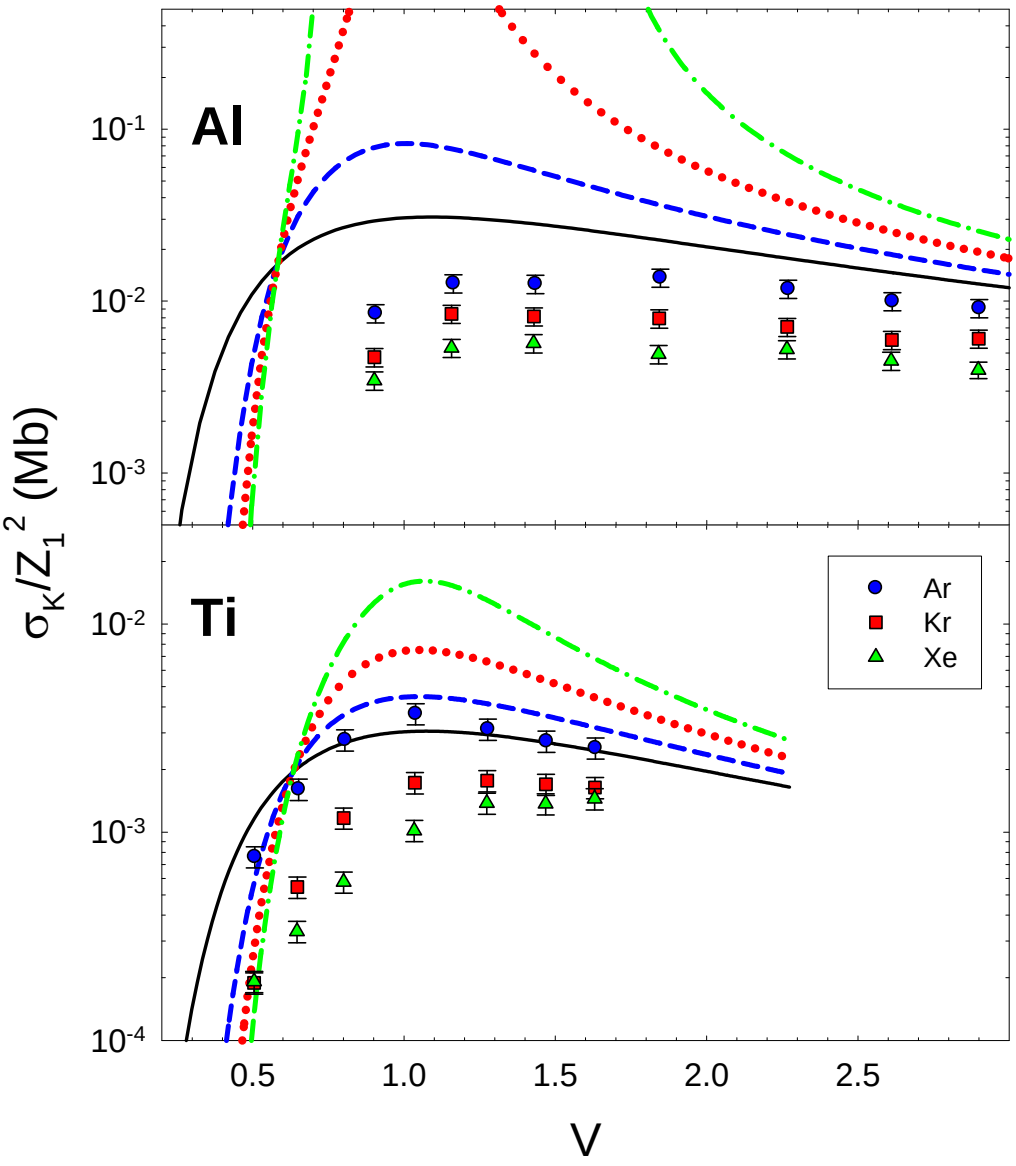

FIG. 59. Comparison of the experimental results for Al and Ti with the predictions of the ECPSSR theory. The theoretical curves are for Ar (blue dashed), Kr (red dotted), and Xe (green dot-dashed) projectiles. The solid curve shows the ECPSSR predictions for protons.

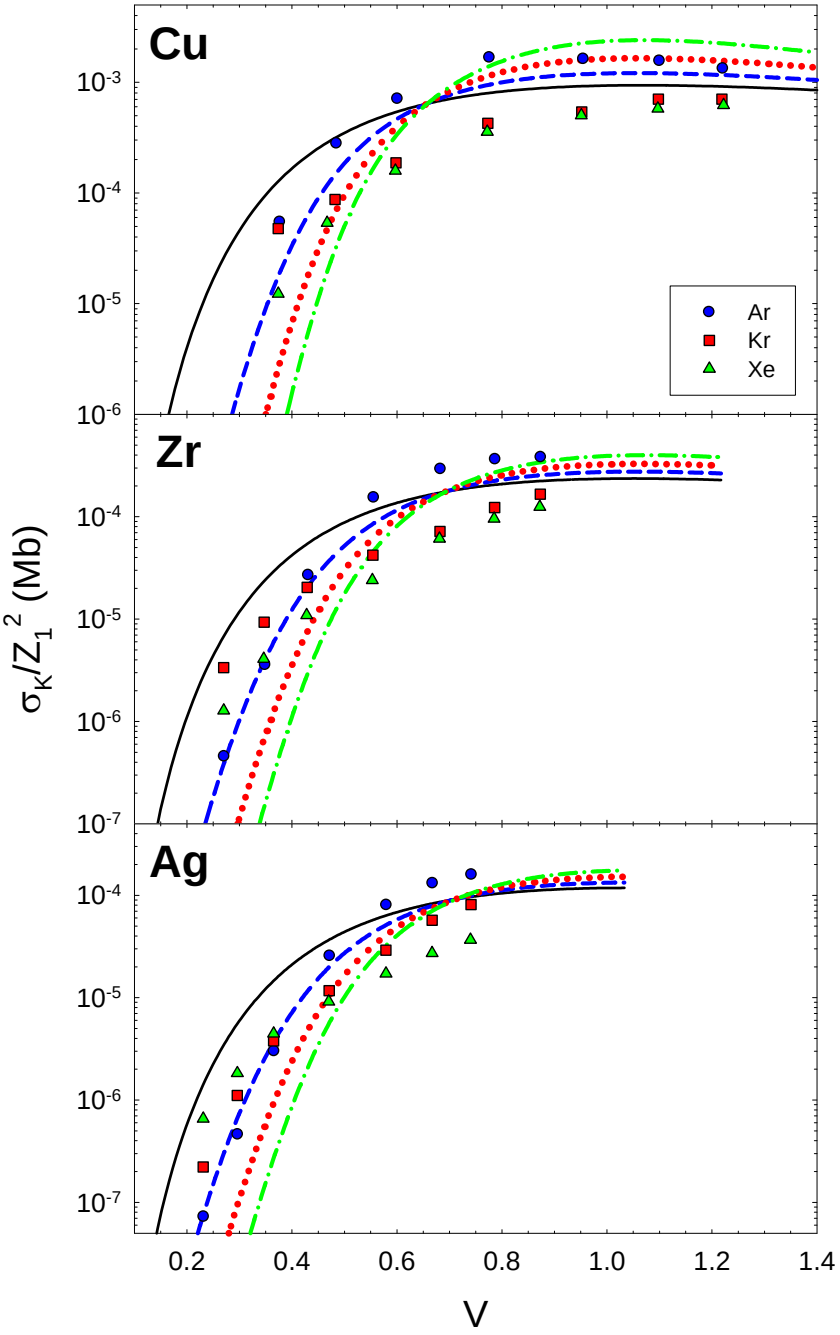

FIG. 60. Comparison of the experimental results for Cu, Zr, and Ag with the predictions of the ECPSSR theory. The theoretical curves are for Ar (blue dashed), Kr (red dotted), and Xe (green dot-dashed) projectiles. The solid curve shows the ECPSSR predictions for protons. (The experimental error bars are smaller the size of the data points).

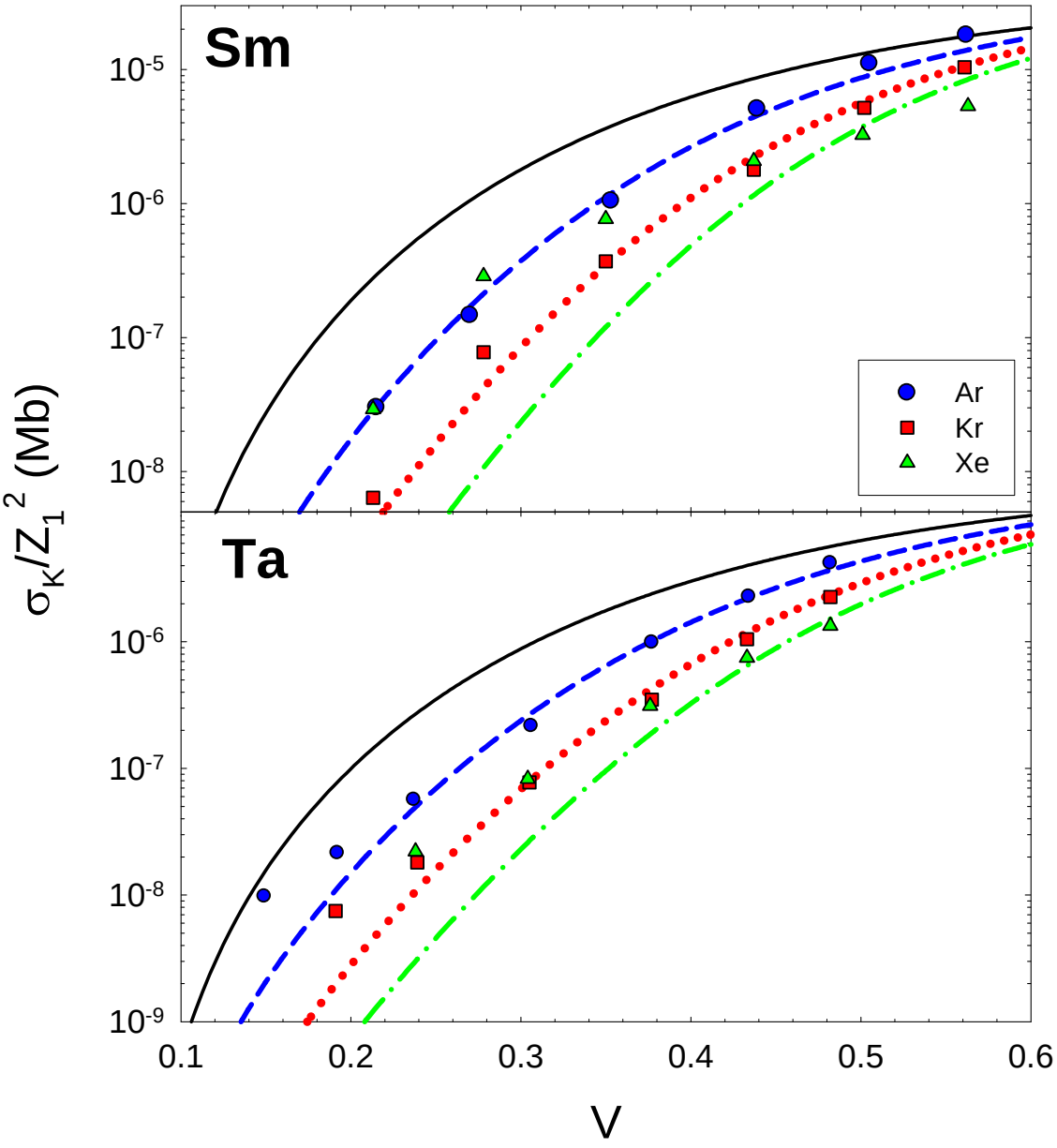

FIG. 61. Comparison of the experimental results for Sm and Ta with the predictions of the ECPSSR theory. The theoretical curves are for Ar (blue dashed), Kr (red dotted), and Xe (green dot-dashed) projectiles. The solid curve shows the ECPSSR predictions for protons. (The experimental error bars are smaller the size of the data points).

6.3. Scaling of the cross sections

In view of the fact that reliable theoretical methods for predicting cross sections for K x ray production in heavy ion-atom collisions have yet to be developed, and because these cross sections are of practical use in analytical applications and for beam monitoring in experiments with heavy ions, it is desirable to examine scaling relations that might provide a means for their estimation. First-order descriptions of inner-shell ionization based on the PWBA as well as the classical binary encounter approximation (BEA) predict that target K-shell ionization cross sections are proportional to the square of the projectile effective charge (Z_{eff}^2) divided by the square of the target electron binding energy (B_K^2) times a function that defines the V dependence of the collision process. Therefore, a plot of the K-shell ionization cross section multiplied by B_K^2 / Z_{eff}^2 versus V should define a universal function that depends only on V. This type of scaling has been found to work reasonably well for proton and alpha particle projectiles with Z_{eff} taken to equal Z_1 [96].

6.3.1. Kα x-ray cross sections

In the present case involving heavy ion projectiles, the goal of providing a convenient scaling method for estimating K x-ray production cross sections is obscured by the fluorescence yield factor (which depends on the degree of multiple ionization) since its calculation is difficult and relies on a number of untested approximations and assumptions. Therefore, in the present treatment, it was decided to replace the

calculated fluorescence yield $\omega_{K\alpha}$ with the single vacancy fluorescence yield ω_0 and, in effect, consider it to be part of the overall scaling factor. The effectiveness of the B_K^2 / ω_0 scaling factor in accounting for the target dependence of the cross sections is demonstrated in Fig. 62 and Fig. 63. In Fig. 62, where the Kα x-ray production cross section divided by ω_0 is plotted as a function of V, it is apparent that the data points for the various targets define individual curves and that these curves differ for each projectile. When the data in Fig. 62 are multiplied by B_K^2, as shown in Fig. 63, the individual curves blend together (with the exception of the Al data) to approximately define a common target curve for each projectile.

In seeking to account for the projectile dependence of the Kα x-ray production cross sections, it is obvious from Fig. 59 through Fig. 61 that setting $Z_{eff} = Z_1$ will not work. Instead, the following procedure was found to provide values for Z_{eff} that gave reasonably good projectile scaling. Because the Al data points sampled the highest V region, where the V dependence is nearly constant, the four cross sections measured at 10, 15, 20, and 25 MeV/amu were chosen to establish the average Z_{eff} scaling factors, defined as

$$Z_{eff} = \left\{ \frac{\sigma_{K\alpha}(Z_1)}{\omega_0 \sigma_K(1)} \right\}^{1/2} \tag{91}$$

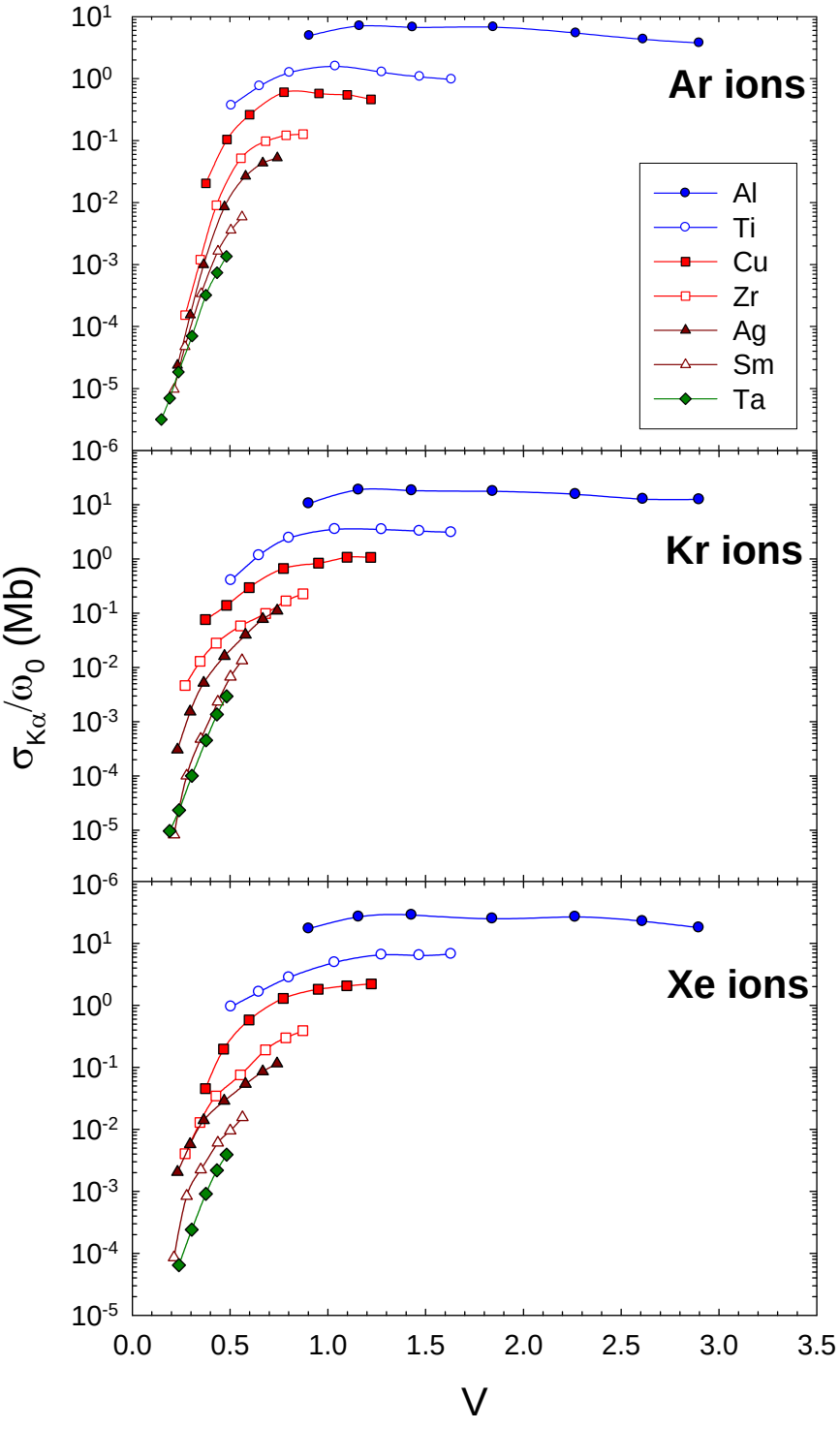

FIG. 62. The sets of Kα x-ray production cross sections divided by the single vacancy fluorescence yields, as a function of speed ratio (shown separately for each projectile).

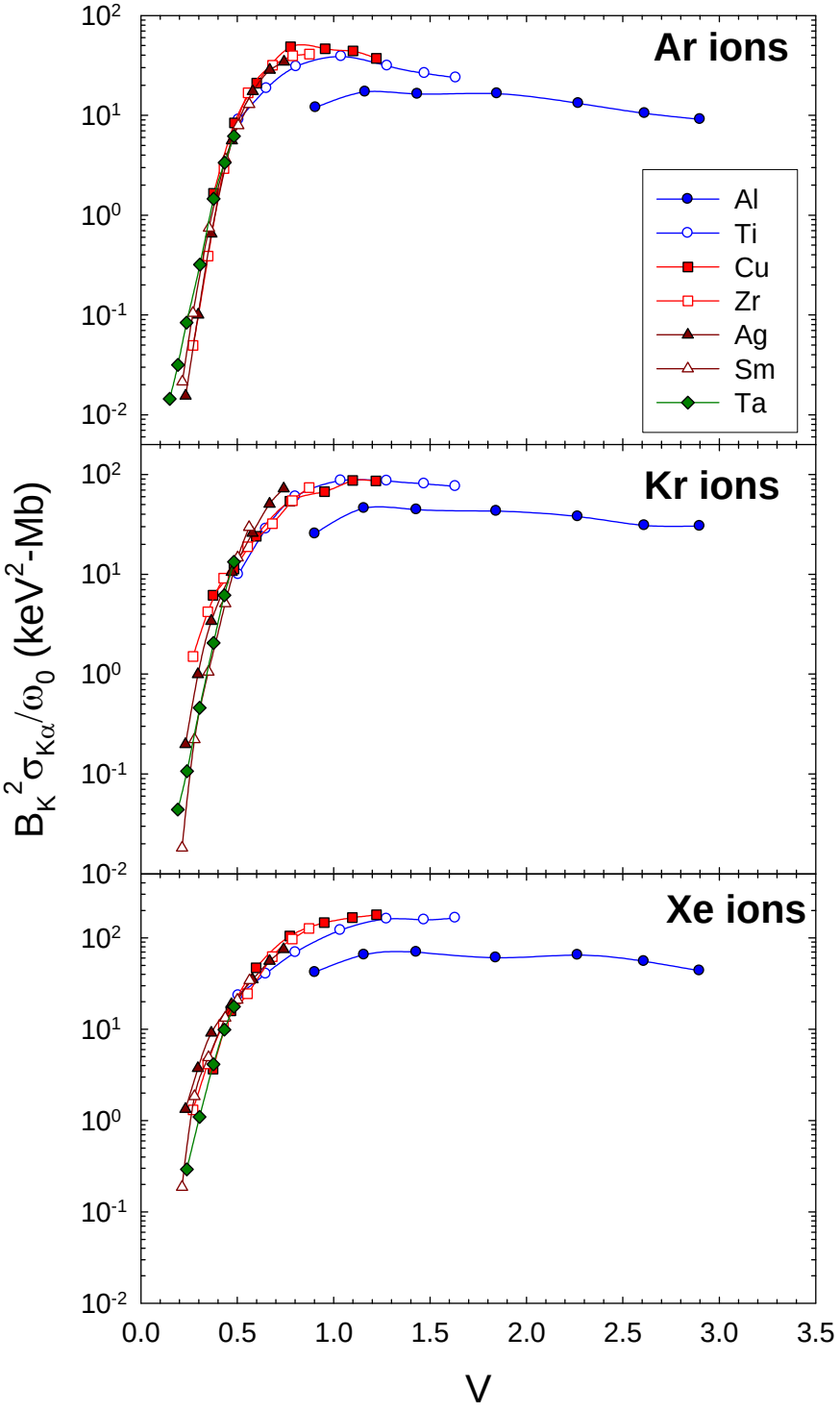

FIG. 63. The data in FIG. 62 multiplied by the scaling factor B_K^2 for each target, as a function of speed ratio (shown separately for each projectile).

where $\sigma_{K\alpha}(Z_1)$ is the Al Kα x-ray production cross section for a projectile with atomic number Z_1 and $\sigma_K(1)$ is the ECPSSR K-shell ionization cross section for protons on Al. The fully scaled cross sections are shown in Fig. 64 as a function of V. It is found that dividing the data in Fig. 63 by Z_{eff}^2 has the effect of grouping most of the data points for all three projectiles along a "universal" curve. A fit to the data points (which excluded the Al points for the measurements at 2.5, 4, and 6 MeV/amu) using an extreme value four parameter tailed function is shown by the solid curve in Fig. 64. The equation of this curve is

$$F(V) = a_0 \exp(B), \tag{92}$$

where

$$B = \frac{-V + a_1 + a_2 - a_2 a_3 e^{\frac{-(V + a_2 \ln a_3 - a_1)}{a_2}}}{a_2 a_3}, \tag{93}$$

with $a_0 = 0.113$, $a_1 = 1.069$, $a_2 = 0.234$, and $a_3 = 4.486$. The average absolute deviations of the Kα x-ray production cross sections calculated using Eq. (92) from the experimental cross sections are given in Table XXVII.

A graph of Z_{eff} versus Z_1 is shown in Fig. 65. The error bars on the data points for Ar, Kr, and Xe represent the standard deviations from the average values of Z_{eff} determined using the four Al cross sections. The other data points in Fig. 65 were calculated using Al cross sections from a previous study [19] at 10 MeV/amu that were re-evaluated to include the double K-vacancy production contributions. The equation of the fitted solid curve in this figure is

$$Z_{eff} = 46.29\left[1 - e^{-0.0256 Z_1}\right] \tag{94}$$

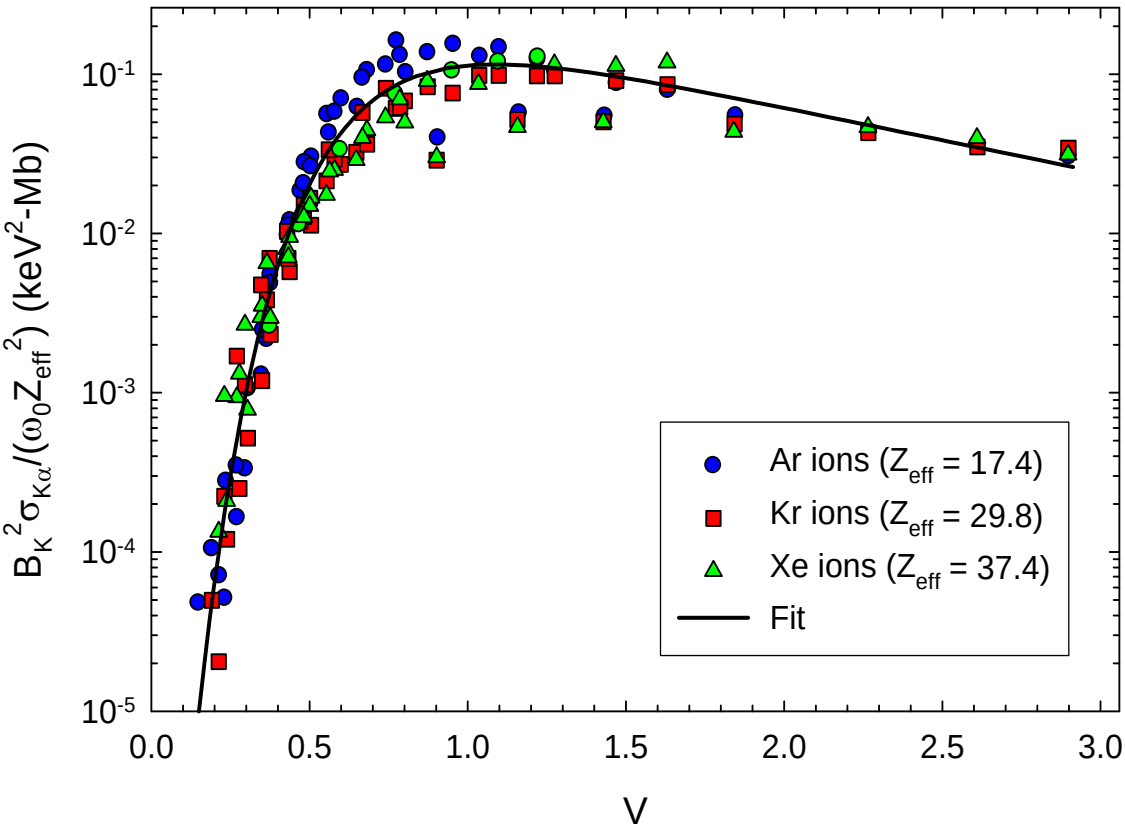

FIG. 64. The fully scaled Kα x-ray production cross sections as a function of speed ratio. A semiempirical universal curve has been fit to the data points.

TABLE XXVII. Average absolute deviations of the Kα x-ray production cross sections calculated using Eq. (92) from the experimental cross sections.

Target	$\Delta\sigma_{K\alpha}$ Ar (%)	$\Delta\sigma_{K\alpha}$ Kr (%)	$\Delta\sigma_{K\alpha}$ Xe (%)	Restrictions
Al	12.6	18.9	25.8	V > 1.8
Ti	10.9	25.1	35.7	none
Cu	32.0	27.4	12.5	none
Zr	36.9	38.4	26.3	V > 0.3
Ag	33.1	13.6	34.8	V > 0.3
Sm	15.8	39.4	33.5	V > 0.3
Ta	29.0	23.0	18.4	V > 0.2

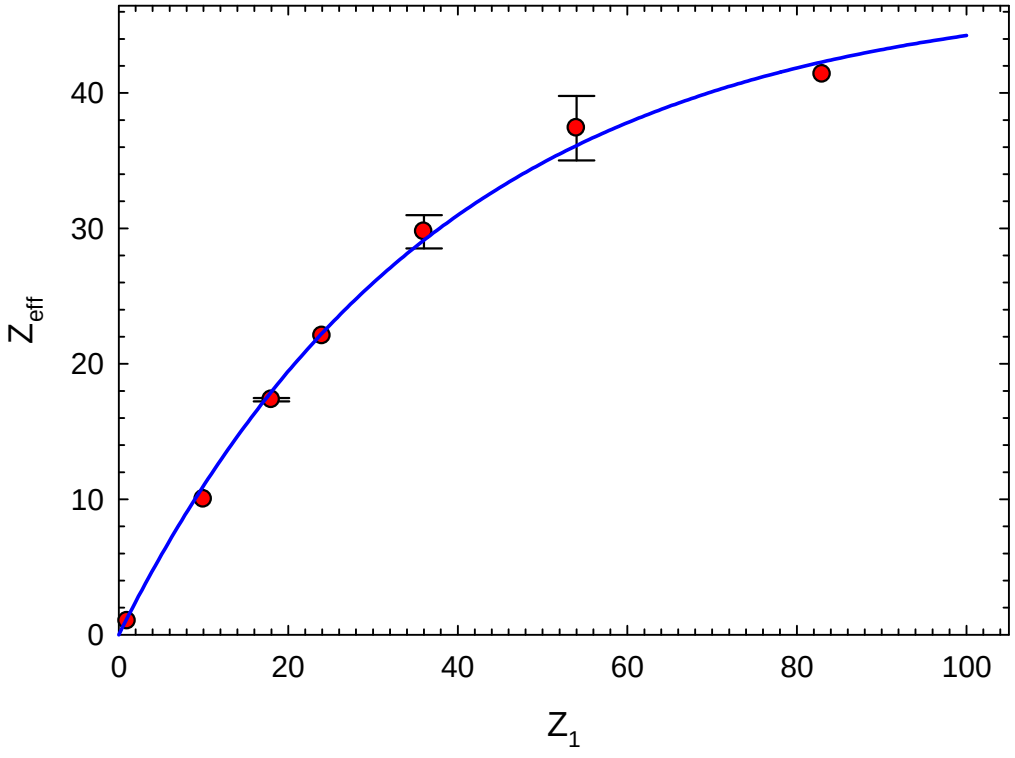

FIG. 65. A graph showing the dependence of the projectile effective charge on the projectile atomic number. The solid curve has been fit to the data points.

6.3.2. Scaling law based on the Geometrical Model

As mentioned in Chapter V and discussed in detail in Ref. [96], the apparent average L-vacancy fraction is a universal function of the universal variable X, according to the Geometrical Model. In order to investigate the dependence of total Kα x-ray production cross sections on X, Kα x-ray production cross sections are shown plotted as a function of universal variable in Fig. 66. Apparently, the data points for each projectile define different curves, but these curves seem to have similar trends.

It was found that most of the data points for all three projectiles are grouped along a single "universal" curve when the Kα x-ray production cross sections are divided by the square of the effective projectile atomic number [determined from Eq. (94)] while the universal variable is multiplied by $\frac{v_1}{4Z_1Z_2}$. The new abscissa variable is defined as $X' = X\frac{v_1}{4Z_1Z_2} = V\left[G(V)\right]^{\frac{1}{2}} / Z_2$. The scaled Kα x-ray production cross sections as a function of the new variable X' are shown in Fig. 67. This "universal" curve can be described by the following two functions. One is

$$y = \frac{a}{1+\left(\frac{b}{x}\right)^c}, \tag{95}$$

for X' from 10^{-9} to 0.0020 with a = 7.88 × 10^{-3}, b = 7.50 × $10^{-2,}$ and c = 4.05 and the other is

$$y = y_0 + ae^{-0.5\left(\frac{|x-x_0|}{b}\right)^c}, \tag{96}$$

for X' from 0 .0020 to 0.10 with a = 8.00×10^{-4}, b = $4.12 \times 10^{-2,}$ c = 6.29, $x_0 = 6.04 \times 10^{-2}$, and $y_0 = -7.20 \times 10^{-6}$. The average absolute deviations (defined as $\Delta\sigma = \left|\sigma_{pre} - \sigma_{\exp}\right| / \sigma_{pre}$, where σ_{pre} is the predicted and $\sigma_{\exp}$ is the experimental Kα x-ray production cross section) of the Kα x-ray production cross sections calculated using Eqs. (95) and (96) from the experimental cross sections are given in Table XXVIII. Data points having absolute deviations greater than 200% were not included in the average absolute deviation calculation, but most of them were for small values of X' (much less than 0.0020). The average relative deviations are significantly reduced by considering only data points for X' > 0.0020.

.

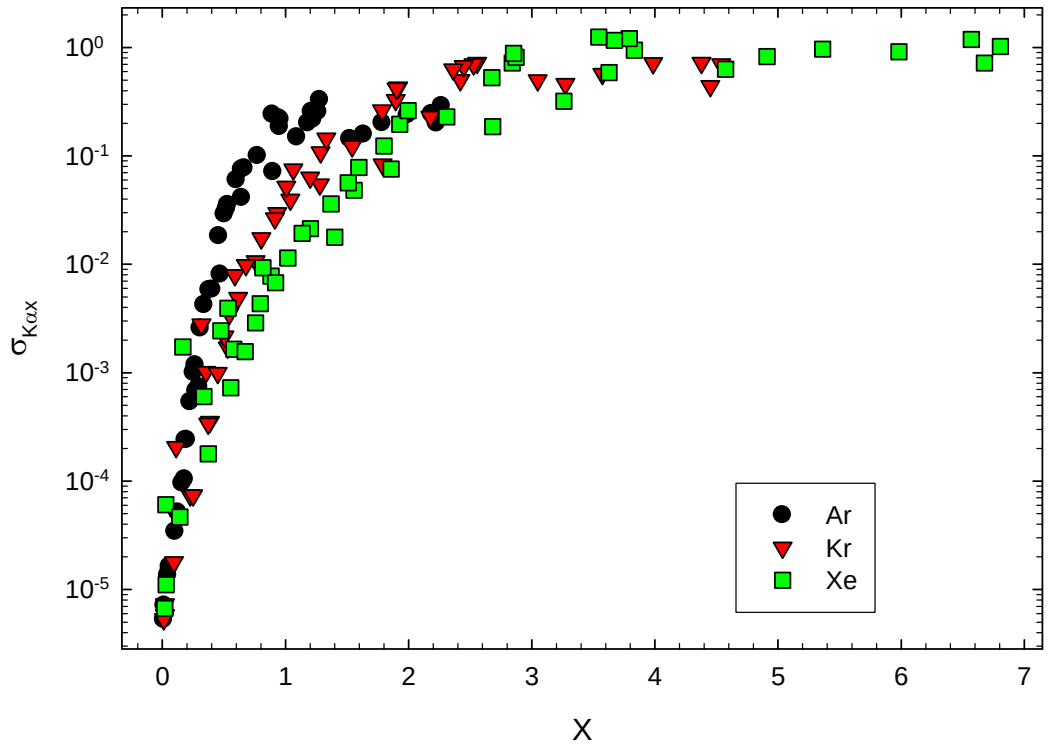

FIG. 66. Kα x-ray production cross sections (Mb) as a function of universal variable.

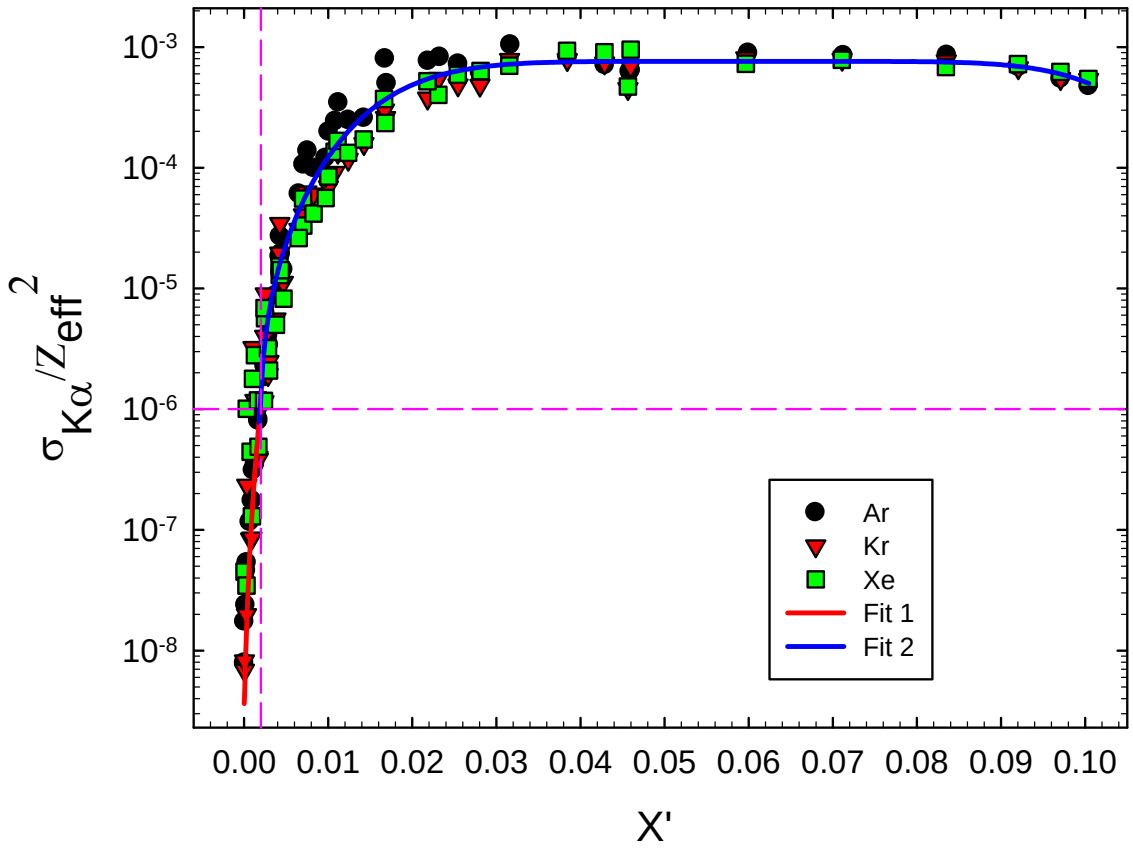

FIG. 67. Kα x-ray cross section divided by square of projectile effective atomic number as a function of X'. The solid curves are the best fit lines given by Eqs. (95) and (95) while the dashed pink lines indicate the validate regions for the two fits.

TABLE XXVIII. Average absolute deviations of the Kα x-ray production cross sections calculated using Eqs. (95) and (96) from the experimental cross sections. Shaded values are for X' greater than 0.00020.

Target	$\Delta\sigma_{K\alpha}$ (Ar) (%)		$\Delta\sigma_{K\alpha}$ (Kr) (%)		$\Delta\sigma_{K\alpha}$ (Xe) (%)	
Al	11.0		9.9		9.6	
Ti	27.5		15.3		20.6	
Cu	62.0		34.4		8.2	
Zr	40.8	31.0	41.2	Zr	40.8	31.0
Ag	15.7	14.4	17.2	Ag	15.7	14.4
Sm	30.1	14.7	38.2	Sm	30.1	14.7
Ta	21.4	14.4	49.4	Ta	21.4	14.4

CHAPTER VII

CONCLUSION

In the present investigation, cross sections for K-shell ionization by heavy ions have been determined from measurements of target K x-ray yields. The measurements were performed with Ar, Kr, and Xe ions at energies of 2.5, 4, 6, 10, 15, 20, and 25 MeV/amu and self-supported metallic foil targets of Al, Ti, Cu, Zr, Ag, Sm, and Ta. X-rays were detected with a Si(Li) detector, while the particle were counted in coincidence with the x-rays using a plastic scintillation detector.

Relative x-ray yields were obtained for Sm and Ta targets as well for the Ag targets at 2.5 and 4.0 MeV/amu. In the case of Ag, a reference target of Cu was employed to determine the absolute yield of Cu K x-rays. Then the particle detector was removed and a thin Al absorber was used to absorb low energy (L) x-rays. Finally, an x-ray spectrum containing both the target and the reference K x-rays was recorded. In the case of Sm and Ta, reference foils of Ag and a three step procedure were employed.

In addition, high resolution measurements have been performed with a curved crystal spectrometer for Al, Ti, and V targets in first order, and for Co and Cu targets in second order using the same projectiles and energies as in the cross section measurements to assess the degree of simultaneous L-shell ionization and the enhancement of the Kα diagram lines due to secondary ionization processes. This information was needed to

correct the Kα x-ray production cross sections for contribution from secondary ionization processes and to calculate the fluorescence yields needed to convert the Kα x-ray production cross sections into K vacancy production cross sections. In these high resolution measurements, an EDD crystal was employed for the Al target while a LiF(200) crystal was employed for all the other targets.

The targets were thick enough to insure full charge state equilibration of the projectile ions, but thin enough that energy loss was not a major concern (except in the case of the thicker Sm target at the lower energies). This was confirmed by the calculation of the mean effective projectile energies with a numerical method, which showed that the maximum energy change was less than 30%. and the effects of energy loss were less than 5% on the final values of the cross sections [96].

The high resolution spectra also revealed systematic dependencies on the collision parameters of important spectral features associated with multiple vacancy production. Specifically, the apparent average L-shell spectator vacancy fraction at the time of Kα x-ray emission, p_L, was found to be a universal function of the Geometrical Model's parameter X for Z_2 = 17 - 32. This finding provided a means of estimating the the apparent degree of simultaneous K plus L shell ionization for any projectile/target combination within the current collision regime.

Multiple-vacancy Kα fluorescence yields were calculated using information about the vacancy distribution provided by the high resolution spectra for targets from Al to Cu based on the method described in Ref. [96]. Those for Zr to Ta were estimated using an extrapolation procedure.

Kα diagram peak enhancement [Eq. (73)] were also determined from the high resolution measurements for Al to Cu targets. In the case of Zr and Ag targets, this factor was determined from the low resolution K x-ray spectra by measuring the $K\beta_1'$ x-ray diagram peak intensity and employing theoretical intensity ratios of $K\beta_1'$ to Kα for single vacancy atoms from Scofield et al. [187]. Corrections for secondary ionization in the Sm and Ta targets were estimated to be negligible due to the fact that both the projectile K x-rays and the ejected electrons have energies that are below the target K binding energies.

The Kα x-ray production cross sections for Ar projectiles at 4.5 and 7.5 MeV/amu, interpolated from the current results, were compared with those of Balster et al. [188]. The two sets are in fairly good agreement for the targets of Zr (Z_2 = 40) to Ta (Z_2 = 73) with an average absolute deviation of 21% and 39% for Ar at energies of 4.5 and 7.5 MeV/amu, respectively.

Comparisons of the present Kα x-ray production cross sections with those of Meyerhof et al. for Kr and Xe projectiles at energies from 2.4 to 4 MeV/amu show similar overall trends as a function of target atomic number, but the current results are systematically lower than those of Meyerhof et al.. The two sets of measurements have average absolute deviations of 38 % for Kr and 36 % for Xe projectiles at 2.5 MeV/amu over the target range from Zr (Z_2 = 40) to Ta (Z_2 = 73) and from Ti (Z_2 = 22) to Sm (Z_2 = 62), respectively. The Kα x-ray production cross sections for Xe projectiles at 2.95 MeV/amu were also compared and found to have similar features. The average absolute deviation of the two sets of data was 36%.

The K vacancy production cross sections for Ar projectiles were found to agree reasonably well with the predictions of the ECPSSR theory for all targets except Al. The cross sections for Al were as much as an order of magnitude lower than the theoretical values at the lowest projectile speed. The cross sections for K-vacancy production in Al and Ti by Kr and Xe projectiles were considerably below the ECPSSR cross sections over the whole range of projectile energy, while those for Cu, Zr, and Ag were above the ECPSSR predictions at low energies and below at high energies. The cross sections for Kr on Sm and Ta were in good agreement with the theory, but those for Xe on Sm and Ta, which contain substantial contributions from the molecular orbital promotion mechanism, were much larger than the theoretical cross sections when the ratio of projectile to K-electron speed (V) dropped below 0.4.

Examination of the scaling properties of the Kα x-ray production cross sections revealed that multiplication by the factor B_K^2/ω_0 (where B_K is the target K-shell electron binding energy and ω_0 is the theoretical fluorescence yield for single vacancy atoms) removes the target dependence for the most part. Also, it was found that the projectile dependence is nearly independent of V and can be taken into account by a factor representing the square of the projectile effective charge (Z_{eff}^2). Multiplying the Kα x-ray production cross sections by $B_K^2/(\omega_0 Z_{eff}^2)$ resulted in a universal function of V. The universal curve reproduced the measured cross sections to within ± 30 % on average and may be used to estimate cross sections for other collision systems that have not yet been measured. The values of Z_{eff} were determined for Z_1 = 1 to 83.

The relationship between the Kα x-ray production cross sections and the geometrical

model's universal variable (X) was examined. It was found that the Kα x-ray production cross sections plotted as a function of X defined different curves for each projectile, but these curves displayed similar trends

When the Kα x-ray production cross sections were divided by the square of the effective projectile atomic number and plotted as a function of the universal variable multiplied by $\frac{v_1}{4Z_1Z_2}$, most of the data points for all three projectiles became grouped along a single "universal" curve. This curve was described by a modified Gaussian function for X' greater than 0.0020 and by another function for X' less than 0.0020. The overall average absolute deviations are within ±23% except for Ar on Cu and those of X' less than 0.0020.

REFERENCES

[1] J. H. Hubbell, P. N. Trehan, N. Singh, B. Chand, D. Mehta, M. L. Garg, R. R. Garg, S. Singh, and S. Puri, J. Phys. Chem. Ref. Data **23**, 339 (1994).

[2] H. H. Bransden and M. R. C. Mcdowell, *Charge Exchange and the Theory of Ion-Atom Collisions* (Clarendon Press, Oxford, 1992).

[3] R. K. Janev, *Atomic and Molecular Processes in Fusion Edge Plasmas* (Plenum, New York, 1995).

[4] J. D. Lindl, *Inertial Confinement Fusion* (Springer, New York, 1998).

[5] G. Moschini and V. Valkovic, *Proceedings of the Seventh International Conference on PIXE and Its Analytical Applications* (ScienceDirect, Padua, Italy, 1995).

[6] M. Uda, *Proceedings of the Sixth International Conference on PIXE and Its Analytical Applications* (ScienceDirect, Tokyo, Japan, 1992).

[7] J. Bang and J. M. Hansteen, Kgl. Dan. Vid. Selsk. Mat.-Fys. Medd. **31**, 13 (1959).

[8] L. Kocbach, J. M. Hansteen, and R. Gundersen, Nucl. Instrum. Methods **169**, 281 (1980).

[9] M. Pauli, F. Rosel, and D. Trautmann, J. Phys. B **11**, 2511 (1978).

[10] M. Pauli, F. Rosel, and D. Trautmann, Phys. Lett. A **67**, 28 (1978).

[11] M. Pauli and D. Trautmann, J. Phys. B **11**, 667 (1978).

[12] D. Trautmann and T. Kauer, Nucl. Instrum. Methods Phys. Res. B **42**, 449 (1989).

[13] W. Brandt, R. Laubert, and I. Sellin, Phys. Rev. **151**, 56 (1966).

[14] G. Basbas, W. Brandt, and R. Laubert, Phys. Rev. A **7**, 983 (1973).

[15] W. Brandt and G. Lapicki, Phys. Rev. A **10**, 474 (1974).

[16] G. Basbas, W. Brandt, and R. Laubert, Phys. Rev. A **17**, 1655 (1978).

[17] W. Brandt and G. Lapicki, Phys. Rev. A **20**, 465 (1979).

[18] W. Brandt and G. Lapicki, Phys. Rev. A **23**, 1717 (1981).

[19] R. Watson, V. Horvat, J. Blackadar, and K. Zaharakis, Phys. Rev. A **62**, 052709 (2000).

[20] R. Watson, J. Blackadar, and V. Horvat, Phys. Rev. A **60**, 2959 (1999).

[21] H. Paul and J. Muhr, Physics Reports **135**, 47 (1986).

[22] G. Basbas, W. Brandt, and R. H. Ritchie, Phys. Rev. A **7**, 1971 (1973).

[23] G. Lapicki, M. Goldstein, and W. Brandt, Phys. Rev. A **23**, 2727 (1981).

[24] G. Lapicki, R. Laubert, and W. Brandt, Phys. Rev. A **22**, 1889 (1980).

[25] W. E. Meyerhof and R. Anholt, J. Phys. B **12**, 3919 (1979).

[26] W. E. Meyerhof, R. Anholt, J. Eichler, and A. Salop, Phys. Rev. A **17**, 108 (1978).

[27] W. E. Meyerhof, R. Anholt, and T. Saylor, Phys. Rev. A **16**, 169 (1977).

[28] R. Anholt and W. Meyerhof, Phys. Rev. A **16**, 190 (1977).

[29] W. E. Meyerhof, R. Anholt, T. K. Saylor, S. M. Lazarus, A. Little, and L. F. Chase, Phys. Rev. A **14**, 1653 (1976).

[30] R. Anholt, W. Meyerhof, and A. Salin, Bull. Amer. Phys. Soc. **21**, 1301 (1976).

[31] W. E. Meyerhof, T. Saylor, S. Lazarus, A. Little, B. Triplett, L. Chase, and R. Anholt, Phys. Rev. Lett. **32**, 1279 (1974).

[32] R. Anholt and W. Meyerhof, Bull. Amer. Phys. Soc. **19**, 592 (1974).

[33] I. P. Grant, B. J. Mckenzie, P. H. Norrington, D. F. Mayers, and N. C. Pyper, Comp. Phys. Comm. **21**, 207 (1980).

[34] K. Taulbjerg and J. S. Briggs, J. Phys. B **8**, 1895 (1975).

[35] M. Barat and W. Lichten, Phys. Rev. A **6**, 211 (1972).

[36] U. Fano and W. Lichten, Phys. Rev. Lett. **14**, 627 (1965).

[37] J. S. Briggs and K. Taulbjerg, J. Phys. B **8**, 1909 (1975).

[38] K. Taulbjerg and J. S. Briggs, J. Phys. B **8**, 1895 (1975).

[39] W. E. Meyerhof, Phys. Rev. Lett. **31**, 1341 (1973).

[40] R. Anholt, W. E. Meyerhof, C. Stoller, E. Morenzoni, S. A. Andriamonje, J. Molitoris, O. Baker, D. Hoffmann, H. Bowman, J. S. Xu, Z. Xu, K. Frankel, D. Murphy, and K. Crowe, Phys. Rev. A **30**, 2234 (1984).

[41] R. Anholt, Phys. Rev. A **31**, 3579 (1985).

[42] R. Anholt, W. Meyerhof, H. Gould, C. Munger, J. Alonso, P. Thieberger, and H. Wegner, Phys. Rev. A **32**, 3302 (1985).

[43] W. E. Meyerhof, Phys. Rev. A **32**, 3291 (1985).

[44] R. Anholt and W. Meyerhof, Phys. Rev. A **33**, 1556 (1986).

[45] R. Anholt, C. Stoller, J. Molitoris, D. Spooner, E. Morenzoni, S. Andriamonje, W. Meyerhof, H. Bowman, J. Xu, Z. Xu, J. Rasmussen, and D. Hoffmann, Phys. Rev. A **33**, 2270 (1986).

[46] R. Anholt, W. E. Meyerhof, X. Xu, H. Gould, B. Feinberg, R. Mcdonald, H. Wegner, and P. Thieberger, Phys. Rev. A **36**, 1586 (1987).

[47] W. E. Meyerhof, R. Anholt, and X. Y. Xu, Phys. Rev. A **35**, 1055 (1987).

[48] R. Anholt, Phys. Rev. A **19**, 1004 (1979).

[49] E. Liatard, J. F. Bruandet, F. Glasser, and T. U. Chan, Z. Phys. D **2**, 223 (1986).

[50] V. Horvat, G. Sampoll, K. Wohrer, M. Chabot, and R. Watson, Phys. Rev. A **46**, 2572 (1992).

[51] Y. Zou, Y. Awaya, C. P. Bhalla, T. Kambara, Y. Kanai, M. Oura, Y. Nakai, K. Ando, A. Hitachi, and S. Kravis, Phys. Rev. A **51**, 3790 (1995).

[52] V. Kravchuk, A. Van Den Berg, F. Fleurot, M. De Huu, H. Lohner, H. Wilschut, M. Polasik, M. Lewandowska-Robak, and K. Slabkowska, Phys. Rev. A **64**, 062710 (2001).

[53] V. Kravchuk, H. Wilschut, A. Van Den Berg, B. Davids, F. Fleurot, M. Hunyadi, M. De Huu, H. Lohner, and A. Van Der Woude, Phys. Rev. A **67**, 052709 (2003).

[54] M. H. Chen, B. Crasemann, and H. Mark, Phys. Rev. A **26**, 1243 (1982).

[55] M. H. Chen, B. Crasemann, and H. Mark, Phys. Rev. A **27**, 2358 (1983).

[56] E. Merzbacher and H. N. Lewis, Handbuch der Physik **34**, 166 (1958).

[57] M. Pauli and D. Trautmann, J. Phys. B **11**, 667 (1978).

[58] J. D. Garcia, R. J. Fortner, and T. M. Kavanagh, Rev. Mod. Phys. **45**, 111 (1973).

[59] J. D. Garcia, Phys. Rev. A **1**, 1402 (1970).

[60] J. D. Garcia, Phys. Rev. A **1**, 280 (1970).

[61] J. D. Garcia, Phys. Rev. A **4**, 955 (1971).

[62] B. Sulik and G. Hock, in *Proceedings of the 2nd Workshop on High-Energy Ion-Atom Collision Processes*, edited by D. B. a. G. Hock. (Akadémiai Kiadó, Budapest, Debrecen, Hungary, 1984), pp. 183.

[63] B. Sulik, G. Hock, and D. Berenyi, J. Phys. B **17**, 3239 (1984).

[64] B. Sulik, I. Kadar, S. Ricz, D. Varga, J. Vegh, G. Hock, and D. Berenyi, Nucl Instrum. Methods Phys. Res B **28**, 509 (1987).

[65] B. Crasemann, *Ionization and Transition Probabilities Volume I* (Academic Press, New York 1975).

[66] E. Merzbacher, in *the International Conference on Inner Shell Ioniaztion Phenomena* (North-Holland, Amsterdam, Atlanta, Georgia, 1972).

[67] B. Choi, E. Merzbacher, and G. Khandelwal, Atomic Data **5**, 291 (1973).

[68] G. Khandelwal, B. Choi, and E. Merzbacher, Atomic Data **1**, 103 (1969).

[69] M. E. Rudd, Y. K. Kim, D. H. Madison, and J. W. Gallagher, Phys. Rev. A **57**, 965 (1985).

[70] D. Trautmann, G. Baur, and F. Rosel, J. Phys. B **16**, 3005 (1983).

[71] D. Trautmann and F. Rosel, Nucl. Instrum. Methods **169**, 259 (1980).

[72] W. Brandt, R. Laubert, and I. Sellin, Phys. Rev. **151**, 56 (1966).

[73] A. Amundsen, J. Phys. B **10**, 2177 (1977).

[74] A. Amundsen, J. Phys. B **10**, 2177 (1977).

[75] P. A. Amundsen and L. Kocbach, J. Phys. B, L122 (1975).

[76] M. Pauli, F. Rosel, and D. Trautmann, Journal of Physics B: Atomic and Molecular Physics, 2511 (1978).

[77] B. Choi, Phys. Rev. A **4**, 1002 (1971).

[78] H. S. Brandi and B. Koiller, Phys. Rev. A **19**, 1058 (1979).

[79] H. S. Brandi and B. Koiller, Phys. Rev. A **23**, 975 (1981).

[80] G. Lapicki, Phys. Rev. A **23**, 975 (1981).

[81] G. Lapicki and F. D. Mcdaniel, Phys. Rev. A **22**, 1896 (1980).

[82] Z. Liu and S. J. Cipolla, Comp. Phys. Comm. **97**, 315 (1996).

[83] G. Lapicki, J. Phys. Chem. Ref. Data **18**, 111 (1989).

[84] Gryzinsk.M, Phys. Rev. **138**, A305 (1965).

[85] Gryzinsk.M, Phys. Rev. **138**, A322 (1965).

[86] Gryzinsk.M, Phys. Rev. **138**, A336 (1965).

[87] M. E. Rudd, D. Gregoire, and J. B. Crooks, Phys. Rev. A **3**, 1635 (1971).

[88] J. H. Mcguire and P. Richard, Phys. Rev. A **8**, 1374 (1973).

[89] J. M. Hansteen, Nucl. Instrum. Methods Phys. Res. B **42**, 426 (1989).

[90] A. Amundsen, J. Phys. B **9**, 971 (1976).

[91] K. Taulbjerg, J. Phys. B **10**, L341 (1977).

[92] D. Trautmann, F. Rosel, and G. Baur, Nucl. Instrum. Methods **214**, 21 (1983).

[93] G. Baur, M. Pauli, and D. Trautmann, J. Phys. G **2**, 171 (1976).

[94] R. L. Becker, A. L. Ford, and J. F. Reading, Nucl. Instrum. Methods **214**, 49 (1983).

[95] D. Banas, M. Pajek, J. Semaniak, J. Braziewicz, A. Kubala-Kukus, U. Majewska, T. Czyzewski, M. Jaskola, W. Kretschmer, T. Mukoyama, and D. Trautmann, Nucl. Instrum. Methods Phys. Res. B **195**, 233 (2002).

[96] V. Horvat, R. L. Watson, and Y. Peng, Phys. Rev. A **74**, 022718 (2006).

[97] D. H. Madison and E. Merzbacher, in *Atomic Inner-Shell Processes*, edited by B. Crasemann, (Academic Press, New York 1975), p 1.

[98] F. Hund, Z. Phys. **40**, 742 (1927).

[99] R. S. Mulliken, Phys. Rev. **32**, 186 (1928).

[100] U. Fano and W. Lichten, Phys. Rev. Lett. **14**, 627 (1965).

[101] M. Barat and W. Lichten, Phys. Rev. A **6**, 211 (1972).

[102] J. Eichler, U. Wille, B. Fastrup, and K. Taulbjerg, Phys. Rev. A **14**, 707 (1976).

[103] W. E. Meyerhof and K. Taulbjerg, Annual Review of Nuclear and Particle Science **27**, 279 (1977).

[104] F. W. Saris, W. F. V. D. Weg, H. Tawara, and R. Laubert, Phys. Rev. Lett. **28**, 717 (1972).

[105] W. Lichten, Phys. Rev. **164**, 131 (1967).

[106] J. S. Briggs, Rep. Prog. Phys. **39**, 217 (1976).

[107] G. Lapicki and W. Lichten, Phys. Rev. A **31**, 1354 (1985).

[108] W. E. Meyerhof, R. Anholt, T. Saylor, and P. Bond, Phys. Rev. A **11**, 1083 (1975).

[109] R. Anholt, Rev. Mod. Phys. **57**, 995 (1985).

[110] W. E. Meyerhof, R. Anholt, and W. Wolfli, Phys. Lett. B **84**, 59 (1979).

[111] B. M. Tissue, website: *Photomultiplier Tube (PMT)*, accessed on 09-30, 2006, http://www.chem.vt.edu/chem-ed/optics/detector/pmt.html

[112] J. L. Campbell and P. L. Mcghee, Nucl Instrum. Methods Phys. Res A **248**, 393 (1986).

[113] J. S. Hansen, J. C. Mcgeorge, D. Nix, W. D. Schmidt-Ott, I. Unus, and R. W. Fink, Nucl. Instrum. Methods **106**, 365 (1973).

[114] M. Krumrey and E. Tegeler, Review of Scientific Instruments **63**, 797 (1992).

[115] F. Scholze and G. Ulm, Nucl Instrum. Methods Phys. Res A **339**, 49 (1994).

[116] P. Muller, F. Riehle, E. Tegeler, and B. Wende, Nucl Instrum. Methods Phys. Res A **246**, 569 (1986).

[117] F. Scholze and M. Procop, X-Ray Spectrometry **30**, 69 (2001).

[118] W. N. Lennard and D. Phillips, Nucl. Instrum. Methods **166**, 521 (1979).

[119] M. Pajek, D. Banas, J. Semaniak, J. Braziewicz, U. Majewska, S. Chojnacki, T. Czyzewski, I. Fijal, M. Jaskola, A. Glombik, W. Kretschmer, D. Trautmann, G. Lapicki, and T. Mukoyama, Phys. Rev. A **68**, 022705 (2003).

[120] J. Palinkas and B. Schlenk, Nucl. Instrum. Methods **169**, 493 (1980).

[121] U. Wolters, D. Meyer, and K. Wiesemann, J. Phys. D **31**, 2112 (1998).

[122] J. Tschischgale, D. Kuchler, U. Lehnert, and G. Zschornack, Nucl Instrum. Methods Phys. Res A **400**, 387 (1997).

[123] D. L. Weathers, J. L. Duggan, M. R. Mcneir, Y. C. Yu, F. D. Mcdaniel, C. A. Quarles, H. Lehtihet, and D. Kahler, Nucl Instrum. Methods Phys. Res B **56-57**, 964 (1991).

[124] W. Maenhaut and H. Raemdonck, Nucl Instrum. Methods Phys. Res B **1**, 123 (1984).

[125] D. D. Cohen, Nucl. Instrum. Methods. **193**, 15 (1982).

[126] S. J. Cipolla and S. M. Watson, Nucl Instrum. Methods Phys. Res B **10-11**, 946 (1985).

[127] N. V. De Castro Faria, F. L. Freire, A. G. De Pinho, and E. F. Da Silveira, Phys. Rev. A **28**, 2770 (1983).

[128] W. J. Gallagher and S. J. Cipolla, Nucl. Instrum. Methods **122**, 405 (1974).

[129] E. Karttunen, H. U. Freund, and R. W. Fink, Phys. Rev. A **4**, 1695 (1971).

[130] Private communication, IAEA evaluation, A. Nichols to J. C. Hardy

[131] B. B. Bandong, Ph.D dissertation, Texas A&M University, College Station (May, 1988)

[132] L. S. Birks, in *X-ray Spectrometry*, edited by H. K. Herglotz, and L. S. Birks, (Marcel Dekker, INC., New York and Basel, 1978), p 10.

[133] J. Goldstein, D. E. Newbury, D. C. Joy, C. E. Lyman, P. Echlin, E. Lifshin, L. C. Sawyer, and J. R. Michael, *Scanning Electron Microscopy and X-ray Microanalysis* (Springer, New York, 2003).

[134] J. Blackdale, Ph.D. dissertation, Texas A&M University, College Station (August, 1999)

[135] J. A. Bearden, Rev. Mod. Phys. **39**, 78 (1967).

[136] J. A. Bearden and A. F. Burr, Rev. Mod. Phys. **39**, 125 (1967).

[137] F. T. Porter and M. S. Freedman, J. Phys. Chem. Ref. Data **7**, 1267 (1978).

[138] K. D. Sevier, At. Data Nucl. Data Tables **24**, 323 (1979).

[139] R. D. Deslattes, E. G. Kessler, P. Indelicato, L. De Billy, E. Lindroth, and J. Anton, Rev. Mod. Phys. **75**, 35 (2003).

[140] D. Coster, L. Kronig, and R. De, Physica **2**, 13 (1935).

[141] M. H. Chen and B. Crasemann, Phys. Rev. A **16**, 1495 (1977).

[142] R. L. Watson, F. E. Jenson, and T. Chiao, Phys. Rev. A **10**, 1230 (1974).

[143] R. L. Watson, T. Chiao, and F. E. Jensen, Bull. Amer. Phys. Soc. **19**, 591 (1974).

[144] P. Rymuza, Z. Sujkowski, M. Carlen, J. C. Dousse, M. Gasser, J. Kern, B. Perny, and C. Rheme, Z. Phys. D **14**, 37 (1989).

[145] C. Schmiedekamp, Doyle, B. L., Gray, T. J., Gardner, R. K., Jamison, K. A., Richard, P., Phys. Rev. A **18**, 1892 (1978).

[146] T. Ludziejewski, P. Rymuza, Z. Sujkowski, G. Borchert, J. C. Dousse, C. Rheme, and M. Polasik, Phys. Rev. A **54**, 232 (1996).

[147] M. Polasik, Phys. Rev. A **41**, 3689 (1990).

[148] M. Polasik, Phys. Rev. A **39**, 616 (1989).

[149] M. Polasik, Phys. Rev. A **40**, 4361 (1989).

[150] E. Schonfeld and G. Rodloff, PTB-6.11-1999-1 Physikalisch-Technische Bundesanstalt Braunschweig, Februar (1999)

[151] M. O. Krause, J. Phys. Chem. Ref. Data **8**, 307 (1979).

[152] E. J. Mcguire, Phys. Rev. **185**, 1 (1969).

[153] E. J. Mcguire, Phys. Rev. A **2**, 273 (1970).

[154] D. L. Walters and C. P. Bhalla, Phys. Rev. A **4**, 2164 (1971).

[155] D. L. Walters and C. P. Bhalla, Phys. Rev. A **3**, 1919 (1971).

[156] D. L. Walters and C. P. Bhalla, Phys. Rev. A **3**, 519 (1971).

[157] M. H. Chen, B. Crasemann, and H. Mark, Phys. Rev. A **21**, 436 (1980).

[158] V. O. Kostroun, M. H. Chen, and B. Craseman, Phys. Rev. A **3**, 533 (1971).

[159] B. Crasemann, M. H. Chen, and V. O. Kostroun, Phys. Rev. A **4**, 2161 (1971).

[160] J. H. Scofield, Phys. Rev. A **179**, 9 (1969).

[161] W. Bambynek, C. D. Swift, B. Craseman, H. U. Frend, P. V. Rao, R. E. Price, H. Mark, and R. W. Fink, Rev. Mod. Phys. **44**, 716 (1972).

[162] N. Nica, J. C. Hardy, V. E. Iacob, J. R. Montague, and M. B. Trzhaskovskaya, Phys. Rev. C **71** (2005).

[163] A. Kucukonder, J. Quant. Spectr. Rad. Tran. **90**, 125 (2005).

[164] S. B. Gudennavar, N. M. Badiger, S. R. Thontadarya, and B. Hanumaiah, Rad. Phys. Chem. **68**, 721 (2003).

[165] T. Yashoda, S. Krishnaveni, S. Gowda, T. K. Umesh, and R. Gowda, Pramana-Journal of Physics **58**, 31 (2002).

[166] O. Simsek, S. Yilmaz, D. Karagoz, and M. Ertugrul, J. Radio. Nucl. Chem. **253**, 143 (2002).

[167] O. Simsek, M. Ertugrul, D. Karagoz, G. Budak, A. Karabulut, S. Yilmaz, O. Dogan, U. Turgut, O. Sogut, R. Polat, and A. Gurol, Rad. Phys. Chem. **65**, 27 (2002).

[168] J. K. Pious, K. M. Balakrishna, N. Lingappa, and K. Siddappa, J. Phys. B **25**, 1155 (1992).

[169] M. Takiue and H. Ishikawa, Nucl. Instrum. Methods **173**, 391 (1980).

[170] A. Langenberg, Ph.D. dissertation, University of Utrecht, Utrecht, Netherlands (March, 1978)

[171] E. H. S. Burhop, *The Auger Effect and Other Radiationless Transitions* (Cambridge University Press, New York, 1952).

[172] W. Hankel and Wapstra, *X-ray Spectrum* (Marcel Dekker, INC., New York, Basel, 1985), Vol. 2, p. 43.

[173] D. F. Anagnostopoulos, G. Borchert, D. Gotta, K. Rashid, D. H. Jakubassa-Amundsen, and P. A. Amundsen, Phys. Rev. A **58**, 2797 (1998).

[174] D. F. Anagnostopoulos, J. Phys. B **28**, 47 (1995).

[175] M. Polasik, S. Raj, B. B. Dhal, H. C. Padhi, A. K. Saha, M. B. Kurup, K. G. Prasad, and P. N. Tandon, J. Phys. B **32**, 3711 (1999).

[176] V. Horvat, R. Watson, and J. Blackadar, Nucl. Instrum. Methods Phys. Res. B **170**, 336 (2000).

[177] M. Kobal, Nucl Instrum. Methods Phys. Res B **229**, 165 (2005).

[178] U. Kadhane, C. C. Montanari, and C. T. Lokesh, Phys. Rev. A **67**, 032703 (2003).

[179] F. P. Larkins, J. Phys. B, L29 (1971).

[180] J. H. Hubbell and S. M. Seltzer, website: *X ray mass attenuation coefficients*, accessed on 7-27, 2006, http://physics.nist.gov/PhysRefData/XrayMassCoef/chap2.html

[181] J. F. Ziegler, PC program *SRIM*, Ver. 2003, PC,

[182] G. Friedlander, J. W. Kennedy, E. S. Macias, and J. M. Miller, *Nuclear and Radiochemistry* (John Willey & Sons, Inc., New York, 1981).

[183] Xcom, website: *XCOM*, accessed on 10-4, 2006, http://physics.nist.gov/cgi-bin/Xcom/xcom2

[184] IBM-PC program *Peakfit*, Ver. 4.12, IBM-PC,

[185] J. H. Mcguire and L. Weaver, Phys. Rev. A **16**, 41 (1977).

[186] B. Sulik, I. Kadar, S. Ricz, D. Varga, J. Vegh, G. Hock, and D. Berenyi, Nucl. Instrum. Methods Phys. Res. B **28**, 509 (1987).

[187] J. H. Scofield, Phys. Rev. A **9**, 1041 (1974).

[188] G. J. Balster, W. V. Huffelen, and H. W. Wilschut, Z. Phys. D **2**, 6 (1986).

[189] R. L. Watson, V. Horvat, and K. E. Zaharakis, in *Proceedings of the 16th International Conference on the Application of Accelerators in Research and Industry* (American Institute of Physics CP576, Denton, Texas, 2001), p. 93.

[190] V. Horvat, Ž. Šmit, R. L. Watson, A. N. Perumal, and Y. Peng, in *Proceedings of the 17th International Conference on the Application of Accelerators in Research and Industry* (American Institute of Physics CP576, Denton, Texas, 2002), p. 7.

VITA

Yong Peng was born in 1970 in Hanyuan, Sichuan, China. He received his B.S. diploma in chemistry from Sichuan University in 1994. Then he worked in CAEP, China. In 1997, he started his M.S. study at the University of Science and Technology of China. Supported by the Welch Foundation, he began his current program in Texas A&M University in 1999. He received his Ph.D. degree in December 2006. His permanent mailing address is Matuo Dapu, Hanyuan County, Sichuan Province, China, 625304.